A Numerical Study of the Cosmic Microwave Background

AST5220 - Cosmology II

Candidate 15011

Institute of Theoretical Astrophysics (ITA), University of Oslo

May 8, 2025

ABSTRACT

Context. CONTEXT
Aims. AIMS
Methods. METHODS
Results. RESULTS
Conclusions. CONCLUSIONS

Key words. cosmic background radiation - large-scale structure of Universe

1. Introduction

TODO: proper intro when finished

In this work, I extensively reference the 2018 Planck results (see Planck Collaboration et al. 2020), which serve as the fiducial cosmology. The theoretical framework for this study, including derivations and discussions, is based on material from the AST5220 - Cosmology II course taught by Hans A. Winther at the University of Oslo (see Winther et al. Accessed: June 2025). All computational codes used in this work are available on my GitHub repository, with major components based on templates developed by Winther.

2. Milestone I: Background Cosmology

The evolution of the universe is governed by the interplay between different energy components, including radiation, matter, and dark energy. Understanding how these components influence the expansion history is essential for predicting the large-scale structure of the Universe and the Cosmic Microwave Background (CMB) fluctuations. This milestone focuses on modeling the background evolution of the Universe using the Friedmann equations, which describe how the Hubble parameter H, and thus time and distance measures, evolve with redshift.

I implement a numerical framework that takes in cosmological parameters and computes such key background quantities, and use this to fit to measurements of supernova luminosity distances. By completing this milestone, I aim to establish a robust computational framework that serves as a foundation for later stages of the project, where I analyze perturbations and extract information about CMB anisotropies to obtain constraints on cosmological parameters. TODO: maybe change

2.1. Theoretical framework

2.1.1. Evolution of the Universe and the Hubble parameter

The expansion of the Universe is governed by General Relativity, with the large-scale dynamics described by the Friedmann-Lemaître-Robertson-Walker (FLRW) metric. Assuming a homogeneous and isotropic universe, the metric is given by

$$ds^2 = -c^2dt^2 + a^2(t)\left[\frac{dr^2}{1 - kr^2} + r^2d\theta^2 + r^2\sin^2\theta d\phi^2\right], \quad (2.1)$$

where $a(t) = 1/(1 + z)$ is the dimensionless scale factor, with z being the cosmological redshift. The constant k determines the curvature of the Universe ($k = 0$ for a flat universe, $k > 0$ for a closed universe, and $k < 0$ for an open universe).

The evolution of $a(t)$ is governed by the Friedmann equation, which is derived from Einstein's field equations:

$$H^2 = \frac{8\pi G}{3}\sum_i \rho_i - \frac{kc^2}{a^2} \simeq \frac{8\pi G}{3}\sum_i \rho_i, \quad (2.2)$$

Here, $H = \dot{a}/a$ is the Hubble parameter, and ρ_i denotes the total energy density of some component (photons, baryons, etc.). In the second equality I have used that we can treat the curvature as its own component that is included in the sum, with energy density

$$\rho_k = -\frac{3}{8\pi G}\frac{kc^2}{a^2}. \quad (2.3)$$

It is essential to know not only how the curvature "energy density" scales with a, but the other components as well. To understand this, we start with the continuity equation for a perfect fluid, which is a very accurate description of the energy density components in the Universe on the largest scales, applied to a homogeneous and isotropic universe:

$$\frac{d\rho_i}{dt} + 3H(\rho_i + p_i) = \frac{d\rho_i}{dt} + \frac{3}{a}\frac{da}{dt}\rho_i(1 + w_i) = 0. \quad (2.4)$$

Here, p_i is the pressure of the fluid, and $w_i = p_i/\rho_i$ is the equation of state parameter, which is constant for the fluids considered in conventional cosmology. This differential equation is easily solved by separating variables and integrating, which gives us:

$$\rho_i(a) = \rho_{i0}a^{-3(1+w_i)}, \quad (2.5)$$

where ρ_{i0} is the present-day density.

On large scales, non-relativistic matter can essentially be treated as pressureless, hence $w_m = w_b = w_{CDM} = 0$ and thus

$\rho_m \propto a^{-3}$. This corresponds to the dilution of a density field in an expanding volume. Furthermore, neutrinos are so light that they can still be treated as relativistic (radiation), and we therefore have $w_r = w_\gamma = w_\nu = 1/3$, which implies $\rho_r \propto a^{-4}$. Radiation is also diluted as the Universe expands, and the extra factor of a^{-1} comes from redshifting of relativistic particles in an expanding universe. From eq. (2.3) we indeed see that we can treat curvature as a perfect fluid with equation of state $w_k = -1/3$, while dark energy, represented by the cosmological constant Λ, remains constant in time, hence $w_\Lambda = -1$.

A much more convenient way of writing the Friedmann equation can be derived by defining the critical density, which is the density required for a flat universe ($k = 0$):

$$\rho_c = \frac{3H^2}{8\pi G}. \tag{2.6}$$

We may then define the dimensionless density parameters, which describe how much of the total energy density each component i contributes:

$$\Omega_i = \frac{\rho_i}{\rho_c}. \tag{2.7}$$

Substituting this into the Friedmann equation gives us then

$$H^2 = \frac{8\pi G}{3} \sum_i \Omega_i \rho_c = H^2 \sum_i \Omega_i, \tag{2.8}$$

which shows us explicitly that the density parameters always must sum up to unity. We would like to rewrite this in terms of quantities that we can actually measure today, such as the present day density parameters Ω_{i0}. In that case, H^2 becomes H_0^2 on the right-hand side of eq. (2.8). Furthermore, since we know how the density components scale with a, we may write

$$H^2 = H_0^2 \sum_i \Omega_{i0} a^{-3(1+w_i)}. \tag{2.9}$$

The equivalency of this expression with eq. (2.8) tells us that

$$\Omega_i(a) = \frac{\Omega_{i0} a^{-3(1+w_i)}}{H^2(a)/H_0^2}, \tag{2.10}$$

Additionally, taking the square root on both sides of eq. (2.9) and writing out the terms explicitly, we have

$$H = H_0 \sqrt{(\Omega_{b0} + \Omega_{\text{CDM0}})a^{-3} + (\Omega_{\gamma0} + \Omega_{\nu0})a^{-4} + \Omega_{k0}a^{-2} + \Omega_{\Lambda0}}. \tag{2.11}$$

When fitting to measurements of supernova luminosity distances, I attempt to constrain all but the photon and neutrino density parameters. This is because we know these are given by

$$\Omega_{\gamma0} = g \frac{\pi^2}{30} \frac{(k_B T_{\text{CMB0}})^4}{\hbar^3 c^5} \frac{8\pi G}{3H_0^2}, \tag{2.12}$$

$$\Omega_{\nu0} = \frac{7}{8} N_{\text{eff}} \left(\frac{4}{11}\right)^{1/3} \Omega_{\gamma0}. \tag{2.13}$$

where $g = g_\gamma = g_\nu = 2$, since photons and neutrinos both have 2 internal polarization states. We see that the only free parameters that appear in these expressions are T_{CMB0}, the present day value of the CMB temperature, and N_{eff}, the effective number of relativistic degrees of freedom, both of which are determined to high precision already.

When integrating from the very early universe, using the scale factor a as the time parameter becomes numerically challenging, as it rapidly decreases to vanishingly small values. To address this, I therefore adopt the logarithmic time coordinate

$$x = \log(a), \tag{2.14}$$

instead, which implies that $x = 0$ today and $x = -\infty$ at the Big Bang. Expressed in terms of $\Omega_{m0} = \Omega_{b0} + \Omega_{\text{CDM0}}$ and $\Omega_{r0} = \Omega_{\gamma0} + \Omega_{\nu0}$, we can equivalently write the Hubble parameter as

$$H = H_0 \sqrt{\Omega_{m0}e^{-3x} + \Omega_{r0}e^{-4x} + \Omega_{k0}e^{-2x} + \Omega_{\Lambda0}}. \tag{2.15}$$

A commonly used rescaled version of the Hubble parameter is the conformal Hubble parameter:

$$\mathcal{H} = aH = H_0 \sqrt{\Omega_{m0}e^{-x} + \Omega_{r0}e^{-2x} + \Omega_{k0} + \Omega_{\Lambda0}e^{2x}}. \tag{2.16}$$

This naturally appears when rewriting cosmological equations in terms of the conformal time η, which I present below. I focus more on this version of the Hubble parameter, partly because its first and second derivatives with respect to x prove themselves useful verifing the validity of approximations I make later on. After some tedious calculation, we find that these are

$$\frac{d\mathcal{H}}{dx} = \frac{H_0}{2} \frac{-\Omega_{m0}e^{-x} - 2\Omega_{r0}e^{-2x} + 2\Omega_{\Lambda0}e^{2x}}{\sqrt{\Omega_{m0}e^{-x} + \Omega_{r0}e^{-2x} + \Omega_{k0} + \Omega_{\Lambda0}e^{2x}}},$$
$$= -\frac{H_0^2}{2\mathcal{H}} \left(\Omega_{m0}e^{-x} + 2\Omega_{r0}e^{-2x} - 2\Omega_{\Lambda0}e^{2x}\right), \tag{2.17}$$

$$\frac{d^2\mathcal{H}}{dx^2} = \frac{H_0}{2} \left(\frac{\Omega_{m0}e^{-x} + 4\Omega_{r0}e^{-2x} + 4\Omega_{\Lambda0}e^{2x}}{\sqrt{\Omega_{m0}e^{-x} + \Omega_{r0}e^{-2x} + \Omega_{k0} + \Omega_{\Lambda0}e^{2x}}} \right.$$
$$\left. - \frac{1}{2} \frac{\left(\Omega_{m0}e^{-x} + 2\Omega_{r0}e^{-2x} - 2\Omega_{\Lambda0}e^{2x}\right)^2}{(\Omega_{m0}e^{-x} + \Omega_{r0}e^{-2x} + \Omega_{k0} + \Omega_{\Lambda0}e^{2x})^{3/2}} \right),$$
$$= \frac{H_0^2}{\mathcal{H}} \left[\frac{1}{2}\Omega_{m0}e^{-x} + 2\Omega_{r0}e^{-2x} + 2\Omega_{\Lambda0}e^{2x} - \frac{1}{H_0^2}\left(\frac{d\mathcal{H}}{dx}\right)^2 \right]. \tag{2.18}$$

maybe move to appendix

2.1.2. Conformal time and distance measures

The cosmic time t is related to our time variable x through

$$\frac{dt}{dx} = \frac{dt}{da}\frac{da}{dx} = \frac{a}{\dot{a}} = \frac{1}{H}, \tag{2.19}$$

hence, to compute the cosmic time t given our time coordinate x, we simply integrate this to get

$$t(x) = \int_{-\infty}^{x} \frac{dx'}{H(x')}. \tag{2.20}$$

Evaluating this at $x = 0$ (today), we obtain the age of the Universe.

While it is interesting to solve our system of equations for t, it is more useful to introduce the conformal time η. This is defined as

$$d\eta = \frac{cdt}{a} \quad \Leftrightarrow \quad \frac{d\eta}{dx} = \frac{c}{\mathcal{H}}, \tag{2.21}$$

and thus has units of length. The equation on the right can easily be numerically integrated to obtain $\eta(x)$, which describes how far

light has traveled since the Big Bang. It is therefore also called the particle horizon, and is a crucial concept in cosmology, as it determines the causal structure of the Universe.

A closely related quantity is the so-called comoving distance a photon has travelled since emission, defined as

$$\chi = \eta_0 - \eta, \tag{2.22}$$

where η_0 is the conformal time today. This is fundamental in defining distance measures in cosmology. We know that photons travel along null geodesics $ds^2 = 0$, and from the conformal time and the FLRW line element we see that this implies that the coordinate distance r satisfies

$$c\,dt = \frac{a\,dr}{\sqrt{1 - kr^2}}, \tag{2.23}$$

for a radially traveling photon ($d\theta = d\phi = 0$). Changing the time coordinate to conformal time, we rewrite this as

$$d\eta = \frac{dr}{\sqrt{1 - kr^2}}, \tag{2.24}$$

and integrating from emission at time η to today, we get precisely the comoving distance:

$$\int_{\eta}^{\eta_0} d\eta' \equiv \chi = \int_0^r \frac{dr'}{\sqrt{1 - kr'^2}}. \tag{2.25}$$

Solving this integral for different values of the curvature constant k, we obtain

$$r = \chi \begin{cases} \dfrac{\sin\left(\sqrt{|\Omega_{k0}|}H_0\chi/c\right)}{\left(\sqrt{|\Omega_{k0}|}H_0\chi/c\right)}, & \Omega_{k0} < 0 \quad \text{(Closed)}, \\[2ex] 1, & \Omega_{k0} = 0 \quad \text{(Flat)}, \\[2ex] \dfrac{\sinh\left(\sqrt{|\Omega_{k0}|}H_0\chi/c\right)}{\left(\sqrt{|\Omega_{k0}|}H_0\chi/c\right)}, & \Omega_{k0} > 0 \quad \text{(Open)}. \end{cases} \tag{2.26}$$

This defines the proper radial coordinate r, which is used in all cosmological distance measures.

The angular diameter distance relates an object's physical extent D to its observed angular extent θ on the sky:

$$d_A = \frac{D}{\theta}. \tag{2.27}$$

From the metric, we see that the transverse separation of a source at r subtending an angle $d\theta$ is

$$dD = ar\,d\theta, \tag{2.28}$$

hence the angular diameter distance:

$$d_A = ar, \tag{2.29}$$

which simplifies to:

$$d_A = a\chi, \tag{2.30}$$

for a flat universe.

Even more relevant for this milestone is the luminosity distance, which is dependent on the measured brightness of standard candles like Type Ia supernovae. We know that the flux F from a source with luminosity L follows an inverse-square law:

$$F = \frac{L}{4\pi d_L^2}. \tag{2.31}$$

In an expanding universe, photons are redshifted and their arrival rate is also affected, leading to the relation:

$$d_L = d_A(1 + z)^2 = \frac{d_A}{a^2}. \tag{2.32}$$

This quantity is crucial in observational cosmology as it accounts for both the geometric distance and the redshifted energy of photons. It is therefore fundamental for interpreting supernovae observations and measuring cosmic expansion.

2.1.3. Key cosmological epochs

Though it also has been verified by numerous observations, based on the expression for the Hubble parameter it is not hard to see that the Universe must have gone through phases where its energy budget was (or will be) dominated by radiation, matter and dark energy, separately, in that order. This implies that there must have been a point in time where the Universe was equal amounts of radiation and matter (matter and dark energy), if we neglect the curvature and dark energy (radiation). At radiation-matter equality (rm) we have

$$\Omega_{r,rm} = \Omega_{m,rm} \quad \Leftrightarrow \quad \Omega_{r0}e^{-4x_{rm}} = \Omega_{m0}e^{-3x_{rm}}, \tag{2.33}$$

and thus

$$x_{rm} = \log\left(\frac{\Omega_{r0}}{\Omega_{m0}}\right). \tag{2.34}$$

Using that $x = \log(a)$ and $z = 1/a - 1$ this gives us an expression for the redshift at rm:

$$z_{rm} = \frac{\Omega_{m0}}{\Omega_{r0}} - 1. \tag{2.35}$$

Similarly, at matter-dark energy equality ($m\Lambda$) we have

$$\Omega_{m0}e^{-3x_{m\Lambda}} = \Omega_{\Lambda 0} \quad \Leftrightarrow \quad x_{m\Lambda} = \frac{1}{3}\log\left(\frac{\Omega_{m0}}{\Omega_{\Lambda 0}}\right), \tag{2.36}$$

and thus

$$z_{m\Lambda} = \left(\frac{\Omega_{\Lambda 0}}{\Omega_{m0}}\right)^{1/3} - 1. \tag{2.37}$$

To ensure that the numerical results presented in this work agree with analytical expectations, it is beneficial to have approximate expressions for the cosmic and conformal times in the different regimes. For a universe dominated by a single component with equation of state w_i the cosmic time t is given by

$$t = \int_0^t dt' = \int_{-\infty}^x \frac{dx'}{H_0\sqrt{\Omega_{i0}e^{-3(1+w_i)x'}}}. \tag{2.38}$$

When the Universe transitions between an era where its energy density is dominated by some component ρ_j to some other component ρ_i, we may neglect all other components and compute an approximate expression for the cosmic time as function of x by writing

$$t_i(x) \approx t_{j,i} + \int_{x_{j,i}}^x \frac{dx'}{H_0\sqrt{\Omega_{i0}e^{-3(1+w_i)x'}}}, \tag{2.39}$$

where $x_{j,i}$ and $t_{j,i}$ correspond to their values when $\rho_j = \rho_i$. For radiation we simply have $x_{j,i} = -\infty$ and thus $t_{j,i} = 0$, since the very early Universe was filled with relativistic particles, hence

$$t_r(x) = \int_{-\infty}^x \frac{dx'}{H_0\sqrt{\Omega_{r0}e^{-4x'}}} = \frac{1}{2H_0\sqrt{\Omega_{r0}e^{-4x}}}. \tag{2.40}$$

We see that radiation-matter equality occurs at

$$t_{rm} = t_r(x_{rm}) = \frac{\Omega_{r0}^{3/2}}{2H_0 \Omega_{m0}^2}, \tag{2.41}$$

and for matter it then follows

$$
\begin{aligned}
t_m(x) &\approx t_{rm} + \int_{x_{rm}}^{x} \frac{dx'}{H_0 \sqrt{\Omega_{m0}e^{-3x'}}}, \\
&= \frac{\Omega_{r0}^{3/2}}{2H_0\Omega_{m0}^2} + \frac{2}{3H_0}\left[\frac{1}{\sqrt{\Omega_{m0}e^{-3x}}} - \frac{\Omega_{r0}^{3/2}}{H_0\Omega_{m0}^2}\right], \\
&= \frac{1}{3H_0}\left[\frac{2}{\sqrt{\Omega_{m0}e^{-3x}}} - \frac{\Omega_{r0}^{3/2}}{2\Omega_{m0}^2}\right],
\end{aligned} \tag{2.42}
$$

with matter-dark energy equality occuring at

$$t_{m\Lambda} = \frac{1}{3H_0}\left[\frac{2}{\sqrt{\Omega_{\Lambda 0}}} - \frac{\Omega_{r0}^{3/2}}{2\Omega_{m0}^2}\right]. \tag{2.43}$$

Lastly, for dark energy we have

$$
\begin{aligned}
t_\Lambda(x) &\approx t_{m\Lambda} + \int_{x_{m\Lambda}}^{x} \frac{dx'}{H_0 \sqrt{\Omega_{\Lambda 0}}}, \\
&= \frac{1}{3H_0}\left[\frac{2}{\sqrt{\Omega_{\Lambda 0}}} - \frac{\Omega_{r0}^{3/2}}{2\Omega_{m0}^2}\right] + \frac{1}{H_0 \sqrt{\Omega_{\Lambda 0}}}\left[x - \frac{1}{3}\log\left(\frac{\Omega_{m0}}{\Omega_{\Lambda 0}}\right)\right], \\
&= \frac{1}{H_0 \sqrt{\Omega_{\Lambda 0}}}\left[x + \frac{2}{3} - \frac{1}{3}\log\left(\frac{\Omega_{m0}}{\Omega_{\Lambda 0}}\right) - \frac{\sqrt{\Omega_{\Lambda 0}}\Omega_{r0}^{3/2}}{6\Omega_{m0}^2}\right].
\end{aligned} \tag{2.44}
$$

From these derived expressions, it is obvious that $a \propto t^{1/2}$ in the radiation dominated era, $a \propto t^{2/3}$ in the matter era and $a \propto e^{H_0 \sqrt{\Omega_{\Lambda 0}}t}$ in the dark energy era, which is the expected result.

Following an analogous approach for the conformal time, it is straight-forward to show that since

$$\eta_i(x) \approx \eta_{j,i} + \int_{x_{j,i}}^{x} \frac{c\,dx'}{H_0 \sqrt{\Omega_{i0}e^{-(1+3w_i)x'}}}, \tag{2.45}$$

we have the following approximate expressions:

$$\eta_r(x) = \frac{c}{H_0 \sqrt{\Omega_{r0}e^{-2x}}}, \tag{2.46}$$

$$\eta_m(x) = \frac{c}{H_0}\left[\frac{2}{\sqrt{\Omega_{m0}e^{-x}}} - \frac{\sqrt{\Omega_{r0}}}{\Omega_{m0}}\right], \tag{2.47}$$

$$\eta_\Lambda(x) = -\frac{c}{H_0}\left[\frac{1}{\sqrt{\Omega_{\Lambda 0}e^{2x}}} + \frac{\sqrt{\Omega_{r0}}}{\Omega_{m0}} - \frac{3}{\Omega_{m0}^{1/3}\Omega_{\Lambda 0}^{1/6}}\right], \tag{2.48}$$

with the conformal equality times:

$$\eta_{rm} = \frac{c}{H_0}\frac{\sqrt{\Omega_{r0}}}{\Omega_{m0}}, \tag{2.49}$$

$$\eta_{m\Lambda} = \frac{c}{H_0}\left[\frac{2}{\Omega_{m0}^{1/3}\Omega_{\Lambda 0}^{1/6}} - \frac{\sqrt{\Omega_{r0}}}{\Omega_{m0}}\right]. \tag{2.50}$$

To be able to actually test the validity of the approximations made above, it is essential to use them to compute the expected values of some scaled expressions, as this makes it easier to see the relative errors. Obviously, in an era dominated by component i we have

$$\mathcal{H}_i \approx H_0 \sqrt{\Omega_{i0}e^{-(1+3w_i)}}, \tag{2.51}$$

and in the radiation dominated era we thus have

$$\left(\frac{d\mathcal{H}}{dx}\right)_r = -H_0 \sqrt{\Omega_{r0}}e^{-x} = -\mathcal{H}_r \quad \Leftrightarrow \quad \left(\frac{1}{\mathcal{H}}\frac{d\mathcal{H}}{dx}\right)_r = -1, \tag{2.52}$$

$$\left(\frac{d^2\mathcal{H}}{dx^2}\right)_r = H_0 \sqrt{\Omega_{r0}}e^{-x} = \mathcal{H}_r \quad \Leftrightarrow \quad \left(\frac{1}{\mathcal{H}}\frac{d^2\mathcal{H}}{dx^2}\right)_r = 1. \tag{2.53}$$

Similarly, we have

$$\left(\frac{d\mathcal{H}}{dx}\right)_m = -\frac{\mathcal{H}_m}{2} \quad \Leftrightarrow \quad \left(\frac{1}{\mathcal{H}}\frac{d\mathcal{H}}{dx}\right)_m = -\frac{1}{2}, \tag{2.54}$$

$$\left(\frac{d^2\mathcal{H}}{dx^2}\right)_m = \frac{\mathcal{H}_m}{4} \quad \Leftrightarrow \quad \left(\frac{1}{\mathcal{H}}\frac{d^2\mathcal{H}}{dx^2}\right)_m = \frac{1}{4}. \tag{2.55}$$

in the matter dominated era, and

$$\mathcal{H}_\Lambda = \left(\frac{d\mathcal{H}}{dx}\right)_\Lambda = \left(\frac{d^2\mathcal{H}}{dx^2}\right)_\Lambda = H_0 \sqrt{\Omega_{\Lambda 0}}e^{x}, \tag{2.56}$$

in the dark energy dominated era. From the latter it is obvious that

$$\left(\frac{1}{\mathcal{H}}\frac{d\mathcal{H}}{dx}\right)_\Lambda = \left(\frac{1}{\mathcal{H}}\frac{d^2\mathcal{H}}{dx^2}\right)_\Lambda = 1. \tag{2.57}$$

maybe move "to ensure..." and down to app.

2.1.4. Onset of acceleration

When analyzing a simulated CMB power spectrum and comparing it to observations, it is interesting to know when the expansion of the Universe started to accelerate. It is a well known fact that the expansion rate (governed by $\dot{a}$) is increasing as of today, and that we are in the early stage of a dark energy dominated era. We have the second Friedmann equation

$$\frac{\ddot{a}}{a} = -\frac{4\pi G}{3}\sum_i \rho_i \left(1 + 3w_i\right), \tag{2.58}$$

where the sum runs over all components (matter, radiation, etc.). The onset of acceleration occurs when $\ddot{a}$ switches sign, i.e., when

$$\sum_i \rho_i \left(1 + 3w_i\right) = 0. \tag{2.59}$$

Assuming that this happens well after the radiation dominated era, we can approximate this as

$$\rho_m(x_{\text{acc}}) - 2\rho_\Lambda(x_{\text{acc}}) = 0 \tag{2.60}$$

Using that the expression (2.10) for the density parameters at arbitrary a, we can rewrite eq. (2.60) to get

$$\Omega_{m0}e^{-3x_{\text{acc}}} = 2\Omega_{\Lambda 0} \quad \Leftrightarrow \quad x_{\text{acc}} = \frac{1}{3}\log\left(\frac{\Omega_{m0}}{2\Omega_{\Lambda 0}}\right). \tag{2.61}$$

This corresponds to a redshift

$$z_{\text{acc}} = \left(\frac{2\Omega_{\Lambda 0}}{\Omega_{m0}}\right)^{1/3} - 1. \tag{2.62}$$

Obviously, $t_{\text{acc}} < t_{m\Lambda}$, so we can make the same approximation this time, hence

$$t_{\text{acc}} = t_m(x_{\text{acc}}) = \frac{1}{3H_0}\left[\sqrt{\frac{2}{\Omega_{\Lambda 0}}} - \frac{\Omega_{r0}^{3/2}}{2\Omega_{m0}^2}\right], \tag{2.63}$$

with the conformal time being

$$\eta_{\text{acc}} = \eta_m(x_{\text{acc}}) = \frac{c}{H_0}\left[\frac{2^{5/6}}{\Omega_{m0}^{1/3}\Omega_{\Lambda 0}^{1/6}} - \frac{\sqrt{\Omega_{r0}}}{\Omega_{m0}}\right]. \tag{2.64}$$

rewrite this if appendix

2.1.5. The Universe today

It is of course a great consistency check to see if I am able to replicate the values for the age of the Universe and its horizon size today, and we can use the expressions derived above to do so. Following the approximations I have done up until this point, we have

$$t_0 \approx t_\Lambda(0) = \frac{1}{H_0 \sqrt{\Omega_{\Lambda 0}}} \left[\frac{2}{3} - \frac{1}{3} \log\left(\frac{\Omega_{m0}}{\Omega_{\Lambda 0}}\right) - \frac{\sqrt{\Omega_{\Lambda 0}}\Omega_{r0}^{3/2}}{6\Omega_{m0}^2} \right],$$
$$(2.65)$$

$$\eta_0 \approx \eta_\Lambda(0) = -\frac{c}{H_0} \left[\frac{1}{\sqrt{\Omega_{\Lambda 0}}} + \frac{\sqrt{\Omega_{r0}}}{\Omega_{m0}} - \frac{3}{\Omega_{m0}^{1/3}\Omega_{\Lambda 0}^{1/6}} \right]. \qquad (2.66)$$

as we know that we currently are in the beginning of a dark energy dominated era.

2.1.6. The χ^2-method

After having established the theoretical framework describing the evolution of the Universe, we now turn to how observational data can be used to constrain cosmological parameters. One of the most powerful tools for this is the study of Type Ia supernovae, which serve as standard candles for measuring the expansion history of the Universe. Given their intrinsic luminosity, the observed flux allows us to determine their luminosity distance d_L as a function of redshift z, providing a direct probe of the Universe's geometry and expansion.

To quantitatively compare theoretical models to observational data, we define the so-called chi-squared statistic:

$$\chi^2(h, \Omega_{m0}, \Omega_{k0}) = \sum_{i=1}^{N} \frac{\left[d_L(z_i, h, \Omega_{m0}, \Omega_{k0}) - d_L^{\text{obs}}(z_i) \right]^2}{\sigma_i^2}, \qquad (2.67)$$

where N is the number of data points, $d_L^{\text{obs}}(z_i)$ represents the measured luminosity distance at redshift z_i, and σ_i is the associated measurement uncertainty. This function quantifies how well a given set of parameters $(h, \Omega_{m0}, \Omega_{k0})$ fits the data: a lower χ^2 value corresponds to a better fit.

2.2. Implementation details

2.2.1. The fiducial model

As mentioned in section 1, I adopt the best-fit Planck 2018 cosmology (see Planck Collaboration et al. 2020) as my fiducial model, with values chosen within their stated uncertainties. This includes the following parameters:

$$h = 0.67,$$
$$T_{\text{CMB0}} = 2.7255 \, \text{K},$$
$$N_{\text{eff}} = 3.046,$$
$$\Omega_{b0} = 0.05,$$
$$\Omega_{\text{CDM0}} = 0.267,$$
$$\Omega_{k0} = 0.$$

Here, h is the dimensionless Hubble constant, which is related to the commonly presented Hubble constant through

$$H_0 = 100h \, \text{km s}^{-1} \, \text{Mpc}^{-1}. \qquad (2.68)$$

The photon and neutrino density parameters are easily calculated using the values for T_{CMB0} and N_{eff}, and since all the density parameters must sum up to unity, we have

$$\Omega_{\gamma 0} = 5.50896 \times 10^{-5},$$
$$\Omega_{\nu 0} = 3.81093 \times 10^{-5},$$
$$\Omega_{\Lambda 0} = 0.683.$$

2.2.2. Main program structure

As mentioned in section 1, all the code I have used is located on my GitHub repository. In this section I specify which files are relevant for this milestone, and roughly what they contain and how they should be implemented. All of the source codes, which are implemented in C++, are located in the `src` folder, including the main program `Main.cpp`. Naturally, the `scripts` folder contains Python scripts, wherein NumPy and Matplotlib are used for plotting and analyzing the results. The `data` and `results` folders contain data and outputs from the source code, respectively, in the form of `.txt` files, while figures are placed in `figs`. maybe remove folder info

The evolution of the conformal and cosmic times, Hubble parameter, density parameters and related quantities are computed using the `BackgroundCosmology` class, implemented in `BackgroundCosmology.cpp` and `BackgroundCosmology.h`. Necessary constants and units are defined in their SI-unit values in `Utils.h`, as well as some convenient data types. The fundamental equations governing the expansion are integrated numerically using a GSL-based ODE solver (see `ODESolver.cpp` and `ODESolver.h`). The solutions for $t(x)$ and $\eta(x)$ are stored at discrete values of x and are interpolated using cubic splines (see `Spline.cpp` and `Spline.h`) for efficient lookup, which also ensure smooth evaluations of these quantities at any redshift. This is implemented within the `BackgroundCosmology` class, and all results produced here are written to file and analyzed in `background.py`.

2.2.3. Initial conditions

To numerically solve for conformal time η and cosmic time t, we need appropriate initial conditions. Integrating from $x = -\infty$ (i.e., the Big Bang) is of course impossible, and we may therefore choose an early starting time x_{start} instead, and use the analytical approximations in the radiation-dominated era:

$$\eta(x_{\text{start}}) = \frac{c}{H_0 \sqrt{\Omega_{r0}e^{-2x_{\text{start}}}}} \approx \frac{c}{\mathcal{H}(x_{\text{start}})}, \qquad (2.69)$$

$$t(x_{\text{start}}) = \frac{1}{2H_0 \sqrt{\Omega_{r0}e^{-4x_{\text{start}}}}} \approx \frac{1}{2H(x_{\text{start}})}. \qquad (2.70)$$

This ensures a smooth transition between analytical and numerical solutions, minimizing errors when solving for the full evolution of $\eta(x)$ and $t(x)$.

2.2.4. Integration limits and points

When integrating to solve for η and t, I chose to use $x_{\min} = -21.0$ and $x_{\max} = 6.0$ as integration limits, with $n = 1\,000$ points. However, when splining the results I used $x_{\min} = -20.0$ and $x_{\max} = 5.0$ instead, so as to not include the likely more unstable endpoints, with $n = 2\,501$ points (corresponding to $\Delta x = 0.01$) for smoother visualization.
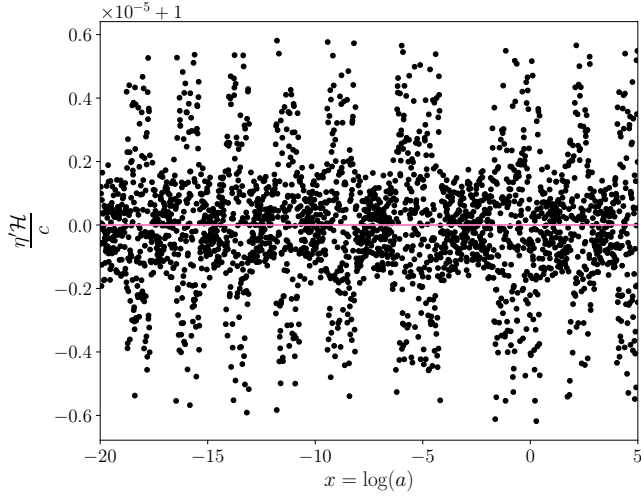
Fig. 2.1. Comparison of the numerically computed conformal time derivative $\eta'\mathcal{H}/c$ with the expected value of 1 (pink line). The small deviations on the order of $\lesssim 10^{-5}$ confirm the numerical stability of the integration.
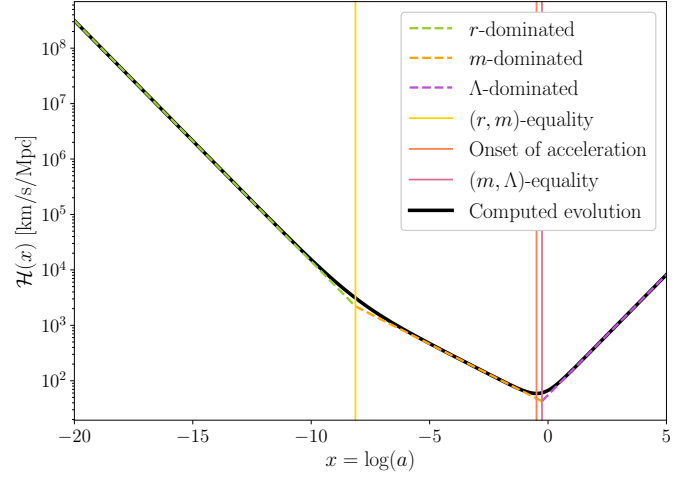
Fig. 2.2. Exact evolution of the conformal Hubble parameter $\mathcal{H}(x)$ (black) compared with approximations (dashed). The onset of acceleration is visible as a departure from matter-like scaling, occuring at the trough of the exact solution.

2.2.5. Supernova fitting

To constrain cosmological parameters $(h, \Omega_{m0}, \Omega_{k0})$, I performed a Markov Chain Monte Carlo (MCMC) fit to Type Ia supernova data (see `supernovadata.txt`), which is implemented in `SupernovaFitting.h`. The MCMC chain consists of 10 000 samples, where I have treated the 200 first samples are as burn-in time and thus discarded them. The results are further analyzed in `supernova.py`, where I visualize the accepted samples within the $(\chi^2 - \chi^2_{\min}) < 1\sigma$ and $(\chi^2 - \chi^2_{\min}) < 2\sigma$, constraints in the $(\Omega_{m0}, \Omega_{\Lambda0})$-plane, corresponding to 68.3% and 95.45% confidence levels, repsectively. I use tabulated values of $1\sigma = 3.53$ and $2\sigma = 8.02$ (see Reid Accessed: February 2025), since we have $k = 3$ degrees of freedom. This is because we really have four parameters $(h, \Omega_{m0}, \Omega_{k0}, \Omega_{\Lambda0})$, but also the constraint that all the density parameters must sum up to unity, which eliminates one d.o.f.

2.2.6. Testing the code

To test the stability of the numerical solutions presented in the following section, I have plotted $\eta'\mathcal{H}/c$ as function of x in figure 2.1, since this quantity should remain close to unity throughout the range. The scatter points, which were obtained by taking the derivative of the spline for η, show small deviations from 1, on the order of $\lesssim 10^{-5}$, indicating that the numerical error is very small. It also remains bounded throughout the range of x, suggesting that the ODE solver maintains stability and does not accumulate significant numerical drift. The slight periodic variations could result from finite step sizes in the integration, or have something to do with interpolation errors between the integration points, but they are well within an acceptable tolerance.

As an additional test of the code, I ran it using a set of toy cosmological parameters chosen to match those used by Winther et al. (Accessed: June 2025). The parameters are $h = 0.7$, $\Omega_{\mathrm{CDM}0} = 0.45$, $\Omega_{b0} = 0.05$, $\Omega_{k0} = 0$, $N_{\mathrm{eff}} = 0$ (implying $\Omega_{\nu0} = 0$), and $T_{\mathrm{CMB}0} = 0.27255$, K, as in the fiducial model. The resulting plots, shown in figures A.1, A.2, and A.3 in appendix A, are visually indistinguishable from those published by Winther. This provides strong validation for the accuracy and reliability of the implementation.

2.3. Results and discussions

2.3.1. The conformal Hubble parameter

In figure 2.2 I have plotted the exact evolution of the conformal Hubble parameter $\mathcal{H}(x)$ (black solid line), with approximations in the different cosmological epochs overplotted (dashed lines). Green, orange and purple correspond to radiation-, matter- and dark energy-dominated eras, respectively, with the yellow, red and pink vertical lines marking radiation-matter equality, onset of acceleration, and matter-dark energy equality. We see that the approximations closely follow the exact solution, staying at the correct order of magnitude at all times, although the deviations are significant close to the equality times. These are of course to be expected, since the approximations were derived under the assumption of the Universe only containing the dominating component within the different eras, which of course is not realistic as we transition from one to another. Thus, the result is still a great validation for the approximations, which indicates that we can safely use them to verify the numerical solutions for η and t.

A more direct comparison between the approximations and the exact evolution can be seen in figure 2.3, where I have plotted the first (left) and second (right) derivatives of $\mathcal{H}$ with respect to x, divided by $\mathcal{H}$ to see relative differences more easily. The dashed lines of different colors represent the same things here as well. We see good agreement in the asymptotically radiation-dominated and dark energy-dominated regimes, while in the matter-dominated epoch and around the equality times there are clear deviations, especially for the double derivative. This is reasonable, as we make rough approximations in both the beginning and the end of this era, hence the exact solution barely has time to sink to the expected value before it rises at the next transition point.

It is interesting to see that the scaled double derivative actually increases beyond the expected value in the beginning of the dark energy-dominated era, with the peak being today. To understand this, we can look back at eqs. (2.17) and (2.18). The latter shows that the second derivative is influenced by a competition
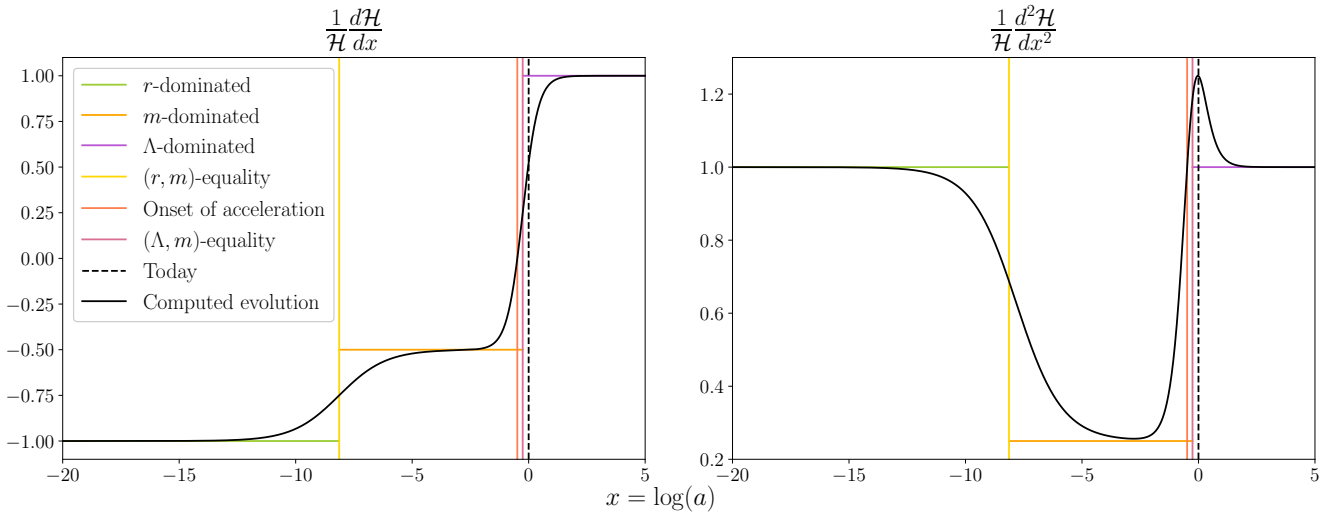
Fig. 2.3. Comparison of exact evolutions (black) with approximations (dashed) for the scaled first and second derivatives of $\mathcal{H}(x)$. Agreement is good in pure radiation and matter domination but deviates near transitions due to neglected components.

between growing and decaying terms as the Universe evolves: During the matter-dominated era, the dominant term is $\Omega_{m0}e^{-x}$, which leads to a slow decrease in $\mathcal{H}$; as Λ begins to dominate, the exponential growth of the $2\Omega_{\Lambda 0}e^{2x}$ term starts accelerating the Universe. The transition is not instantaneous, meaning there is a period where the competing effects of matter dilution (e^{-x}) and dark energy growth (e^{2x}) cause a rapid shift in dynamics. This is visible in the sharp turn of $\mathcal{H}$ in figure 2.2, and explains the peak in the scaled second derivative before it settles into the Λ-dominated regime.

2.3.2. Time and horizon measures

In figure 2.4 I have plotted the numerical solutions for the conformal time η/c (grey) and the cosmic time t (black) as functions of x, with the approximate analytical solutions presented in section 2.1 overplotted with dashed lines. The two bottom subplots, where the cosmic time is in focus, are included to easily be able to study what happens where the discrepancies between the numerical and analytical solutions are most drastic: where the Universe transitions from being dominated by one component to another. As expected, we see that the analytical approximation starts to deviate from the numerical curve as we approach (r, m)-equality, and eventually meets it again after. This happens also for the (m, Λ)-equality, but here the deviation actually continues to grow before it falls down again.

In table 2.1 I have listed key cosmological timestamps for important transition points in the Universe's history: radiation-matter equality, the onset of acceleration, matter-dark energy equality, and present-day values. The logarithmic scale factor $x = \log(a)$ and redshift z are listed for each event, along with analytical and numerical results for cosmic time t, conformal time η/c, and the comoving horizon η. We observe a discrepancy between the analytically approximated values for t and η obtained using the expressions derived in section 2.1 and the corresponding numerical values, which instead were obtained by solving the full system of equations and interpolating via splines. These discrepancies are consistent with figure 2.4.

<mark>compare r-m eq w/ Planck!</mark>

In Planck Collaboration et al. (2020), one presented estimate of the age of the Universe is $t_0 = 13.801 \pm 0.024$ Gyr. This

is based on 1σ constraints on a combination of gravitational lensing and TT (temperature), TE (temperature-E mode polarization), EE (E mode polarization) and lowE (low multipole E-mode polarization) angular power spectra measurements. This is in good agreement with the numerical result, although the value stated here is slightly larger. Nevertheless, the analytical approximation greatly overestimate it in comparison. This further validates the numerical solution around the equality times, where it deviates from the approximate evolutions and we have less to compare it to.

2.3.3. Density parameters

The evolutions of the density parameters $\Omega_i(x)$ are plotted in figure 2.5, with solid lines for Ω_r, Ω_m and Ω_Λ, and dashed lines for the individual components that make up the two first of these. The solid curves are consistent with the previous results, with the transitions between the different eras matching the observed changes in $\mathcal{H}$, η and t. For example, the abrupt change in the conformal Hubble parameter at (m, Λ)-equality compared to the change at (r, m)-equality matches the relatively rapid takeover of Λ as the dominating energy component, as opposed to the more gradual change from radiation to matter domination.

2.3.4. Supernova fitting

When running the MCMC fits, the minimum chi-squared value obtained was $\chi^2_{\min} = 29.2867$, corresponding to the parameter values listed in the third column of table 2.2. The means μ_i and standard deviations σ_i (where i runs over the parameters) computed for the samples within the 1σ constraints are listed as well, in addition to the Planck parameters stated in Planck Collaboration et al. (2020) for comparison. Interestingly, the supernova measurements favor a slightly open universe, deviating from the Planck result of a flat universe. However, the standard deviation, which is about three times larger than the best-fit value, suggests that the data does not strongly constrain curvature. We also see that the Planck result for Ω_{m0} is higher than the best-fit value, though it is within the $1\sigma_m$ confidence interval.

After obtaining the best-fit values I made a new instance of `BackgroundCosmology` with these parameters and solved for
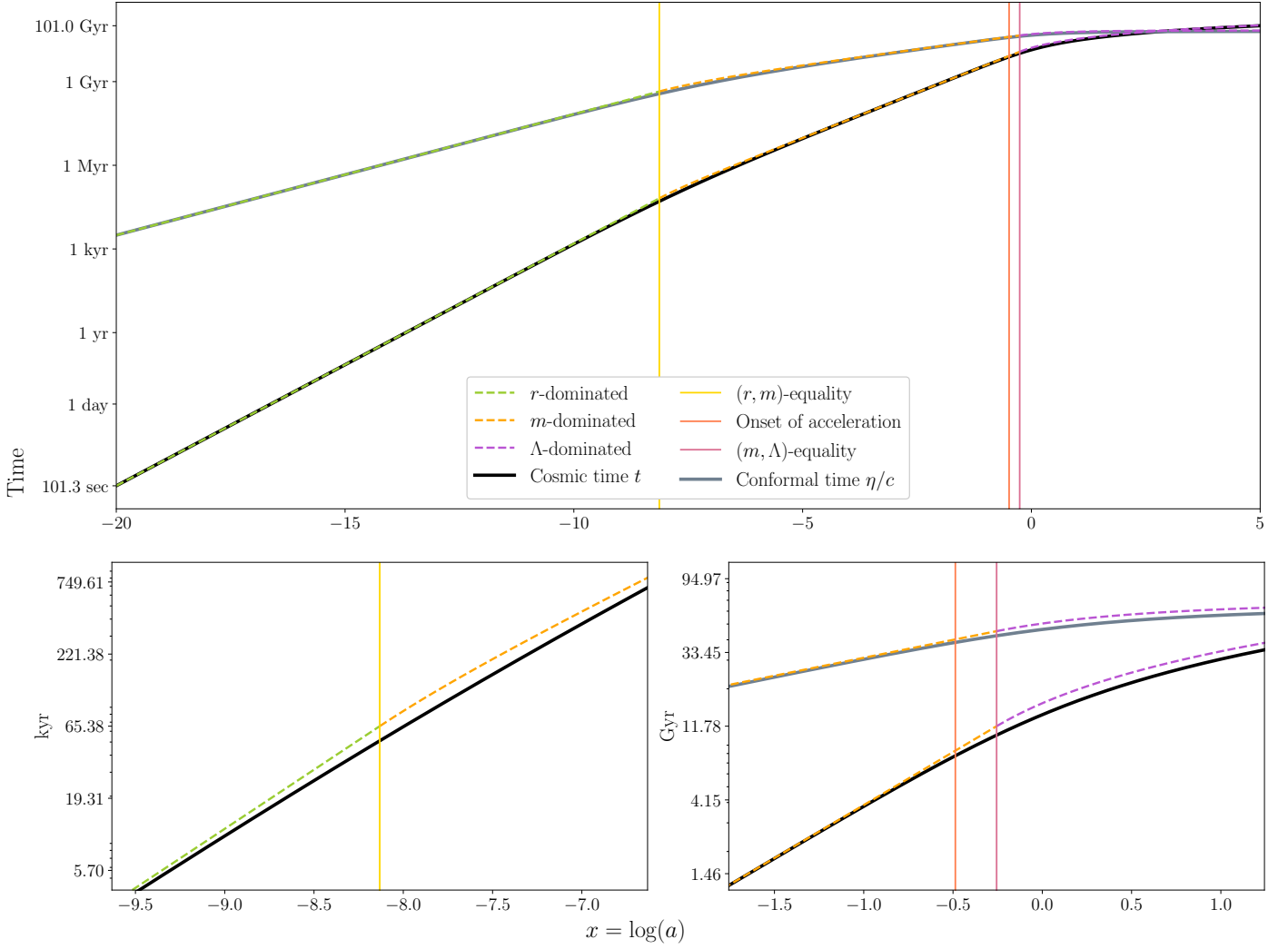
Fig. 2.4. Conformal time $\eta(x)$ (grey) and cosmic time $t(x)$ (black) compared with analytical approximations (dashed). Deviations near equality points arise due to gradual transitions between dominant energy components. This is highlighted in the bottom subplots for the cosmic time.

Table 2.1. Key cosmological timestamps at radiation-matter equality, the onset of acceleration, matter-dark energy equality, and present-day values. The analytical values are obtained using approximations from the theory section, while the numerical values are extracted from splines after solving the full system of equations. Discrepancies between the two highlight the limitations of the analytical approximations, especially during transition epochs.

	Radiation-matter equality	Onset of acceleration	Matter-dark energy equality	Present day values
x	-8.13	-0.49	-0.26	0
z	3400.33	0.63	0.29	0
t (analytical)	$65.38\,\mathrm{kyr}$	$8.33\,\mathrm{Gyr}$	$11.78\,\mathrm{Gyr}$	$16.30\,\mathrm{Gyr}$
t (numerical)	$51.06\,\mathrm{kyr}$	$7.75\,\mathrm{Gyr}$	$10.38\,\mathrm{Gyr}$	$13.86\,\mathrm{Gyr}$
η/c (analytical)	$444.75\,\mathrm{Myr}$	$40.22\,\mathrm{Gyr}$	$45.20\,\mathrm{Gyr}$	$50.36\,\mathrm{Gyr}$
η/c (numerical)	$368.44\,\mathrm{Myr}$	$38.57\,\mathrm{Gyr}$	$42.37\,\mathrm{Gyr}$	$46.32\,\mathrm{Gyr}$
η (analytical)	$136.27\,\mathrm{Mpc}$	$12.32\,\mathrm{Gpc}$	$13.85\,\mathrm{Gpc}$	$15.43\,\mathrm{Gpc}$
η (numerical)	$112.89\,\mathrm{Mpc}$	$11.82\,\mathrm{Gpc}$	$12.98\,\mathrm{Gpc}$	$14.19\,\mathrm{Gpc}$

this universe as well. In figure 2.6 I have plotted the scaled luminosity distance d_L/z against z for this best-fit cosmology (black curve) as well as the Planck cosmology (grey curve), together with the data points d_L^{obs}/z with scaled errorbars (pink). We see that the best-fit cosmology aligns much better with the data points than the Planck model, as the latter does not always lie within the supernova errorbars. This reflects the fact that the Planck data prefers a flat universe, whereas the best-fit suggests slightly negative curvature, which alters the distance-redshift relation. It also highlights tensions between low-redshift and high-redshift cosmological probes (see e.g. Reiss et al. (2024) for a recent discussion of this so-called Hubble tension in light of JWST
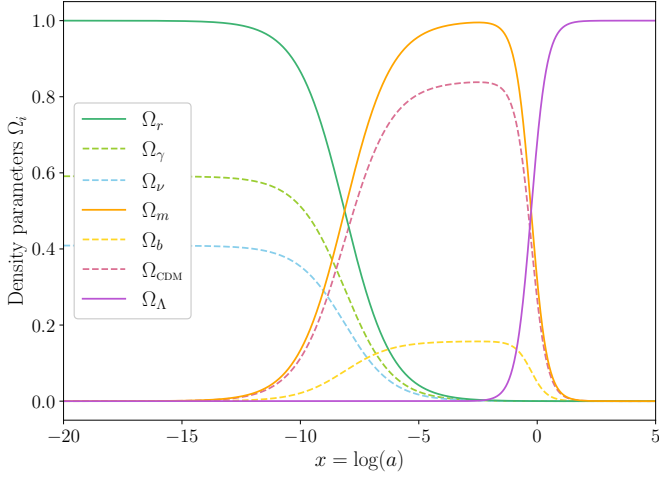
Fig. 2.5. The fractional energy densities of radiation, matter, and dark energy as functions of x (solid lines). The dashed lines show the evolutions of the radiation components (photons and neutrinos) and matter components (baryons and dark matter).

Table 2.2. Best-fit cosmological parameters obtained from supernova data, along with their mean values and standard deviations. The best-fit values correspond to the minimum χ^2, while the Planck 2018 values estimated from 1σ constraints on TT,TE,EE+lowE+lensing measurements are provided for comparison. These were determined by assuming a perfectly flat Universe, though they do actually estimate a small non-zero curvature density ($\Omega_{k0} = 0.0007 \pm 0.0019$) when relaxing this assumption and also including BAO measurements. I have chosen to neglect this in my analysis, due to the relatively small value and large uncertainty. <mark>move to main text?</mark> Moreover, the Hubble constant is given in units of km/s/Mpc.

	μ_i	σ_i	$\min(\chi^2)$	Planck
H_0	70.1	0.5	70.2	67.4 ± 0.5
Ω_{m0}	0.240	0.087	0.258	0.315 ± 0.007
Ω_{k0}	0.12	0.22	0.07	0
$\Omega_{\Lambda0}$	0.642	0.133	0.672	0.685 ± 0.007
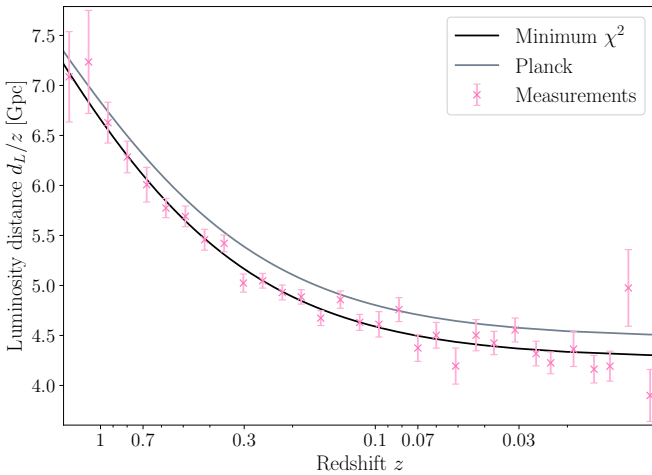
Fig. 2.6. Comparison of the luminosity distances d_L^{obs}/z gathered from supernova observations (pink with errorbars) with the fiducial Planck model (grey) and the best-fit model from MCMC analysis (black).
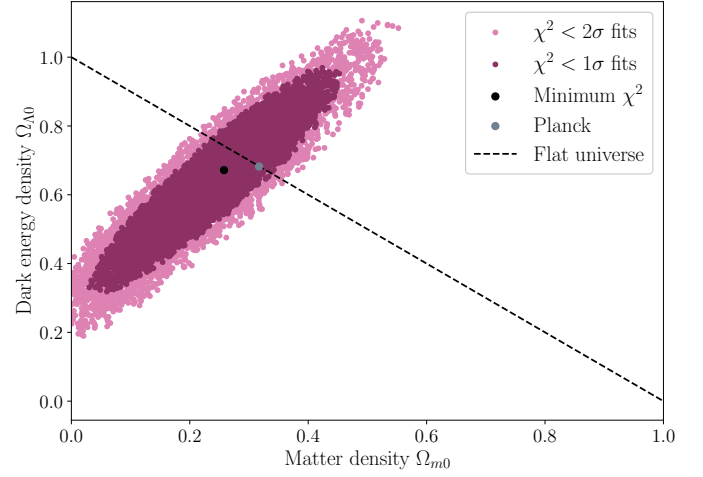

Fig. 2.7. Confidence contours in the $(\Omega_{m0}, \Omega_{\Lambda0})$ parameter space from the supernova MCMC analysis, compared to the Planck fiducial model. The supernova constraints allow for a slightly open universe, while Planck favors flatness based on multi-probe data.

observations). However, it should be kept in mind that measurements of supernova magnitudes can be affected by calibration uncertainties, host galaxy effects and dust extinction, potentially shifting best-fit cosmological parameters. Nevertheless, the discrepancies underscore the importance of using multiple probes and datasets to break parameter degeneracies and obtain a more complete picture of cosmic expansion.

In figure 2.7 I have scatter plotted the accepted $(\Omega_{m0}, \Omega_{\Lambda0})$ samples within the 1σ and 2σ constraints, with the black (grey) data point showing the best-fit (Planck) parameter set, and the dashed line showing the combinations that allow for a flat universe. We see clearly here that supernova-only constraints allow for slightly different cosmologies than the Planck model, with a preference for a lower matter density and small negative curvature. The Planck data includes additional information from the early universe, leading to a tighter preference for a flat universe with more mass. This discrepancy ties directly to the luminosity distance plot, confirming that these best-fit supernova parameters slightly differ from Planck's and further highlighting the importance of combining multiple datasets for robust cosmological constraints.

Figure 2.8 shows normalized histograms of the samples within the 1σ constraint, with Gaussian fits made with the μ_i and σ_i overplotted to represent the posterior distributions. Most noticeable is how different the supernova and Planck results are for H_0, with the smallest accepted 1σ samples being as large as 69 km/s/Mpc. Planck's estimate is derived from early universe physics (CMB, baryon acoustic oscillations and large-scale structure), while supernova constraints come from low-redshift expansion. The discrepancy may therefore indicate new and/or unknown physics present at some eras of the expansion history (see Reiss et al. (2024), but also Cortês & Liddle (2024) for critical discussions on tensions as indicators of new physics), or possibly systematic errors in one or both datasets. Moreover, we see that the supernova-only constraint clearly prefers a lower matter density compared than the Planck estimate, consistent with the MCMC contour plot.

The posterior distribution suggests a preference for a slightly open universe, though with considerable uncertainty. This deviation from flatness may arise because supernovae alone do not
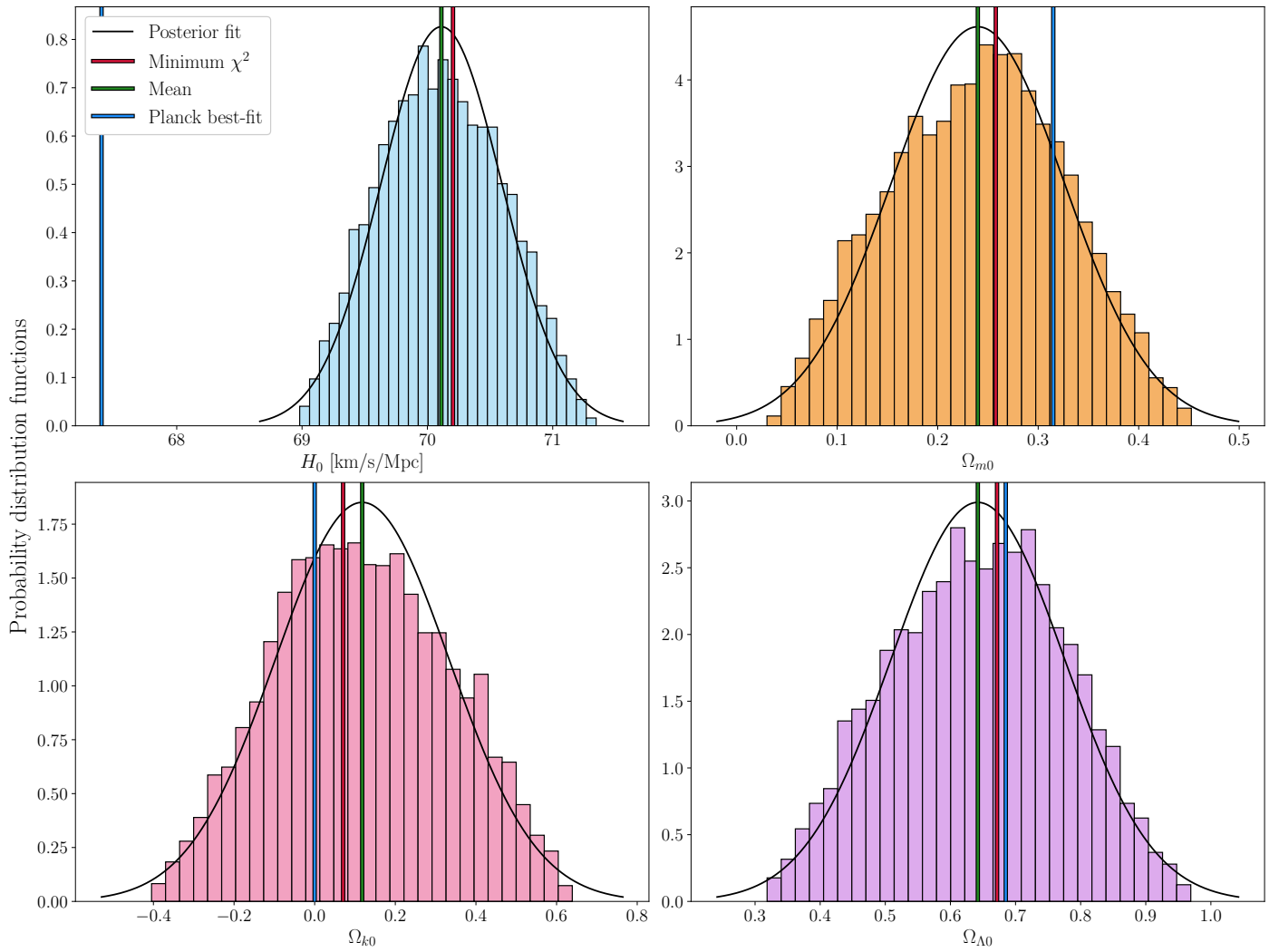
Fig. 2.8. Histograms of the MCMC posterior distributions for the parameters ($H_0, \Omega_{m0}, \Omega_{k0}, \Omega_{\Lambda0}$), compared with Gaussian fits (solid curves) and Planck values. Deviations from Gaussianity indicate asymmetries in parameter uncertainties.

tightly constrain curvature, as they primarily measure relative distances, not absolute spatial curvature. Moreover, we see that the histograms are not perfectly Gaussian, particularly those for Ω_{m0} and Ω_{k0}. Specifically, the asymmetry with more samples in the low mass/negative curvature ends may suggest a skewed uncertainty, indicating that a simple Gaussian error estimate might underestimate the possible range of accepted values.

<mark>maybe remove/argue for good in ast. standards</mark>

3. Milestone II: Recombination History

I got feedback on this paragraph from the milestone II intro, saying it was good but that initial conditions was not a good word to use in the last sentence. Can you suggest an alternative?

In the previous milestone, I established a numerical framework for solving the background evolution of the Universe, validating the results against analytical approximations and observational constraints. This provided a foundation for understanding the expansion history and cosmic distances, key ingredients in interpreting cosmological data. However, to model the formation of the CMB and its anisotropies, we must now extend the analysis to include recombination history: the period when the Universe transitioned from an ionized plasma to a neutral state, allowing photons to decouple from matter. This process deter-

mines the surface of last scattering, setting the conditions at decoupling that shape the CMB fluctuations we observe today.

In this milestone, I compute the recombination and reionization history by solving the Saha and Peebles equations, track the evolution of the optical depth $\tau(x)$, and derive the visibility function $\tilde{g}(x)$, which quantifies when CMB photons last interacted with free electrons. These quantities are essential for accurately modeling the temperature and polarization anisotropies of the CMB in the next milestones. Additionally, I compute the sound horizon at decoupling, a fundamental scale imprinted in the CMB power spectrum. This milestone bridges the gap between background cosmology and perturbation theory, ensuring that my model of the early Universe correctly captures the physics governing photon-matter interactions before recombination.

3.1. Theoretical framework

3.1.1. The Boltzmann equation and interactions

In cosmology, the evolution of particle species is governed by their phase-space distribution function, which in thermal equi-

librium takes the following form:

$$f(E) = \frac{1}{e^{(E-\mu)/T} \pm 1}. \tag{3.1}$$

Here, E is the energy of the particle, μ is the chemical potential, and T is the temperature of the system. The plus sign corresponds to the Fermi-Dirac distribution, and the minus sign to the Bose-Einstein distribution, which apply to fermions and bosons, respectively. For non-relativistic particles ($E \gg T$), the exponential terms in the denominator dominate, leading to the classical Maxwell-Boltzmann distribution:

$$f(E) \approx e^{-(E-\mu)/T}. \tag{3.2}$$

This approximation is valid for massive species that are thermally decoupled or at sufficiently low temperatures. It plays a crucial role in describing the abundance of baryons and cold dark matter in the late Universe.

The phase-space distribution function is the fundamental quantity from which one can compute physical observables such as number densities, energy densities, and momenta. Its time evolution is governed by the Boltzmann equation, which describes how particles respond to the expansion of the Universe and interact with each other. In general relativity, this equation is written in terms of an affine parameter λ as:

$$\frac{df}{d\lambda} = C[f], \tag{3.3}$$

where $C[f]$ is the collision term, which is is generally obtained from quantum field theory and encodes interactions between particles. In a homogeneous and isotropic universe, it vanishes when species are in thermal equilibrium, as detailed balance ensures that the rate of interactions maintains the equilibrium distribution.

In cosmology, we primarily consider $1 + 2 \leftrightarrows 3 + 4$ interactions, where the most crucial to consider are Compton scattering of photons off electrons, Coulomb scattering of electrons off protons, and Hydrogen recombination and ionization:

$$e^- + \gamma \leftrightarrows e^- + \gamma, \tag{3.4}$$
$$e^- + p \leftrightarrows e^- + p, \tag{3.5}$$
$$e^- + p \leftrightarrows H + \gamma. \tag{3.6}$$

The most relevant interaction for computing the CMB is Compton scattering in its low-energy (Thomson) limit, as this governs the coupling between electrons and photons in the early Universe. It is thus crucial for the optical depth, a quantity I introduce in section 3.1.6 that will prove to be essential as we move on to perturbations. Moreover, Coulomb scattering is only indirectly important, as its strength ensures that we can treat electrons and protons as a single particle species (baryons). Lastly, Hydrogen (as well as Helium) recombination and ionization is crucial for the recombination history. This is studied more in detail in sections 3.1.3 through 3.1.5.

3.1.2. Mass fractions

Rather than tracking the absolute number densities of different particle species, it is convenient to define mass fractions to describe relative species abundances. The most important of these is the free electron fraction, defined as

$$X_e = \frac{n_e}{n_H}, \tag{3.7}$$

where n_e is the number density of free electrons and n_H is the number density of Hydrogen nuclei (both ionized and neutral).

Since Helium is also present in the early Universe, we define the primordial Helium mass fraction Y_p, which represents the fraction of baryonic mass in Helium:

$$Y_p = \frac{m_{He}n_{He}}{m_b n_b} = \frac{4n_{He}}{n_b}, \tag{3.8}$$

where n_{He} is the number density of Helium nuclei and

$$n_b \approx \frac{\rho_b}{m_H} = \frac{\Omega_{b0}\rho_{c0}}{m_H a^3}, \tag{3.9}$$

is the total baryon number density. The factor of 4 in eq. (3.8) accounts for the fact that Helium nuclei (Helium-4) have four nucleons each. The number density of Hydrogen can easily be expressed in terms of Y_p, as all other elements are negligible for our purposes:

$$n_H = n_b - 4n_{He} = (1 - Y_p)n_b. \tag{3.10}$$

To fully describe the ionization state of the Universe, it is also necessary to introduce the ionization fractions of Hydrogen and Helium:

$$x_{H+} = \frac{n_{H^+}}{n_H}, \tag{3.11}$$
$$x_{He+} = \frac{n_{He^+}}{n_{He}}, \tag{3.12}$$
$$x_{He++} = \frac{n_{He^{++}}}{n_{He}}. \tag{3.13}$$

Here, x_{H+} represents the fraction of ionized Hydrogen, while x_{He+} and x_{He++} describe singly and doubly ionized Helium, respectively. These mass fractions allow for efficient tracking of the recombination process. When including Helium, the free electron number density is given by

$$n_e = 2n_{He++} + n_{He+} + n_{H+}, \tag{3.14}$$

which can be rewritten as

$$\frac{n_e}{n_b} = (2x_{He++} + x_{He+})\frac{Y_p}{4} + x_{H+}(1 - Y_p) \equiv f_e. \tag{3.15}$$

The free electron fraction is related to this by:

$$X_e = \frac{f_e}{1 - Y_p}. \tag{3.16}$$

3.1.3. The Saha approximation

To determine how recombination proceeds, we need to quantify the balance between ionization and recombination processes in the early Universe. The evolution of number densities is governed by the Boltzmann equation, and for a general interaction of the type $1 + 2 \leftrightarrows 3 + 4$ it can be shown that this takes the following form:

$$\frac{1}{a^3}\frac{d(n_1 a^3)}{dt} = -\alpha n_1 n_2 + \beta n_3 n_4. \tag{3.17}$$

Here, $\alpha = \langle \sigma v \rangle$ is the thermally averaged cross-section for the interaction, while β is related to α through equilibrium conditions:

$$\beta = \alpha \left(\frac{n_1 n_2}{n_3 n_4}\right)_{eq}. \tag{3.18}$$

If equilibrium holds, the right-hand side must vanish, and we obtain an equation relating the equilibrium number densities.

The Saha equation provides an analytical expression for the ionization fraction in equilibrium, valid when the ionization and recombination rates are fast compared to the Hubble expansion rate. It follows from writing eq. (3.18) for the process specified in eq. (3.6) in terms of the free electron fraction X_e. However, in order to derive it we need the number density of a species in thermal equilibrium, which follows from the distribution functions (eq. (3.1)) in the non-relativistic limit $E \gg T$:

$$n_i = g_i \left(\frac{m_i k_{\mathrm{B}} T}{2\pi\hbar^2} \right)^{3/2} e^{-\epsilon_i / k_{\mathrm{B}} T}, \tag{3.19}$$

where g_i is the statistical degeneracy, m_i is the mass, and ϵ_i is the ionization energy. Using this, we obtain the standard Saha equation for Hydrogen recombination when ignoring Helium alltogether:

$$\frac{X_e^2}{1 - X_e} = \frac{1}{n_H} \left(\frac{m_e k_{\mathrm{B}} T}{2\pi\hbar^2} \right)^{3/2} e^{-\epsilon_0 / k_{\mathrm{B}} T}. \tag{3.20}$$

Here, $\epsilon_0 = 13.6\,\mathrm{eV}$ is the ionization energy of Hydrogen. This equation determines how the free electron fraction evolves with temperature, and is an excellent approximation when $X_e \approx 1$.

To compute the recombination history more accurately, we must account for Helium. Conveniently, the ionization history of Helium follows the same principles as for Hydrogen, and using the ionization fractions defined in section 3.1.2 we obtain three coupled Saha equations for Hydrogen and Helium recombination:

$$n_e \frac{x_{\mathrm{He+}}}{1 - x_{\mathrm{He+}} - x_{\mathrm{He++}}} = 2 \left(\frac{m_e k_{\mathrm{B}} T_b}{2\pi\hbar^2} \right)^{3/2} e^{-\chi_0 / k_{\mathrm{B}} T_b}, \tag{3.21}$$

$$n_e \frac{x_{\mathrm{He++}}}{x_{\mathrm{He+}}} = 4 \left(\frac{m_e k_{\mathrm{B}} T_b}{2\pi\hbar^2} \right)^{3/2} e^{-\chi_1 / k_{\mathrm{B}} T_b}, \tag{3.22}$$

$$n_e \frac{x_{\mathrm{H+}}}{1 - x_{\mathrm{H+}}} = \left(\frac{m_e k_{\mathrm{B}} T_b}{2\pi\hbar^2} \right)^{3/2} e^{-\epsilon_0 / k_{\mathrm{B}} T_b}. \tag{3.23}$$

Here, $\chi_0 = 24.5874\,\mathrm{eV}$ is the ionization energy of neutral Helium, and $\chi_1 = 4\epsilon_0 = 54.42279\,\mathrm{eV}$ is the ionization energy of singly ionized Helium.

Unlike Hydrogen recombination, which can be solved directly using the Saha equation, Helium recombination requires an iterative approach. Given an initial guess for $f_e \approx 1$, we may solve the three Saha equations algebraically for $x_{\mathrm{He++}}$, $x_{\mathrm{He+}}$ and $x_{\mathrm{H+}}$, then compute the corresponding value of f_e using eq. (3.15). This process should be repeated a few times, using the updated f_e as input for the next iteration, until convergence according to some threshold value is reached:

$$|f_e - f_{e,\mathrm{old}}| < \Delta f_{e,\mathrm{tol}}. \tag{3.24}$$

This ensures an accurate determination of the free electron fraction.

3.1.4. The Peebles equation

The Saha approximation provides an accurate description of recombination in the early stages when the ionization and recombination processes are in thermal equilibrium. However, as the universe expands and cools, the recombination rate slows down relative to the Hubble expansion, preventing the free electron fraction X_e from immediately following the equilibrium prediction.

To accurately model recombination at later times, when X_e is no longer very close to 1, we must instead use the Peebles equation, which describes the evolution of X_e in an out-of-equilibrium setting. This looks the same whether Helium is included or not, and is given by

$$\frac{dX_e}{dx} = \frac{C_r(T_b)}{H} \left[\beta(T_b)(1 - X_e) - n_{\mathrm{H}} \alpha^{(2)}(T_b) X_e^2 \right]. \tag{3.25}$$

Most of the quantities that appear in eq. (3.25) are derived from quantum field theory calculations, and I will simply state them and what they represent. First of all,

$$\alpha^{(2)}(T_b) = \frac{64\pi}{\sqrt{27\pi}} \left(\frac{\alpha}{m_e\hbar} \right)^2 \sqrt{\frac{\epsilon_0}{k_{\mathrm{B}} T_b}} \phi_2(T_b), \tag{3.26}$$

and

$$\alpha = \frac{m_e c}{\hbar} \sqrt{\frac{3\sigma_{\mathrm{T}}}{8\pi}} \simeq \frac{1}{137.0359992}, \tag{3.27}$$

are the effective recombination coefficient and the fine-structure constant, respectively, with σ_{T} being the cross-section for Thomson scattering, and the dimensionless function

$$\phi_2(T_b) = 0.448 \ln \left(\frac{\epsilon_0}{k_{\mathrm{B}} T_b} \right). \tag{3.28}$$

Furthermore,

$$\beta(T_b) = \alpha^{(2)}(T_b) \left(\frac{m_e k_{\mathrm{B}} T_b}{2\pi\hbar^2} \right)^{3/2} e^{-\epsilon_0 / k_{\mathrm{B}} T_b}, \tag{3.29}$$

is the recombination rate per unit volume, and

$$C_r = \frac{\Lambda_{2s \to 1s} + \Lambda_\alpha}{\Lambda_{2s \to 1s} + \Lambda_\alpha + \beta^{(2)}(T_b)}, \tag{3.30}$$

is the Peebles correction factor, which accounts for the fact that some recombinations result in excited Hydrogen states instead of directly producing neutral Hydrogen. In this expression, $\Lambda_{2s \to 1s} = 8.227\,\mathrm{s}^{-1}$ is the spontaneous two-photon decay rate of the Hydrogen $2s$ state, and

$$\Lambda_\alpha = \frac{H}{(8\pi)^2 n_{1s}} \left(\frac{3\epsilon_0 \hbar}{c} \right)^3, \tag{3.31}$$

is the Ly-α escape rate, which accounts for the fact that Ly-α photons can redshift out of resonance before being reabsorbed. Furthermore,

$$n_{1s} = (1 - X_e) n_{\mathrm{H}}, \tag{3.32}$$

is the number density of Hydrogen in the ground state, and

$$\beta^{(2)}(T_b) = \beta(T_b) e^{3\epsilon_0 / 4 k_{\mathrm{B}} T_b}, \tag{3.33}$$

is the modified photoionization rate from the $n = 2$ level, introduced in the Peebles model to account for the fact that only recombinations into the $n = 2$ state are considered, rather than the full statistical equilibrium among excited states.

3.1.5. Reionization

Although reionization was likely a complex and extended process, it can be accurately modeled using a simple hyperbolic tangent (tanh) function, as implemented in CAMB (Code for Anisotropies in the Microwave Background, see Lewis et al. (2000)). This approach provides a smooth transition of the free electron fraction X_e from its post-recombination value to a fully ionized state. The modified evolution of the free electron fraction is then given by:

$$X_e = X_e^{\text{Peebles}} + \frac{1 + f_{\text{He}}}{2} \left(1 + \tanh \frac{y_{\text{reion}} - y}{\Delta y_{\text{reion}}} \right), \tag{3.34}$$

where we define $y = (1 + z)^{3/2} = e^{-3x/2}$, and thus $y_{\text{reion}} = (1 + z_{\text{reion}})^{3/2}$ and $\Delta y_{\text{reion}} = \frac{3}{2} \sqrt{1 + z_{\text{reion}}} \Delta z_{\text{reion}}$. Here, z_{reion} is the redshift at which reionization is centered, and Δz_{reion} determines how quickly the transition occurs. These parameters are constrained by CMB data, particularly the large-scale E-mode polarization spectrum.

In eq. (3.34),

$$f_{\text{He}} = \frac{Y_p}{4(1 - Y_p)} \tag{3.35}$$

accounts for the contribution to the reionization process from singly and doubly ionized Helium. The former is assumed to contribute around the same time as Hydrogen reionization, hence the factor $(1 + f_{\text{He}})/2$. Furthermore, Helium likely underwent a second phase of reionization at later times, and this can be modelled by adding a second term:

$$\frac{f_{\text{He}}}{2} \left(1 + \tanh \frac{z_{\text{He,reion}} - z}{\Delta z_{\text{He,reion}}} \right). \tag{3.36}$$

Analogous to the primary reionization process, the parameters that determine the mid-point and duration of this second phase are $z_{\text{He,reion}}$ and $\Delta z_{\text{He,reion}}$, respectively. Though the contribution from Helium if not as crucial as that from Hydrogen, it is still essential to include if one wants to accurately model the thermal history of the Universe.

3.1.6. Optical depths and visibility functions

To understand how photons interact with matter during recombination, we need to study the optical depth, which quantifies the probability of a photon scattering as it travels through the Universe. It is a dimensionless quantity that describes the attenuation of intensity due to scattering. If a source emits radiation with an initial intensity I_0, then the observed intensity after traveling a distance x through a medium with optical depth τ is given by

$$I(x) = I_0 e^{-\tau(x)}. \tag{3.37}$$

If $\tau \gg 1$ we say that the medium is optically thick, meaning photons scatter many times before escaping. If $\tau \ll 1$ the medium is optically thin, allowing most photons to pass through unimpeded. It is common in cosmology to define $\tau = 1$ as the point of last scattering, where photons transition from being tightly coupled to propagating freely.

As mentioned in section 3.1.1, the primary source of opacity in the early Universe is Thomson scattering of photons off free electrons. Thus, the optical depth of photons at a given conformal time η is defined as the integrated Thomson scattering rate along the line of sight:

$$\tau(\eta) = \int_{\eta}^{\eta_0} n_e \sigma_{\text{T}} a d\eta'. \tag{3.38}$$

However, it is more conveniently written on differential form in terms of the chosen time variable x instead:

$$\tau'(x) = \frac{d\tau}{dx} = -\frac{cn_e \sigma_{\text{T}}}{H}, \tag{3.39}$$

which can easily be integrated numerically and splined so that we can compute $\tau(x)$. The second derivative of the optical depth, τ'', is also useful to compute from this, since it helps characterize the sharpness of changes in τ during important events in the thermal history, such as decoupling and reionization.

A related, but less critical quantity is the baryon optical depth, which quantifies the drag exerted on baryons due to interactions with photons. On differential form it is given by:

$$\tau_b'(x) = \frac{d\tau_b}{dx} = -\frac{cRn_e \sigma_{\text{T}}}{H} = R\frac{d\tau}{dx}, \tag{3.40}$$

where

$$R(x) = \frac{4\Omega_{\gamma 0}}{3\Omega_{b0} a} = \frac{4\Omega_{\gamma 0}}{3\Omega_{b0}} e^{-x}, \tag{3.41}$$

is the ratio of the photon and baryon energy densities. The point when baryons stop being significantly influenced by the drag from photons and start evolving under gravity alone is defined by $\tau_b = 1$, and the interval between the photon and baryon decoupling is referred to as the drag epoch. This delay plays an important role in the evolution of baryon acoustic oscillations (BAO). It primarily arises from the much higher number density of photons relative to baryons, which means that photons can continue to effectively drag baryons even after photon decoupling has begun.

Can you add a sentence saying that we also can analogously define a visibility function $\tilde{g}_b(x)$ derived from the baryon optical depth, which we won't necessarily need for further computations, but can be used for testing that $\tau_b(x)$ is integrated correctly?

The visibility function $\tilde{g}(x)$ gives the probability density that a CMB photon last scattered at time x and is defined as:

$$\tilde{g}(x) = -\frac{d\tau}{dx} e^{-\tau(x)}. \tag{3.42}$$

It peaks around photon decoupling, when $\tau(x) \approx 1$, marking the transition from frequent scattering to free-streaming. The width of this peak reflects how sharply defined the time of photon decoupling is, hence why it is commonly referred to as the surface of last scattering.

To ensure the correctness of the numerical implementation further on, it is also useful to compute the first and second derivatives of $\tilde{g}(x)$ with respect to x, as they play a central role in the expression for the source function used in the line-of-sight integration. This is is essential for computing the CMB spectrum, as we will see in section 5.1.2. Analogously, we can define a baryon visibility function $\tilde{g}_b(x)$ from the baryon optical depth. While we won't need this quantity in later calculations, it can serve as a useful check to verify that $\tau_b(x)$ has been integrated correctly.

3.1.7. The sound horizon

The maximum comoving distance that a sound wave in the primordial plasma could have propagated from the beginning of the Universe is reprented by the so-called sound horizon. It is defined as the integral of the sound speed over cosmic time:

$$s(x) = \int_0^t \frac{c_s(t')}{a(t')} dt' = \int_{-\infty}^x \frac{c_s(x')}{\mathcal{H}(x')} dx', \tag{3.43}$$

and is thus closely related to the particle horizon (eq. (2.21)). Here, c_s is the speed of sound in the tightly coupled photon-baryon plasma, hence the speed of a pressure wave propagating in the primordial fluid. It is given by

$$c_s(x) = \frac{c}{\sqrt{3(1 + R(x))}}, \tag{3.44}$$

where $R(x)$ is defined as in eq. (3.41). At early times, photons dominate, and $c_s \approx c/\sqrt{3}$, but as the Universe expands and baryons become more influential, c_s decreases.

A crucial quantity when studying the CMB is the sound horizon at decoupling, r_s, as this length scale is directly imprinted on the temperature power spectrum. More specifically, a commonly computed quantity in studies of the CMB is the angular acoustic scale, given in terms of r_s and the comoving distance to the last scattering surface $\chi_s = \eta_0 - \eta_s$ as

$$\theta_s = \frac{r_s}{\chi_s}. \tag{3.45}$$

Furthermore, the sound horizon at baryon decoupling, r_{drag}, is relevant for baryon acoustic oscillations in the large-scale distribution of galaxies. Accurately computing both sound horizons is therefore essential for making precise predictions about the observed large-scale structure of the Universe.

3.1.8. Baryon temperature

A common approximation in cosmology is to assume that the baryon temperature T_b follows the photon temperature $T_\gamma = T_{\mathrm{CMB}}$ at all times due to rapid interactions between baryons and photons. However, Thomson scattering becomes too inefficient some time after decoupling, and the baryon temperature eventually starts evolving independently. Though this occurs relatively late in the recombination history, and thus has little effect on the CMB anisotropies, it is good to track the full evolution of T_b in order to to ensure accuracy in the predictions.

The baryon temperature is also governed by the Boltzmann equation, and in a smooth, homogeneous universe, its evolution is given by:

$$\frac{dT_b}{dx} = 2 \left[\frac{\mu(x)}{m_e} \frac{d\tau_b}{dx} (T_b - T_{\mathrm{CMB}}) - T_b \right], \tag{3.46}$$

Here, $\mu(x)$ is the mean molecular weight of baryons, including free electrons and all ions of Hydrogen and Helium, but it is a good approximation to simply set $\mu = m_{\mathrm{H}}$ at all times x.

Eq. (3.46) is numerically unstable at early times when $|d\tau/dx| \gg 1$, so it's convenient to introduce

$$y = \frac{T_b}{T_{\mathrm{CMB}}} - 1 \implies \frac{dy}{dx} = \frac{1}{T_{\mathrm{CMB}}} \left[\frac{dT_b}{dx} - (y+1) \frac{dT_{\mathrm{CMB}}}{dx} \right], \tag{3.47}$$

and solve for this variable instead. Using that $T_{\mathrm{CMB}} = T_{\mathrm{CMB}0} e^{-x}$, and inserting eq. (3.46) into eq. (3.47), we thus get the following differential equation for y:

$$\frac{dy}{dx} = 1 + y \left[2 \frac{m_{\mathrm{H}}}{m_e} \frac{d\tau_b}{dx} - 1 \right]. \tag{3.48}$$

3.2. Implementation details

3.2.1. The fiducial model

Adding to the cosmological parameters specified in section 2.2.1, I use the following parameters to compute the recombination and reionization history of the Universe:

$$Y_p = 0.245,$$
$$z_{\mathrm{reion}} = 8.0,$$
$$\Delta z_{\mathrm{reion}} = 0.5,$$
$$z_{\mathrm{He,reion}} = 3.5,$$
$$\Delta z_{\mathrm{He,reion}} = 0.5.$$

These are again based on best-fit values from the 2018 Planck results (see Planck Collaboration et al. 2020). They use a primordial Helium mass fraction of $Y_p = 0.2454$, the posterior mean predicted by Big Bang Nucleosynthesis, and state their estimate of the reionization redshift mid-point as $z_{\mathrm{reion}} = 7.82 \pm 0.71$ based on 1σ limits on TT,TE,EE+lowE+lensing+BAO measurements. When modelling reionization, the rest of the parameters they use are the same as those stated here.

3.2.2. Main program structure

The free electron fraction, electron density, optical depths with derivatives, visibility functions with derivatives, sound horizon, and baryon temperature are all computed in the class `RecombinationHistory`, implemented in the source code and header files of the same name. The same GSL-based ODE solver used previously is also used when solving for X_e (in the Peebles regime), τ, τ_b, $\tilde{g}$, $\tilde{g}_b$, s and T_b, and all of these solutions are interpolated using cubic splines. The results are written to file and visualized in `recombination.py`.

3.2.3. Initial conditions

In the numerical implementation of the recombination history, careful selection of initial conditions is crucial for stable and accurate integration. As we switch to the Peebles regime, the initial condition for X_e in eq. (3.25) is naturally the last value computed in the Saha regime. From this, the free electron density n_e is determined using the baryon number density n_b, which is computed separately from cosmological parameters (eq. (3.9)).

For the optical depth, both the photon optical depth τ and the baryon optical depth τ_b are defined to be zero today. Since the optical depth is an integral that accumulates from past times until today, it is advantageous to integrate backward in time. This avoids truncation errors near $x = 0$ and ensures an accurate computation of the visibility function.

The sound horizon $s(x)$ requires an initial condition at early times. As mentioned in section 3.1.7, it is closely related to the conformal time η, which in the radiation-dominated era follows an analytical approximation (see section 2.2.3). Following an analogous reasoning, the initial condition for $s(x)$ thus becomes

$$s(x_{\mathrm{start}}) = \frac{c_s(x_{\mathrm{start}})}{H_0 \sqrt{\Omega_{r0} e^{-2x_{\mathrm{start}}}}} \approx \frac{c_s(x_{\mathrm{start}})}{\mathcal{H}(x_{\mathrm{start}})}. \tag{3.49}$$

For the baryon temperature T_b, we initially set it equal to the photon temperature T_{CMB}. This is justified since Thomson scattering is highly efficient at maintaining thermal equilibrium between baryons and photons well into the Peebles regime. Since we solve for the variable $y = T_b/T_{\mathrm{CMB}} - 1$, this means the initial condition for y is set to zero.

3.2.4. Integration limits and points

To ensure numerical accuracy in later milestones, I began the integration at $x_{min} = -18.0$, even though no significant recombination-related transitions occur this early. The upper limit was chosen as $x_{max} = 0.0$, since the optical depth is conventionally defined to vanish at the present time, $\tau(x = 0) = 0$, making it a natural endpoint. For the Saha-only solution, I used 1 000 integration points, while for the combined Saha-Peebles calculation I increased this to 10 000 to ensure a smooth transition between the two regimes. When outputting the results I used the range $x \in [-12.0, 0.0]$ with 12 001 sampling points, corresponding to $\Delta x = 0.001$.

3.2.5. Tolerances

As mentioned in the previous section, I had to tune the number of integration points in order to avoid numerical instability in the transition between the Saha and Peebles regimes. Specifically, the double derivative of the optical depth suffers from discontinuities if either too few or too many points are chosen. Also, I found that transitioning to the Peebles regime too late lead to the same effect, and ended up using $X_e < 0.9999$ as criterion.

Although I have decided to include Helium, the code also works with $Y_p = 0$. In that case, eq. (3.20) is used in the Saha regime when computing X_e, which has positive root

$$X_e = \frac{b}{2}\left(-1 + \sqrt{1 + \frac{4}{b}}\right), \quad b = \frac{1}{n_b}\left(\frac{m_e T_b}{2\pi}\right)^{3/2} e^{-\epsilon_0/T_b}. \quad (3.50)$$

In the early Universe T_b is very large, hence $b \ll 1$ since the exponential term dominates. Thus, $4/b \approx 0$, which leads to $X_e = 0$. Obviously, this is not the case at early times, and be may expand the square root around $4/b = 0$ to get $X_e \approx b/2(-1+1+2/b) = 1$. This is only viable in the very beginning of solving the system, and I have therefore set a tolerance of $4/b > 10^{-3}$ for when the above expression can be used to compute X_e.

As mentioned in section 3.1.3, one must solve iteratively for f_e in the Saha regime when using a non-zero Helium abundance. I chose to set $f_e = 1$ and $f_{e,old} = 0$ to begin with, then use $\left|f_e - f_{e,old}\right| < 10^{-10}$ as stopping criterion to ensure that it had properly converged. This is not numerically challenging, so the low tolerance has negligible effect on the computation speed.

When solving for the baryon temperature T_b, we have a set of coupled differential equations for X_e and y in the Peebles regime becomes. The ODE for y is very stiff in the beginning, and since we expect the baryon and photon temperatures to be identical until well after recombination, I have chosen to simply set $T_b = T_{CMB}$ in the differential equation for X_e until some threshold value of x. This can be passed as an argument to the right-hand side method for the Peebles ODE, with default value `x_tol=-7.0` (which is what I have used to produce my results). Furthermore, to aid in the stability of the differential equations I have made it so that the absolute and relative tolerances of the ODE solver are changed from $\epsilon_{abs} = \epsilon_{rel} = 10^{-7}$ to $\epsilon_{abs} = \epsilon_{rel} = 10^{-12}$ in case we solve for T_b.

3.2.6. Testing the code

A good way to check that the computed quantities are reasonable is to compute the integral of $\tilde{g}$ and $\tilde{g}_b$ from x_{min} to x_{max}, since these are probability density functions and must therefore integrate up to unity. By summing the splined values and divid-

ing by the number of points used for integrating, I found that

$$\int_{x_{min}}^{x_{max}} \tilde{g}(x)\,dx = 1.0 + 9.4 \times 10^{-8},$$

$$\int_{x_{min}}^{x_{max}} \tilde{g}_b(x)\,dx = 1.0 + 6.9 \times 10^{-9}.$$

This greatly validates most of the numerical solutions, as the visibility functions depend on the optical depths, which in turn depend on the free electron fraction.

As in the previous milestone, I have produced comparison plots to benchmark the results against those provided by Winther et al. (Accessed: June 2025). Figures A.4, A.5, and A.6 in appendix A show the evolution of X_e, τ (with derivatives), and $\tilde{g}$ (with derivatives), respectively. These were generated using the same toy cosmology described in section 2.2.6, with the addition that Helium is ignored in all cases except the right panel of figure A.4, where $Y_p = 0.24$ is used. Reionization is also included in some runs, primarily using the fiducial parameters with the exception of $z_{reion} = 11.0$. Helium reionization is, naturally, only accounted for when $Y_p \neq 0$.

Overall, the plots show excellent agreement with Winther's results. The only noticeable discrepancy appears in the second derivative of the optical depth, τ'', which exhibits minor numerical instabilities around the transition from the Saha to Peebles regimes and near $x = 0$. Aside from this, the consistency strongly supports the robustness of the implementation.

3.3. Results and discussions

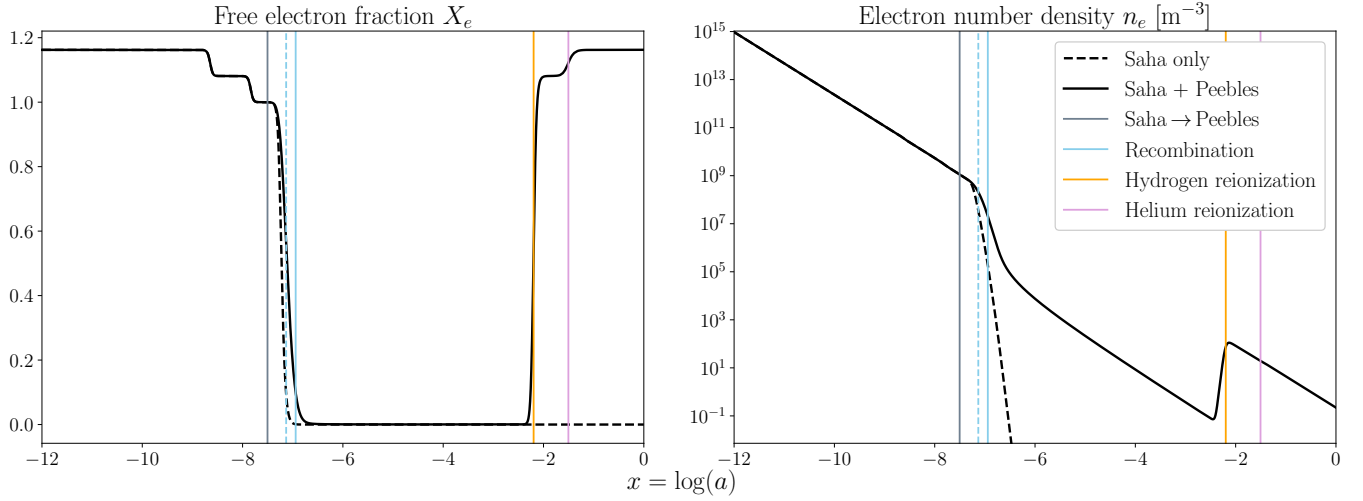#### 3.3.1. Electron fraction and number density

In figure 3.1, I have plotted the free electron fraction, X_e (left subplot), and the electron number density, n_e (right subplot), as functions of x. Initially, we observe that $X_e \lesssim 1.2$, reflecting a fully ionized Universe where both Hydrogen and Helium are ionized. The free electron fraction slightly exceeds 1 due to the contribution of Helium. As the Universe expands and cools, recombination progresses in stages. Around $x \approx -9$, doubly ionized Helium (He^{++}) captures an electron and transitions to singly ionized Helium (He$^+$). Shortly afterward, at $x \approx -8$, He$^+$ recombines into neutral Helium (He). Hydrogen recombination occurs later, around $x \approx -7$, where X_e undergoes a steep decline as most free electrons combine with protons to form neutral Hydrogen. This marks Hydrogen recombination as the dominant process in determining the final ionization state of the Universe.

The impact of these recombination events is also evident in the evolution of the electron number density. During Helium recombination, n_e follows the expected trend of volume dilution with no significant deviations, indicating that Helium recombination has a minimal effect on the overall number density. However, during Hydrogen recombination, n_e drops by approximately four orders of magnitude, demonstrating the rapid capture of electrons by protons. A similar trend can be seen at later times: although He$^+$ reionization leads to an increase in the free electron fraction, its effect on the total number density is negligible compared to the large increase that occurs during the first reionization period.

By turning off reionization, I determined the freeze-out abundance of free electrons to be:

$$X_e \approx 2.7 \times 10^{-4},$$

$$n_e \approx 5.2 \times 10^{-5}\,\text{m}^{-3}.$$

Fig. 3.1. The evolution of the free electron fraction X_e (left) and the free electron number density n_e (right) as functions of $x = \log(a)$. The dashed blue line marks the time of recombination estimated using only the Saha approximation, while the solid line shows the result from solving the Peebles equation. The significant difference illustrates the limitations of assuming equilibrium.

These values are consistent with standard recombination theory, which predicts a residual ionized fraction X_e on the order of 10^{-3} to 10^{-4}. Although this small asymptotic value is difficult to measure directly in today's highly reionized Universe, it plays an important role in our understanding of the thermal history between recombination and reionization. The presence of this residual electron population reflects both the continued existence of high-energy photons capable of reionizing hydrogen atoms and the low particle densities at late times, which reduce the likelihood of recombination events. As a result, a small fraction of electrons and protons remains unbound, preventing complete neutralization of the cosmic plasma.

3.3.2. Optical depths

Figure 3.2 shows the evolution of the photon (left) and baryon (right) optical depths (blue) and their first (red) and second derivatives (green) as functions of $x = \log(a)$. We see from the left panel that the photon optical depth τ is initially large, reflecting the fact that photons are tightly coupled to the baryon-electron plasma due to frequent Thomson scattering. Around decoupling we see a rapid drop in τ, since the photons stop noticing the baryons. This is also visible from the steep negative peak in $-\tau'$, which marks the rapid decline in the scattering probability.

The second derivative τ'' provides further insight into the recombination process. In particular, we see two smaller peaks just before the dominant Hydrogen recombination, corresponding to the transitions of $He^{++} \rightarrow He^+$ and $He^+ \rightarrow He$, which highlights the changes in the free electron fraction seen in figure 3.1. Though subtle, these peaks indicate sudden drops in $-\tau'$, demonstrating that X_e does not decrease monotonically but rather in distinct stages due to the sequential recombination of Helium and Hydrogen.

After recombination, τ levels off and remains nearly constant, meaning that photons are no longer frequently scattering. This corresponds to the transition to CMB free-streaming, where the photons released at decoupling travel largely undisturbed throughout the Universe. However, at $x \lesssim -2$ we observe a sudden increase in $-\tau'$, accompanied by a sharp drop in τ'', corresponding to Hydrogen reionization. This phase is driven by ionizing radiation from early stars, which rapidly increases

the free electron fraction, as reflected in the jumps in X_e and n_e in figure 3.1. The optical depth τ then enters a plateau. A second, smaller bump at $x \approx -1.5$ arises from Helium reionization, caused by high-energy photons from quasars that fully ionize singly ionized Helium (see e.g. Basu et al. (2024) for updated analyzes in light of recent JWST data).

To understand the reionization plateau, consider a photon emitted at aredshift $z < z_{reion}$. Since most Hydrogen is ionized, it has a non-negligible probability of Thomson scattering on its way to us. This probability accumulates over time, making the optical depth larger for photons emitted further in the past. However, for photons emitted in the neutral era between recombination and reionization ($z_{rec} \gg z > z_{reion}$), the scattering probability is negligible, leading to a roughly constant optical depth in this regime. The optical depth at reionization is often a more relevant quantity than the precise redshift of reionization. From my computed spline, I found this value to be $\tau_{reion} = 0.0561$, which perfectly matches the Planck 2018 result: based on TT,TE,EE+lowE+lensing+BAO measurements, Planck Collaboration et al. (2020) found $\tau_{reion} = 0.0561 \pm 0.0071$.

The baryon optical depth τ_b follows a similar evolution to the photon optical depth but starts from a significantly higher value. This reflects the large photon-to-baryon ratio, implying that baryons have an even shorter mean free path than photons in the tightly coupled plasma. Around decoupling, τ_b also undergoes a decline but does so more gradually due to the extended drag epoch, during which residual interactions between baryons and photons delay the onset of independent baryon motion. As seen in the photon case, Hydrogen and Helium reionization lead to a delayed but noticeable increase in τ_b', though the effect is less pronounced. Since baryons are non-relativistic, they are less affected by changes in the free electron fraction compared to photons, resulting in a weaker response to reionization.

3.3.3. The visibility function

In figure 3.3, I have plotted the photon visibility function $\tilde{g}(x)$ (top), its first derivative $\tilde{g}'(x)$ (middle), and second derivative $\tilde{g}''(x)$ (bottom) as functions of x. The interval $x \in [-12, -8]$ has been omitted, as all these quantities remain identically zero in this range. We see that the visibility function peaks sharply
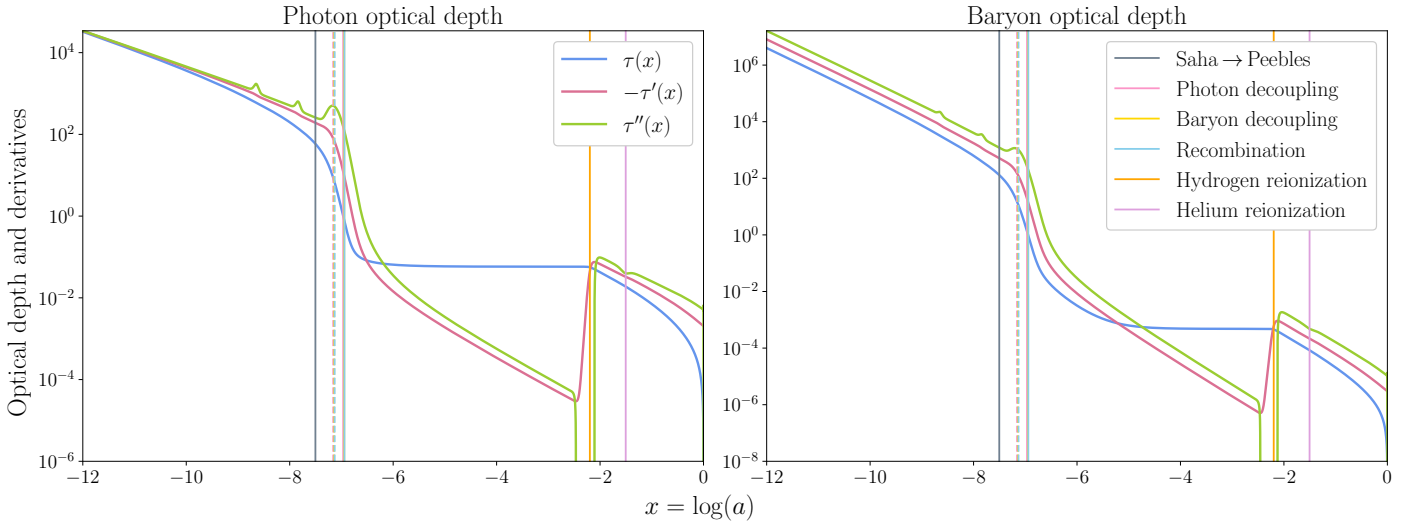
Fig. 3.2. The evolution of the optical depth τ (blue), its first derivative $-\tau'$ (red), and its second derivative τ'' (green) for both photons (left) and baryons (right). The sharp drop in τ marks photon decoupling, after which photons free-stream. In constrast, the gradual decline in τ_b indicates the prolonged influence of radiation pressure on baryons during the drag epoch.

around $x \approx -7$, confirming that the last scattering of CMB photons occurred near this time. As discussed in section 3.1.6, the width of the peak in $\tilde{g}(x)$ reflects the thickness of the last scattering surface, while the zero-crossing of $\tilde{g}'(x)$ indicates the time of steepest decline in scattering probability.

At later times, around $x \lesssim -2$, Hydrogen reionization causes a secondary, broader increase in $\tilde{g}(x)$, reflecting the renewed interaction between photons and free electrons. However, this increase is significantly smaller than at recombination, indicating that only a fraction of CMB photons were re-scattered during this epoch. The visibility function barely changes during the subsequent reionization of singly ionized Helium to doubly ionized Helium, as expected from the negligible impact of this process on the optical depths and their first derivatives.

3.3.4. Important time stamps and horizons

Table 3.1 presents the computed values of x, redshift z, cosmic time t, conformal time (particle horizon) η, and sound horizon s corresponding to photon and baryon decoupling, the changes that occured during the drag epoch in between the two, as well as recombination. The values are given both for calculations using only the Saha approximation and for the more accurate approach that includes the full Peebles equation. As expected, photon decoupling (where τ falls to unity) and recombination (when X_e drops below 0.1) occur at nearly identical times. This is because photons cease scattering once neutral Hydrogen forms, making the two processes tightly linked. However, recombination happens slightly later because a residual fraction of free electrons persists even after photons transition to free-streaming. Baryon decoupling occurs between the two, as evident from figures 3.2 and 3.3.

The Saha approximation alone predicts earlier times of recombination and decoupling, consistent with the steeper drop in the free electron fraction observed in figure 3.1. This discrepancy arises because the Saha equation assumes instantaneous thermal equilibrium, meaning ionization and recombination are treated as occurring instantaneously when crossing equilibrium thresholds. However, in reality, recombination is a non-equilibrium process, as captured by the Peebles equation, which accounts

for the slower capture of electrons by protons in an expanding universe.

The difference in sound horizons between the two approaches highlights the impact of an earlier recombination. Since sound waves in the tightly coupled photon-baryon plasma define the characteristic scale of acoustic oscillations, an earlier recombination results in a slightly smaller sound horizon. This has direct consequences for the CMB anisotropy spectrum, as the first acoustic peak corresponds to the largest mode that fits within the sound horizon at decoupling. A smaller sound horizon shifts the peak positions and alters the angular scale of the acoustic features in both the CMB power spectrum and the BAO in the matter power spectrum. This clearly demonstrates the necessity of using the Peebles equation to accurately model recombination, as relying on the Saha approximation alone leads to artificially early decoupling and incorrect predictions for the CMB and BAO scales.

Figure 3.4 illustrates the evolution of the sound horizon $s(x)$, with the estimated time of recombination marked to highlight where its growth gets stunted. In the early Universe, the sound horizon increases rapidly due to the high sound speed in the tightly coupled photon-baryon fluid. This is a direct consequence of the nearly relativistic equation of state of the plasma, where the sound speed c_s remains close to $c/\sqrt{3}$. However, around recombination, the pressure support from photons is significantly reduced, allowing matter to cluster more freely and leading to a decrease in the sound speed. Consequently, the growth of the sound horizon flattens out as baryons decouple from photons and begin falling into dark matter potential wells, setting the scale of BAO in the later Universe.

In Planck Collaboration et al. (2020), the estimated redshifts of photon and baryon decoupling are $z_s = 1089.92 \pm 0.25$ and $z_{drag} = 1059.94 \pm 0.30$, respectively, based on 1σ constraints from TT,TE,EE+lowE+lensing measurements. The corresponding sound horizons are $r_s = 144.43 \pm 0.26\,\mathrm{Mpc}$ and $r_{drag} = 149.09 \pm 0.26\,\mathrm{Mpc}$. My computed values for z_s and z_{drag} are systematically lower, although the resulting sound horizons—particularly r_{drag}—are in good agreement with the Planck results. This discrepancy in redshift does not necessarily indicate a numerical error but rather reflects a key difference in methodology: while I have computed these quantities using a fixed fiducial

Table 3.1. Table of key cosmological time stamps, showing photon and baryon decoupling, the changes that occur inbetween (the drag epoch), and recombination, along with their corresponding redshifts, cosmic times, conformal times (particle horizons), and sound horizons. The Saha-only results differ significantly from the full solution, underestimating recombination time due to its equilibrium assumption.

Quantity	Method	Photon decoupling	Baryon decoupling	Drag epoch	Recombination
x	Saha only	−7.16	−7.14	0.02	−7.13
	Saha + Peebles	−6.97	−6.95	0.02	−6.94
z	Saha only	1291.70	1260.11	−31.59	1249.29
	Saha + Peebles	1064.44	1037.76	−26.68	1033.21
t [kyr]	Saha only	279.19	291.19	11.99	295.48
	Saha + Peebles	387.17	404.02	16.85	407.01
η [Mpc]	Saha only	246.80	251.49	4.69	253.14
	Saha + Peebles	285.49	290.92	5.43	291.87
s [Mpc]	Saha only	128.90	131.09	2.19	131.85
	Saha + Peebles	146.66	149.10	2.44	149.53

cosmology, Planck reports statistically inferred values obtained by fitting a cosmological model to observational data. Differences in how reionization is handled (e.g., the choice of $z_{\text{reion}} = 8$ in my calculations vs. Planck's $z_{\text{reion}} = 7.64$) could also slightly shift estimated parameters.

Using the value for the particle horizon at photon decoupling presented in table 3.1 (Saha + Peebles approach) and the present-day particle horizon from table 2.1 (numerical value), the comoving distance to the last scattering surface is found to be $\chi_s \approx 13904.51$ Mpc. With my computed sound horizon at decoupling of $r_s \approx 146.66$ Mpc, this gives an angular acoustic scale of $100\theta_s \approx 1.0548$. This is slightly larger than the Planck result of $100\theta_s = 1.0411 \pm 0.0003$, falling outside their reported uncertainty. However, it should be noted that I have not been able to estimate the uncertainty of my estimate, and that the Planck value could fall within this range. Potential sources of this uncertainty include the finite resolution of the numerical integration, the choice of interpolation method for the visibility function, and approximations made in the recombination model.

TODO: maybe change/remove last part

3.3.5. Baryon temperature evolution

Figure 3.5 illustrates the evolution of the baryon temperature $T_b(x)$ (black line) compared to the photon (CMB) temperature $T_{\text{CMB}}(x)$ (grey line). Before recombination the baryon temperature closely follows the photon temperature due to strong Thomson scattering between electrons and CMB photons, which ensures thermal equilibrium. In this regime, both temperatures scale as $T \propto a^{-1}$, as expected for a relativistic plasma. However, baryons begin to cool independently some time after recombination, around $x \approx -6$. At this point, the baryon temperature transition from the radiation-like scaling to an adiabatic evolution, where $T_b \propto a^{-2}$, since the baryons no longer receive energy from photons and instead evolve as a non-relativistic gas in an expanding universe. This is directly linked to the drop in optical depth observed in figure 3.2. The delay between decoupling and the point where the two diverge explains why τ_b declines more gradually than τ, extending the impact of photon pressure beyond the formal decoupling time.

I found the baryon temperature to be $T_{b0} \approx 21$ mK, which is only about $\sim 7 - 8\%$ of the measured CMB temperature today. This result is consistent with theoretical expectations, given

the a^{-2} scaling of T_b after $x \approx 6$ compared to the a^{-1} scaling of T_{CMB}. However, unlike the CMB temperature, which follows a nearly perfect blackbody distribution with only small-scale anisotropies encoding information about early-universe physics, the baryon temperature is not a meaningful global quantity today. This is because matter has strongly clustered since decoupling, leading to highly non-linear structure formation. Most of the baryonic content is no longer in a diffuse, cold state, but concentrated into dense regions such as stars, galaxies, and the hot intergalactic medium. There are very few regions of truly diffuse baryonic gas with temperatures as low as the mean value presented here, though such cold gas remains an active area of research in extragalactic astronomy (see e.g., Tumlinson et al. (2017) and Nelson et al. (2020) about the cold circumgalactic medium).

The temperature deviation between photons and baryons introduces a minor correction to the photon-baryon sound speed, which in principle affects the evolution of acoustic oscillations. However, since recombination is complete before T_b and T_{CMB} significantly diverge, this effect is minimal. For precision calculations of the CMB power spectrum, including the evolution of T_b can slightly refine the modeling of BAO, but its impact on large-scale anisotropies will likely remains small, as mentioned in section 3.1.8.

4. Milestone III: Perturbations

Having established the background evolution of the universe and the recombination history in the previous milestones, I now turn to the evolution of cosmological perturbations, which describe how small fluctuations in density and temperature grew from the early Universe into the large-scale structures we observe today. This step is essential for understanding the formation of CMB anisotropies, as well as the distribution of galaxies and clusters in the late Universe.

In this milestone, I numerically solve the Einstein-Boltzmann equations in linear perturbation theory to track the evolution of cosmological perturbations in photons, neutrinos, baryons, and cold dark matter. These are computed across different Fourier modes to obtain time-dependent solutions for key quantities such as density and velocity perturbations, temperature anisotropies, and gravitational potentials. To manage numerical instabilities at early times, I implement the tight-coupling approximation. The resulting solutions form the basis for com-
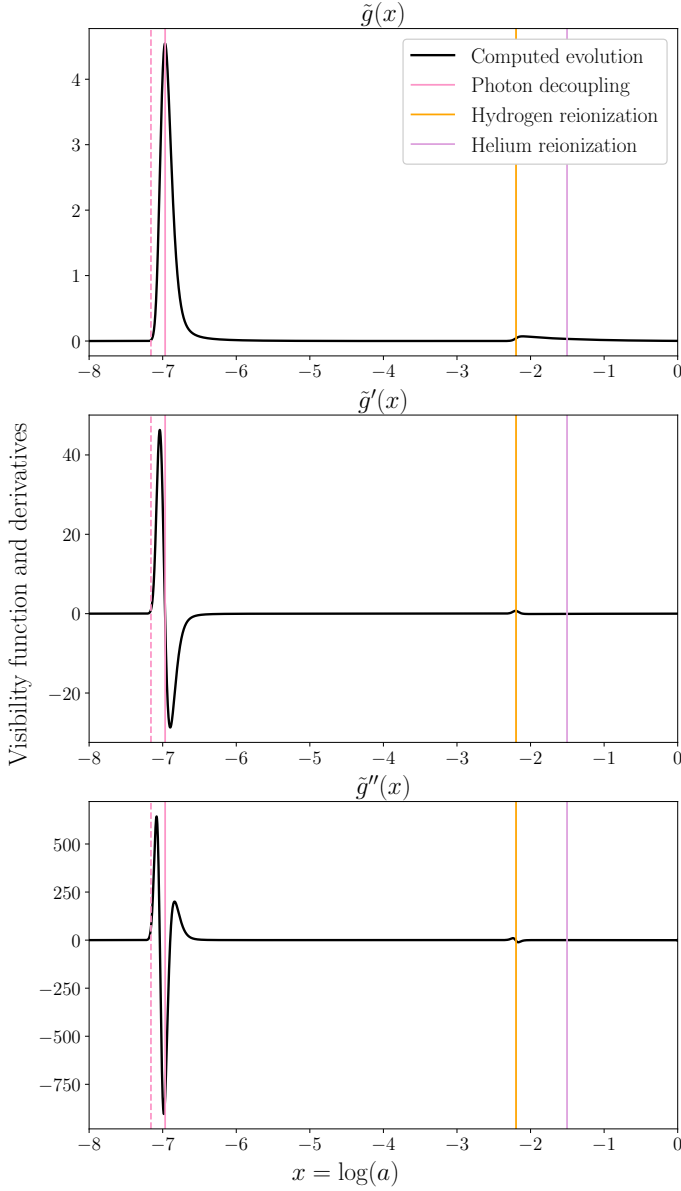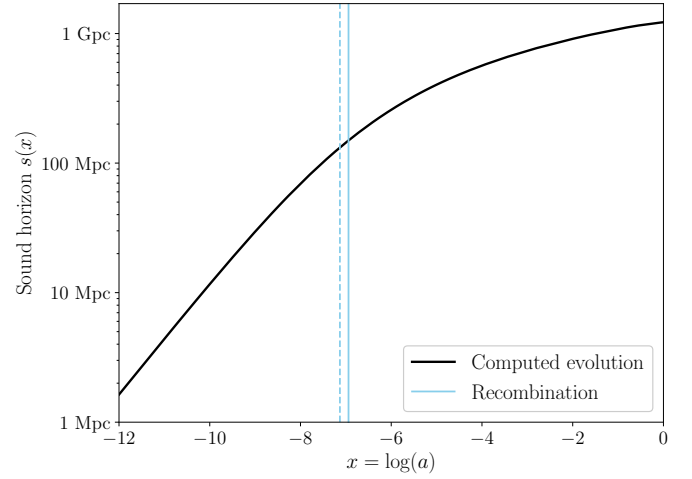
Fig. 3.3. The visibility function $\tilde{g}(x)$ (top), its first derivative $\tilde{g}'(x)$ (middle), and its second derivative $\tilde{g}''(x)$ (bottom). The sharp peak in $\tilde{g}$ defines the last scattering surface, while the first derivative's zero-crossing confirms the rapid transition.

Fig. 3.4. The evolution of the sound horizon $s(x)$ as a function of $x = \log(a)$. The rapid early growth reflects the high sound speed in the tightly coupled photon-baryon plasma, while the flattening at recombination marks the transition to the matter era.
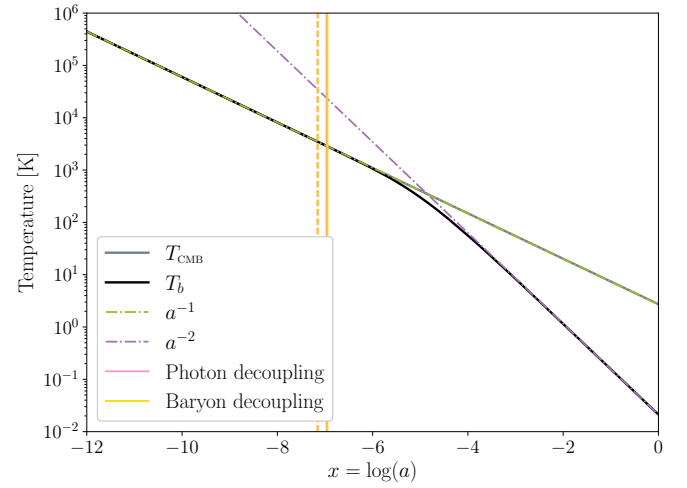
Fig. 3.5. The evolution of the baryon temperature $T_b(x)$ (black) compared to the photon temperature $T_{\mathrm{CMB}}(x)$ (grey). The two temperatures track each other closely before recombination due to strong Thomson scattering. Some time after decoupling, baryons start to cool adiabatically as $T_b \propto a^{-2}$ (purple dashed line), while photons continue to cool as $T_{\mathrm{CMB}} \propto a^{-1}$ (green dashed line).

puting the CMB power spectrum in the next milestone, enabling direct comparison between theory and observation.

4.1. Theoretical framework

4.1.1. Metric perturbations

The perturbed Einstein equations for scalars, vectors, and tensors decouple at linear order, allowing us to study them separately. In this work, I primarily focus on scalar perturbations, which correspond to density fluctuations and are responsible for structure formation. Vector perturbations (vorticity) are not generated by inflation and decay rapidly due to cosmic expansion, hence they are irrelevant when computing the CMB. Furthermore, tensor perturbations (gravitational waves) are a key prediction of inflation and is therefore a topic I revisit in the next milestone.

To simplify the perturbation equations, I work in the Newtonian gauge, where the metric is diagonal:

$$ds^2 = -(1 + 2\Psi)\,dt^2 + a^2(1 + 2\Phi)\,\delta_{ij}\,dx^i dx^j. \tag{4.1}$$

Here, Ψ and Φ are the gravitational potentials, which describe scalar perturbations to the metric and play analogous roles to the Newtonian potential in classical gravity. This is another perk of working in the Newtonian gauge, as it allows for more intuitive physical interpretation while keeping the full relativistic structure of general relativity. More specifically, Ψ represents the perturbation to the time-time component of the metric and acts as the gravitational potential experienced by non-relativistic particles, while Φ appears in the spatial metric perturbations and affects the expansion of space.

The perturbation equations take the form of coupled partial differential equations in real space, which are not trivial to solve.

To simplify the problem, we transform them into Fourier space, where they become a system of ordinary differential equations for each wave mode. In Fourier space, spatial derivatives transform as:

$$\nabla u(x) \rightarrow i\boldsymbol{k}\tilde{u}(k), \tag{4.2}$$

where $\boldsymbol{k}$ is the comoving wave vector of the perturbation. This Fourier decomposition allows us to track the evolution of perturbations across different scales and study their behavior from superhorizon to subhorizon regimes.

4.1.2. Photons

The evolution of CMB anisotropies is governed by perturbations in the photon distribution function. Since photons are massless, they follow null geodesics in a perturbed metric. For a photon with four-momentum P^μ and energy $E = p$, expanding the Christoffel symbols in the geodesic equation leads to:

$$\frac{dP^0}{d\lambda} + \Gamma^0_{\mu\nu}P^\mu P^\nu = 0 \tag{4.3}$$

$$\Rightarrow \frac{dp}{dt} = \frac{1}{P_0}\frac{dp}{d\lambda} \simeq -p\left[H + \frac{\partial\Phi}{\partial t} + \frac{\partial\Psi}{\partial x^i}\frac{\hat{p}^i}{a}\right]. \tag{4.4}$$

show this? This equation describes how the photon energy changes due to both cosmic expansion (the Hubble term H) and metric perturbations. Integrating from recombination to today gives the perturbation to the photon energy in terms of its initial value:

$$\left(\frac{\delta p}{p}\right)_0 = \left(\frac{\delta p}{p}\right)_{\text{rec}} + (\Psi_{\text{rec}} - \Psi_0) + \int_{t_{\text{rec}}}^{t_0}\left[\frac{\partial\Psi}{\partial t} - \frac{\partial\Phi}{\partial t}\right]dt. \tag{4.5}$$

Eq. (4.5) encodes two key effects that shape CMB anisotropies. The first of these is the Sachs-Wolfe effect: the gravitational redshift of photons due to metric perturbations at the last scattering surface, corresponding to the term $(\Psi_{\text{rec}} - \Psi_0)$. More specifically, this represents the change in the gravitational potential from recombination to today. Furthermore, the last term represents the time variation of the metric perturbations $(\partial_t\Psi - \partial_t\Phi)$, which affects photons' energies as they travel through evolving potential wells. This is called the integrated Sachs-Wolfe (ISW) effect, and is most important in the late Universe when dark energy becomes significant.

To describe perturbations in the CMB systematically, we introduce the photon temperature perturbation, defined as:

$$T = \overline{T}(1 + \Theta), \tag{4.6}$$

where $\Theta = \delta T/\overline{T}$ represents small deviations from the mean photon temperature. This perturbation generally depends on time, space, the magnitude, and direction of the photon momentum. However, since Thomson scattering only affects the direction of the photon momentum to first order, we can express the perturbation as $\Theta(t, \boldsymbol{x}, \hat{p})$, eliminating explicit dependence on p. Furthermore, expanding the distribution function for photons in the limit $\Theta \ll 1$ gives:

$$f = \frac{1}{e^{p/\overline{T}(1-\Theta)} - 1} \simeq \overline{f} + \Theta p\frac{\partial\overline{p}}{\partial p}\Theta, \tag{4.7}$$

where

$$\overline{f} = \frac{1}{e^{p/\overline{T}} - 1}. \tag{4.8}$$

Since the chemical potential $\mu = 0$ for photons, this follows directly from the Bose-Einstein distribution (eq. (3.1)). Subtracting the background evolution from the full Boltzmann equation (3.3) leads to the first-order perturbed Boltzmann equation for photons:

$$\frac{df}{d\lambda} = -p^2\frac{\partial\overline{f}}{\partial p}\left[\frac{\partial\Theta}{\partial t} + \frac{\partial\Theta}{\partial x^i}\frac{\hat{p}^i}{a} + \left(\frac{\partial\Phi}{\partial t} + \frac{\partial\Psi}{\partial x^i}\frac{\hat{p}^i}{a}\right)\right] = C[f]. \tag{4.9}$$

show this more explicitly?

If we ignore polarization and the angular dependence of the Thomson scattering cross section, the collision to first order in perturbation theory simplifies to

$$C[f] = -p^2\frac{\partial\overline{f}}{\partial p}n_e\sigma_{\text{T}}\left(\Theta_0 - \Theta + \hat{p}\cdot\boldsymbol{v}_b\right). \tag{4.10}$$

Here, $\boldsymbol{v}_b$ is the baryon velocity, which describes how fast electrons (and protons) are moving, and

$$\Theta_0 = \frac{1}{4\pi}\int\Theta\, d\Omega_{\hat{p}} = \frac{1}{2}\int_{-1}^1\Theta\, d\mu, \tag{4.11}$$

is the monopole moment of the photon distribution, which describes the local temperature averaged over all directions. The integration variable μ is simply the cosine of the angle between the wavevector $\boldsymbol{k}$ and the photon direction:

$$\mu = \hat{p}\cdot\frac{\boldsymbol{k}}{k}. \tag{4.12}$$

Thus, inserting this into eq (4.9) we arrive at the perturbed Boltzmann equation for photons:

$$\frac{\partial\Theta}{\partial t} + \frac{\partial\Theta}{\partial x^i}\frac{\hat{p}^i}{a} + \left(\frac{\partial\Phi}{\partial t} + \frac{\partial\Psi}{\partial x^i}\frac{\hat{p}^i}{a}\right) = n_e\sigma_{\text{T}}\left(\Theta_0 - \Theta + \hat{p}\cdot\boldsymbol{v}_b\right). \tag{4.13}$$

This equation tells us that when Thomson scattering is efficient, photons from different directions have the same temperature, enforcing $\Theta \approx \Theta_0$ locally.

Since CMB perturbations are naturally described in Fourier space, it is convenient to make use of $\boldsymbol{k}$ and μ. The baryon velocity is curl-free, so in Fourier space it simplifies to

$$\boldsymbol{v}_b = iv_b\frac{\boldsymbol{k}}{k}. \tag{4.14}$$

With this, the Boltzmann equation transforms into

$$\frac{\partial\Theta}{\partial t} + \frac{ik\mu}{a}\Theta + \left(\frac{\partial\Phi}{\partial t} + \frac{ik\mu}{a}\Psi\right) = n_e\sigma_T\left(\Theta_0 - \Theta + i\mu v_b - \frac{3\mu^2 - 1}{4}\Pi\right), \tag{4.15}$$

where the additional term

$$\Pi = \Theta_2 + \Theta_0^P + \Theta_2^P, \tag{4.16}$$

accounts for the angular dependence of Tomson scattering through the temperature quadrupole Θ_2, and CMB polarization through the polarization monopole Θ_0^P and quadrupole Θ_2^P.

4.1.3. Multipole expansions

As mentioned in the previous section, the equation governing the evolution of the photon temperature perturbation depends explicitly on the angular direction of the photon momentum. To obtain a more manageable system of equations, it is convenient to expand the angular dependence of the perturbation $\Theta(t, k, \mu)$ in terms of Legendre polynomials, leading to a hierarchy of equations known as the Boltzmann hierarchy. This expansion is particularly useful since the CMB anisotropies are naturally expressed in terms of spherical harmonics, which are closely related to Legendre polynomials. Thus, we write:

$$\Theta(t, k, \mu) = \sum_{\ell=0}^{\infty} \frac{2\ell + 1}{i^\ell} \Theta_\ell(t, k) P_\ell(\mu), \qquad (4.17)$$

where $P_\ell(\mu)$ are the Legendre polynomials, and Θ_ℓ are the multipole moments of the photon distribution function, defined as:

$$\Theta_\ell(t, k) = \frac{i^\ell}{2} \int_{-1}^{1} \Theta(t, k, \mu) P_\ell(\mu) d\mu. \qquad (4.18)$$

The first few moments in the multipole expansion have clear physical interpretations. As we have already seen in eq. (4.10), the $\ell = 0$ term corresponds to the monopole moment, which is directly related to the density contrast of radiation via $\delta_\gamma = 4\Theta_0$. Furthermore, the $\ell = 1$ term describes the dipole moment, which tells us about the velocity of the photon perturbations via the relation $v_\gamma = -3\Theta_1$. Lastly, $\ell = 2$ corresponds to the quadrupole moment of the photon distribution and is closely associated with the anisotropic stress, which I will get back to. Higher-order multipoles describe increasingly finer angular variations in the photon distribution, though they are less intuitive to interpret physically.

To derive the evolution equations for the multipoles, we take moments of the Boltzmann equation for photons. This requires the orthogonality relation for Legendre polynomials,

$$\mu P_\ell = \frac{\ell + 1}{2\ell + 1} P_{\ell+1} + \frac{\ell}{2\ell + 1} P_{\ell-1}. \qquad (4.19)$$

Multiplying eq. (4.15) by $(i^\ell/2)P_\ell$ and integrating over μ allows us to obtain a coupled hierarchy of equations. For $\ell = 0, 1, 2, \ldots$, this results in:

$$\Theta_0' = -\frac{ck}{\mathcal{H}}\Theta_1 - \Phi', \qquad (4.20)$$

$$\Theta_1' = \frac{ck}{3\mathcal{H}}\Theta_0 - \frac{2ck}{3\mathcal{H}}\Theta_2 + \frac{ck}{3\mathcal{H}}\Psi + \tau'\left[\Theta_1 + \frac{1}{3}v_b\right], \qquad (4.21)$$

$$\Theta_\ell' = \frac{ck}{(2\ell + 1)\mathcal{H}}\left[\ell\Theta_{\ell-1} - (\ell + 1)\Theta_{\ell+1}\right]$$
$$+ \tau'\left[\Theta_\ell - \frac{1}{10}\Pi\delta_{\ell,2}\right], \qquad \ell \geq 2. \qquad (4.22)$$

Here, derivatives are taken with respect to x, and the optical depth derivative τ' appears as it was defined in eq. (3.39).

Eq. (4.20) corresponds to the perturbed continuity equation for photons, which ensures conservation of particle number. Furthermore, eq. (4.21) describes the evolution of the photon dipole and is equivalent to the Euler equation, accounting for the anisotropic stress through the quadrupole term, as well as the momentum transfer between photons and baryons via the last term. This ensures that the baryon velocity remains equal to

the photon velocity in the tight-coupling regime, which I come back to in section 4.1.10.

Since the Boltzmann hierarchy contains an infinite number of coupled equations, solving the full system numerically is impossible. Fortunately, at sufficiently high multipoles, the moments decrease in amplitude, allowing for an approximation. However, a naive truncation, such as setting all moments beyond some $\ell_{\max}$ to zero, would introduce errors that propagate to lower multipoles. Instead, the hierarchy is truncated by modifying the equation for the highest included multipole:

$$\Theta_{\ell_{\max}}' = \frac{ck}{\mathcal{H}}\Theta_{\ell_{\max}-1} - c\frac{\ell_{\max} + 1}{\mathcal{H}\eta(x)}\Theta_{\ell_{\max}} + \tau'\Theta_{\ell_{\max}}. \qquad (4.23)$$

This ensures that the high-order multipoles decay smoothly, preventing numerical artifacts. In the next milestone I employ an extremely valuable method known as line-of-sight integration, which lets us set $\ell_{\max} \sim 6 - 10$ and still obtain moderate to high accuracy.

4.1.4. Polarization

In addition to the temperature anisotropies of the CMB, polarization also plays a significant role in constraining cosmological parameters. The CMB becomes polarized due to Thomson scattering, which selectively filters the radiation field and generates linear polarization when there is a local quadrupole anisotropy in the photon distribution.

The equations governing the polarization multipoles Θ_ℓ^P are similar to those for the temperature perturbations, but differ in their source terms and hierarchical coupling. It can be shown that the full set of equations for takes the following form:

$$\Theta_0'^P = -\frac{ck}{\mathcal{H}}\Theta_1^P + \tau'\left[\Theta_0^P - \frac{1}{2}\Pi\right], \qquad (4.24)$$

$$\Theta_\ell'^P = \frac{ck}{(2\ell + 1)\mathcal{H}}\left[\ell\Theta_{\ell-1}^P - (\ell + 1)\Theta_{\ell+1}^P\right]$$
$$+ \tau'\left[\Theta_\ell^P - \frac{1}{10}\Pi\delta_{\ell,2}\right], \qquad 1 \leq \ell < \ell_{\max}, \qquad (4.25)$$

$$\Theta_{\ell_{\max,P}}'^P = \frac{ck}{\mathcal{H}}\Theta_{\ell_{\max,P}-1}^P - c\frac{\ell + 1}{\mathcal{H}\eta(x)}\Theta_{\ell_{\max,P}}^P + \tau'\Theta_{\ell_{\max,P}}^P. \qquad (4.26)$$

Tight-coupling allows us to truncate this hierarchy in the same way as for photons, hence we may set $\ell_{\max,P} = \ell_{\max}$.

<mark>should I refer to Callin when not deriving eq. myself?</mark>

4.1.5. Neutrinos

Being nearly massless and only weakly interacting, neutrinos evolve differently from photons in the early Universe. While photons remain tightly coupled to baryons through Thomson scattering until recombination, neutrinos decoupled approximately one second after the Big Bang and have free-streamed almost unimpeded from then on. Their behavior is well-described by a perturbation to the neutrino temperature, similar to that of photons. Defining the fractional temperature perturbation as

$$\mathcal{N} = \frac{\delta T_\nu}{\overline{T}_\nu} \quad \Leftrightarrow \quad T_\nu = \overline{T}_\nu(1 + \mathcal{N}), \qquad (4.27)$$

we find that the evolution of neutrino perturbations is exactly the same as that of photons in the absence of a collision term:

$$\frac{\partial \mathcal{N}}{\partial t} + \frac{ik\mu}{a}\mathcal{N} + \left(\frac{\partial \Phi}{\partial t} + \frac{ik\mu}{a}\Psi\right) = 0. \qquad (4.28)$$

This equation shows that neutrino perturbations are only influenced by gravitational redshifting due to potential wells and cosmic expansion.

Since neutrinos are free-streaming, their distribution must be expanded into multipoles to describe their angular structure. Similar to the photon case, we may decompose the perturbation into Legendre multipoles:

$$\mathcal{N}_0' = -\frac{ck}{\mathcal{H}}\mathcal{N}_1 - \Phi', \tag{4.29}$$

$$\mathcal{N}_1' = \frac{ck}{3\mathcal{H}}\mathcal{N}_0 - \frac{2ck}{3\mathcal{H}}\mathcal{N}_2 + \frac{ck}{3\mathcal{H}}\Psi, \tag{4.30}$$

$$\mathcal{N}_\ell' = \frac{ck}{(2\ell+1)\mathcal{H}}\big[\ell\mathcal{N}_{\ell-1} - (\ell+1)\mathcal{N}_{\ell+1}\big], \qquad \ell \geq 2. \tag{4.31}$$

Truncating this Boltzmann hierarchy at some maximum value $\ell_{\max,\nu}$ gives us then

$$\mathcal{N}_{\ell_{\max,\nu}}' = \frac{ck}{\mathcal{H}}\mathcal{N}_{\ell_{\max,\nu}-1} - c\frac{\ell_{\max,\nu}+1}{\mathcal{H}\eta(x)}\mathcal{N}_{\ell_{\max,\nu}}. \tag{4.32}$$

Unlike photons, neutrinos freely propagate without being driven toward a monopole component through scattering processes. As a result, their anisotropies persist and contribute to the formation of cosmic structures. Additionally, their relativistic free-streaming contributes to the radiation density, altering the expansion rate and damping small-scale fluctuations. This free-streaming also induces a phase shift in the CMB power spectrum, providing a signature of their presence. Accurately modeling these effects requires truncating the Boltzmann hierarchy for neutrinos at $\ell_{\max,\nu} \approx 10 - 12$, capturing their impact more comprehensively than the photon case, where tight coupling allows for truncation at lower ℓ.

4.1.6. Cold dark matter

Cold dark matter (CDM) plays a crucial role in the formation of cosmic structure. Unlike photons and neutrinos, CDM particles are non-relativistic and interact only through gravity, meaning they do not experience pressure support or free-streaming effects. This leads to a different evolution for CDM perturbations, which gravitationally attract baryons and seed the formation of galaxies and large-scale structure.

The evolution of CDM density and velocity perturbations can be derived from the Boltzmann equation as well. Because dark matter does not participate in scattering interactions, its collision term vanishes, leaving us with the following equation governing its phase-space distribution function:

$$\frac{\partial f}{\partial t} + \frac{\partial f}{\partial x^i}\frac{\hat{p}^i}{a}\frac{p}{E} - \frac{\partial f}{\partial E}\left[H\frac{p^2}{E} + \frac{\partial \Phi}{\partial t}\frac{p^2}{E} + \frac{\partial \Psi}{\partial x^i}\frac{p\hat{p}^i}{a}\right] = 0. \tag{4.33}$$

Since CDM is non-relativistic ($E \approx m$), its evolution is primarily described by the first two moments of the Boltzmann equation—the density contrast and the velocity divergence—rather than a full hierarchy of multipole moments as needed for photons and neutrinos. By integrating over the momentum space, we obtain the continuity equation, which describes the conservation of CDM number density in an expanding Universe:

$$\frac{\partial n}{\partial t} + \frac{1}{a}\frac{\partial}{\partial x^i}\left(nv^i\right) + 3n\left(H + \frac{\partial \Phi}{\partial t}\right) = 0. \tag{4.34}$$

This equation closely resembles the fluid continuity equation, with additional terms accounting for the expansion of the Universe and the effect of gravitational potentials.

write as an overdensity equation instead?

To describe the evolution of CDM velocity perturbations, we take the first moment of the Boltzmann equation, yielding the Euler equation:

$$\frac{\partial v^i}{\partial t} + Hv^i = -\frac{1}{a}\frac{\partial \Psi}{\partial x^i}. \tag{4.35}$$

Since CDM is pressureless, it does not develop internal sound waves, unlike baryons, which are influenced by photon pressure. Instead, dark matter perturbations grow primarily due to gravitational instability, following the potential wells formed by initial fluctuations in the early Universe.

In Fourier space, the evolution equations for the CDM overdensity δ_{CDM} and velocity divergence v_{CDM} take the simpler forms:

$$\delta_{\mathrm{CDM}}' = \frac{ck}{\mathcal{H}}v_{\mathrm{CDM}} - 3\Phi', \tag{4.36}$$

$$v_{\mathrm{CDM}}' = -v_{\mathrm{CDM}} - \frac{ck}{\mathcal{H}}\Psi. \tag{4.37}$$

These equations highlight how CDM perturbations respond to metric fluctuations. The density contrast evolves due to velocity divergence and changes in the gravitational potential, while the velocity perturbation is sourced by gradients in the metric perturbation Ψ, analogous to how the Euler equation describes the motion of a perfect fluid affected by gravity.

4.1.7. Baryons

Having established the equations governing photons, neutrinos, and cold dark matter, the next step is to consider ordinary baryonic matter (electrons and protons). Since the number of baryons is conserved, the continuity equation follows directly from the dark matter case, as neither Coulomb nor Compton interactions affect baryon number conservation. Thus, the baryon number density satisfies

$$\frac{\partial n_b}{\partial t} + \frac{1}{a}\frac{\partial}{\partial x^i}\left(n_b v_b^i\right) + 3n_b\left(H + \frac{\partial \Phi}{\partial t}\right) = 0. \tag{4.38}$$

The key distinction from dark matter lies in the Euler equation, which governs momentum conservation. Unlike dark matter, baryons experience interactions that transfer momentum, particularly through the Thomson scattering of photons off electrons. The last term in the Euler equation for photons, derived earlier from the multipole expansion (see eq. (4.21), and recall that $v_\gamma = -3\Theta_1$), accounts for this momentum transfer. Since momentum must be conserved between the baryons and photons, the baryon Euler equation must include a corresponding term weighted by the relative energy densities:

$$\frac{\partial v_b^i}{\partial t} + Hv_b^i = -\frac{1}{a}\frac{\partial \Psi}{\partial x^i} - \tau' R(v_\gamma^i - v_b^i), \tag{4.39}$$

where R is the ratio defined in eq. (3.41).

As with other components, it is useful to take the Fourier transform to express the baryon evolution equations in terms of the density contrast δ_b and velocity divergence v_b. These take the

standard form:

$$\delta_b' = \frac{ck}{\mathcal{H}}v_b - 3\Phi', \tag{4.40}$$

$$v_b' = -v_b - \frac{ck}{\mathcal{H}}\Psi + \tau' R(3\Theta_1 + v_b). \tag{4.41}$$

The presence of τ' indicates that prior to recombination, photons exert a significant drag force on baryons, preventing them from freely collapsing under gravity. Once recombination occurs and free electrons become scarce, τ' drops, allowing baryons to decouple from photons and fall into dark matter potential wells, ultimately leading to structure formation.

4.1.8. Gravitational potentials

We have now established the perturbation equations for the different species in the Universe, and we finally arrive at the equations governing the metric potentials, Ψ and Φ. The first of these equations follows from the perturbed Einstein equations and describes how the time evolution of the metric perturbations is linked to the density perturbations in different components:

$$\Phi' = \Psi - \frac{c^2 k^2}{3\mathcal{H}^2}\Phi + \frac{H_0^2}{2\mathcal{H}^2}\big(\Omega_{\mathrm{CDM0}}\delta_{\mathrm{CDM}} + \Omega_{b0}\delta_b\big)e^{-x}$$
$$+ \frac{2H_0^2}{\mathcal{H}^2}\big(\Omega_{\gamma 0}\Theta_0 + \Omega_{\nu 0}\mathcal{N}_0\big)e^{-2x}. \tag{4.42}$$

`derive this?` This equation shows that the gravitational potential Φ evolves due to the curvature of space (Ψ term), gradients in the potential itself (the k^2 term), and contributions from cold dark matter, baryons, photons, and neutrinos.

The second equation we need provides a constraint relating Ψ and Φ. In the absence of anisotropic stress, general relativity dictates that $\Phi = -\Psi$. However, the presence of relativistic species such as photons and neutrinos generates an anisotropic stress contribution, which modifies this relation:

$$\Psi = -\Phi - \frac{12H_0^2}{c^2 k^2}\big(\Omega_{\gamma 0}\Theta_2 + \Omega_{\nu 0}\mathcal{N}_2\big)e^{-2x}. \tag{4.43}$$

A key takeaway from these equations is that while Φ is dynamical and evolves due to matter and radiation perturbations, Ψ follows directly from Φ once the anisotropic stress contributions are known. This allows us to solve for the evolution of metric perturbations given the behavior of the matter and radiation components.

4.1.9. Inflation and initial conditions

To numerically evolve perturbations in the early Universe, we must first determine the initial conditions for all variables involved. This requires an understanding of their origin, which inflation provides a compelling explanation for. During this phase of accelerated expansion, quantum fluctuations in the inflaton field were stretched to cosmological scales, transitioning into classical perturbations that seeded the large-scale structure of the Universe.

A central prediction of inflation is the emergence of a nearly scale-invariant Gaussian random field of curvature perturbations, characterized by

$$\langle \mathcal{R}(\boldsymbol{k})\mathcal{R}^*(\boldsymbol{k}')\rangle = (2\pi)^3 \delta(\boldsymbol{k} - \boldsymbol{k}')P_{\mathrm{primordial}}(k). \tag{4.44}$$

The function $P_{\mathrm{primordial}}(k)$ is known as the primordial power spectrum, and is properly introduced in section 5.1.3 of the next milestone. Outside the horizon (i.e., for modes where $ck \ll \mathcal{H}$), the curvature perturbation field $\mathcal{R}$ remains approximately constant:

$$\frac{d\mathcal{R}}{dt} \approx 0. \tag{4.45}$$

This conservation law allows us to use $\mathcal{R}$ as a bridge between inflationary predictions and initial conditions at later times.

In the Newtonian gauge, the curvature perturbation field is defined as

$$\mathcal{R} = \Phi + \frac{\mathcal{H}^2\,(\Phi' - \Psi)}{4\pi G(\bar{\rho} + \bar{P})}e^{-2x}. \tag{4.46}$$

For superhorizon modes in the radiation era, where metric potentials vary slowly, we have $\Phi' \approx 0$ and $\Psi' \approx 0$, and thus $\mathcal{R} \approx \Phi - \Psi/2$. Assuming $\mathcal{R} = 1$ thus sets the normalization for all other perturbation variables. The relation between the two potentials then becomes

$$\Phi + \Psi \simeq -\frac{2f_\nu}{5}\Psi, \tag{4.47}$$

where

$$f_\nu = \frac{\Omega_{\nu 0}}{\Omega_{\gamma 0} + \Omega_{\nu 0}}, \tag{4.48}$$

is the neutrino fraction. This yields the following initial conditions:

$$\Psi = \left(\frac{3}{2} + \frac{2f_\nu}{5}\right)^{-1}, \tag{4.49}$$

$$\Phi = -\left(1 + \frac{2f_\nu}{5}\right)\Psi. \tag{4.50}$$

`derive these things more thoroughly?`
It can further be shown that for cold dark matter and baryons, the initial conditions become:

$$\delta_{\mathrm{CDM}} = \delta_b = -\frac{3}{2}\Psi, \tag{4.51}$$

$$v_{\mathrm{CDM}} = v_b = -\frac{ck}{2\mathcal{H}}\Psi, \tag{4.52}$$

while for photons, we set:

$$\Theta_0 = -\frac{1}{2}\Psi, \tag{4.53}$$

$$\Theta_1 = \frac{ck}{6\mathcal{H}}\Psi, \tag{4.54}$$

$$\Theta_2 = \begin{cases} -\dfrac{8ck}{15\mathcal{H}\tau'}\Theta_1, & \text{(with polarization)} \\[2mm] -\dfrac{20ck}{45\mathcal{H}\tau'}\Theta_1, & \text{(without polarization)} \end{cases} \tag{4.55}$$

$$\Theta_\ell = -\frac{\ell}{2\ell + 1}\frac{ck}{\mathcal{H}\tau'}\Theta_{\ell-1}, \qquad \ell \geq 3. \tag{4.56}$$

For photon polarization we have:

$$\Theta_0^P = \frac{5}{4}\Theta_2, \tag{4.57}$$

$$\Theta_1^P = -\frac{ck}{4\mathcal{H}\tau'}\Theta_2, \tag{4.58}$$

$$\Theta_2^P = \frac{1}{4}\Theta_2, \tag{4.59}$$

$$\Theta_\ell^P = -\frac{\ell}{2\ell + 1}\frac{ck}{\mathcal{H}\tau'}\Theta_{\ell-1}^P, \qquad \ell \geq 3. \tag{4.60}$$

Lastly, the neutrino perturbations follow a similar hierarchy:

$$\mathcal{N}_0 = -\frac{1}{2}\Psi, \tag{4.61}$$

$$\mathcal{N}_1 = \frac{ck}{6\mathcal{H}}\Psi, \tag{4.62}$$

$$\mathcal{N}_2 = -\frac{c^2k^2(\Phi + \Psi)}{12H_0^2\Omega_{\nu 0}}e^{2x}, \tag{4.63}$$

$$\mathcal{N}_\ell = \frac{ck}{(2\ell + 1)\mathcal{H}}\mathcal{N}_{\ell-1}, \qquad \ell \geq 3. \tag{4.64}$$

These initial conditions, derived under the assumption of adiabaticity, allow us to evolve the Boltzmann system forward in time from a well-defined starting point. If one excludes polarization the equations above simplify accordingly, since then Π is simply equal to Θ_2. Similarly, excluding neutrinos sets $f_\nu = 0$.

should the initial conditions be derived?

4.1.10. The tight-coupling regime

Unfortunately, solving the full Boltzmann hierarchy numerically across all times is not practical—particularly in the early Universe, when Thomson scattering is extremely efficient and the optical depth derivative τ' is very large. In this limit, the equations become stiff and unstable for direct numerical integration. To avoid this issue, we may adopt a simplified set of equations valid in the so-called tight-coupling regime, where photons and baryons are so strongly coupled that they behave as a single fluid. These are derived under the assumption that time derivatives of $(3\Theta_1 + v_b)$ are suppressed and can be approximated via a leading-order expansion in $1/\tau'$.

By defining the combination

$$q = -\kappa\Big[(1 - R)\tau' + (1 + R)\tau''\Big](3\Theta_1 + v_b)$$
$$- \kappa\frac{ck}{\mathcal{H}}\left[\Psi + \left(1 - \frac{\mathcal{H}'}{\mathcal{H}}\right)(\Theta_0 - 2\Theta_2) + \Theta_0'\right], \tag{4.65}$$

where the factor

$$\kappa = \left[(1 + R)\tau' + \frac{\mathcal{H}'}{\mathcal{H}} - 1\right]^{-1}, \tag{4.66}$$

we may write the baryon velocity evolution as

$$v_b' = \frac{1}{1 + R}\left[-v_b - \frac{ck}{\mathcal{H}}\Psi + R\left(q + \frac{ck}{\mathcal{H}}(-\Theta_0 + 2\Theta_2) - \frac{ck}{\mathcal{H}}\Psi\right)\right]. \tag{4.67}$$

The evolution of the photon dipole then becomes

$$\Theta_1' = \frac{1}{3}(q - v_b'). \tag{4.68}$$

Furthermore, the higher-order photon multipoles, as well as all of the polarization multipoles, are not dynamically evolved but instead algebraically determined from the dipole. More specifically, they can all be computed using the initial conditions in the normal regime (eqs. (4.55)-(4.60)). Furthermore, neutrinos are unaffected by baryon-photon interactions and therefore evolve the same way as usual.

should I add a sec. about analytical approx. for testing?

or is it enough to compare to your figures?

4.2. Implementation details

TODO: maybe mention k thing

4.2.1. Main program structure

The class `Perturbations`, implemented in the corresponding source and header files, contains methods for solving all perturbation quantities—both in the tight-coupling regime and in the regime where the full Boltzmann equations apply. The results are stored using cubic 2D splines for efficient lookup, and can be retrieved via dedicated get-methods that take x and k as arguments. For the photon, polarization, and neutrino multipoles, the multipole number ℓ is required as a third argument. Additionally, this class computes and splines the source functions needed for the line-of-sight integration in the next milestone (see section 5.1.2 for the relevant expressions).

The number of photon multipoles included when solving the system is controlled by the constructor argument `n_ell_Theta`. For the results presented in section 4.3, I have set this to 11, corresponding to $\ell_{\max} = 10$. Inclusion of polarization and neutrino multipoles is governed by the arguments `n_ell_Theta_P` and `n_ell_Nu`, respectively: if either is set to zero, the associated boolean flags `polarization` or `neutrinos` are set to `false`. I have used 11 multipoles for polarization and 13 for neutrinos to ensure adequate numerical accuracy. An additional boolean constructor argument `lensing` determines whether the source function for the CMB lensing potential (see section 5.1.6) is computed.

maybe not mention source funcs before next milestone?

As before, the code uses the GSL-based ODE solver, though the system now contains many more components. Since the equations must be solved independently for each value of k, the runtime can be substantial. To address this, I have parallelized the k-loops using OpenMP, and enabled this feature by adding the compiler flag `-fopenmp` to the `Makefile` provided by Winther. Moreover, the results are written to file for a chosen value of k using a single output-method, and visualized in `perturbations.py`.

4.2.2. Keeping track of indices

In the class constructor, I define integer indices `idx_var`, where `var` refers to one of the scalar quantities we solve for: Φ, δ_{CDM}, δ_b, v_{CDM}, and v_b. Their respective indices are set to 0, 1, 2, 3, and 4. These constants are used throughout the code to access variables when setting initial conditions, solving the system, and filling the 2D vector `y_array` with the full solutions.

For the photon, polarization, and neutrino multipoles, I define separate starting indices `idx_start_var` corresponding to the positions of their respective monopoles. For photons, this index is given by `idx_start_Theta = n_scalars`, where `n_scalars = 5`. The starting indices for polarization and neutrinos depend on whether these components are included, so they are defined as:

$$i_{\text{start},P} = i_{\text{start},\Theta} + n_{\ell,\Theta} - (1 - b_P),$$
$$i_{\text{start},\nu} = i_{\text{start},P} + n_{\ell,P} + (b_\nu - b_P).$$

Here, $i_{\text{start},P}$ and $n_{\ell,P}$ correspond to the starting index and total number of polarization multipoles, while b_P is the polarization bool. The same goes for photons (subscript Θ) and neutrinos (ν). For example, with 8 photon multipoles and we want to include neutrinos but not polarization, we get $i_{\text{start},P} = 5 + 8 - (1 - 0) = 12$

and $i_{\text{start},\nu} = 12 + 0 + (1 - 0) = 13$. This way, $\mathcal{N}_0$ correctly follows immediately after Θ_7.

When storing the ODE results, I declare `y_array` with `n_ell_tot + 2` components, where `n_ell_tot` includes the 5 scalars and the total number of included multipoles. This extra space is reserved for storing the metric perturbation $\Psi(x, k)$ and the polarization source $\Pi(x, k)$, which are not solved directly but instead computed afterwards using eqs. (4.43) and (4.16). These are appended at the end of `y_array`, with Π stored last.

4.2.3. Switching between regimes

As the Universe evolves and scattering between photons and electrons weakens, we eventually exit the tight-coupling regime. To determine when this transition occurs, it is necessary to define a set of conditions that must be met simultaneously:

1. $\left|\dfrac{d\tau}{dx}\right| > 10,$ \hfill (4.69)

2. $\left|\dfrac{d\tau}{dx}\right| > 10\dfrac{ck}{\mathcal{H}}$ \hfill (4.70)

3. We have not yet passed the onset of recombination, which we take to occur at $x = -8.3$ (corresponding to $z \approx 4000$).

For each mode k, we start at the initial time and search forward to find when tight-coupling ends. This occurs when:

$$\left|\frac{d\tau}{dx}\right| = 10 \cdot \min\left(1, \frac{ck}{\mathcal{H}}\right). \tag{4.71}$$

If the solution gives $x > -8.3$, I fix the end of tight coupling to $x = -8.3$ instead. In practice, this only affects the smallest scales ($k \gtrsim 0.15\,\text{Mpc}^{-1}$), where tight coupling breaks earlier due to faster photon decoupling. At this point, I switch to solving the full Boltzmann hierarchy to accurately track the evolution of anisotropies around recombination.

should I move this to theory?

I use the endpoints of the tight-coupling ODE solutions as initial conditions for the full system, with the exception of the multipoles $\Theta_{\ell \geq 2}$ and Θ_ℓ^P. Since these only start evolving dynamically after tight-coupling ends, their derivatives are set to zero in this regime, and they are instead determined from the initial conditions defined in section 4.1.9. As a result, their values are small but non-zero at early times—particularly for large k. I therefore compute these multipoles separately using the inflationary initial conditions after retrieving the solutions for the dynamical quantities, and fill `y_array` accordingly, since their values from the ODE solver will otherwise be zero.

should I explain that I find a tc-index?

4.2.4. Integration limits and points

When integrating the perturbation equations, I used the range $x_{\min} = -18.0$ to $x_{\max} = 0.0$, with $1,000$ sampling points for computational efficiency. This resolution was found to give results nearly indistinguishable from those obtained using $10,000$ points, making it a reasonable trade-off between accuracy and runtime. Although large values of k take significantly longer to solve than small ones, I opted to compute the solutions for 200 logarithmically spaced k-modes between $k_{\min} = 5.0 \times 10^{-5}\,\text{Mpc}^{-1}$ and $k_{\max} = 1.0\,\text{Mpc}^{-1}$ to capture the full range of scale-dependent behaviors.

For plotting purposes, I focused on a representative subset of modes: $k \in [0.001, 0.01, 0.1, 1.0]\,\text{Mpc}^{-1}$, as including more values would make the figures cluttered and harder to interpret. Modes with $k < 0.001\,\text{Mpc}^{-1}$ correspond to extremely large scales that do not enter the horizon until very late times and thus show limited evolution within the range of interest. For the output, I used the same x-range as in the integration and sampled $18,001$ points with spacing $\Delta x = 0.001$ to ensure smooth visualizations.

4.2.5. Testing the code

Many of the quantities computed in this milestone are intricately linked through tight-coupling relations and Boltzmann hierarchies, meaning that even minor implementation errors can propagate and lead to incorrect results. Unfortunately, several of these quantities are also challenging to interpret physically. While there are many possible ways to test the code, I found it most instructive to compare against the reference plots provided by Winther et al. (Accessed: June 2025) okay to cite this way? using the toy cosmology described in the previous milestones. In this setup, only 8 photon multipoles are included, and neutrinos, polarization, Helium, and reionization are all neglected.

Figures A.7, A.8, and A.9 in appendix A show the plots I have made with this toy cosmology. Overall, the agreement is excellent. The only notable differences appear in the baryon velocity and photon multipoles for the smallest scale mode ($k = 0.1\,\text{Mpc}^{-1}$). In the right subplot of figure A.8, the dashed green line shows that v_b dips to much smaller values in my plot than in Winther's, and the relative depths of these dips also differs. However, since the figure uses logarithmic scaling and displays absolute values, these dips simply mark where the perturbation changes sign. This discrepancy likely results from different sampling densities.

Similarly, small differences in the post-recombination oscillations of Θ_0 and Θ_1 for this same mode (see the green curve in figure A.9) are also likely due to differences in sampling. The fact that all other features match closely is a strong validation of the code's accuracy—at least when polarization and neutrinos are excluded from the system.

should I discuss more?

4.3. Results and discussions

4.3.1. Cold dark matter and baryons

Figure 4.1 shows the evolution of the density contrasts δ_{CDM} and δ_b (left panel) and the corresponding velocity perturbations v_{CDM} and v_b (right panel), plotted as functions of $x = \log(a)$ for the four selected wavenumbers mentioned in section 4.2.4. Darker colors correspond to smaller k (larger scales), and vertical dashed lines mark the approximate horizon entry for each mode, estimated by $ck/\mathcal{H} = 1$. should I explain this? The yellow and red lines indicate radiation-matter and matter-dark energy equality, respectively.

Small-scale modes ($k = 1.0, 0.1\,\text{Mpc}^{-1}$) enter the horizon during radiation domination, when the energy density is dominated by relativistic species that cannot cluster efficiently. As a result, gravitational potentials decay, suppressing the growth of matter overdensities—a phenomenon known as the Meszaros effect. In this regime, CDM perturbations grow only logarithmically until matter domination sets in. This suppression is driven indirectly by radiation pressure, which causes the decay of gravi-
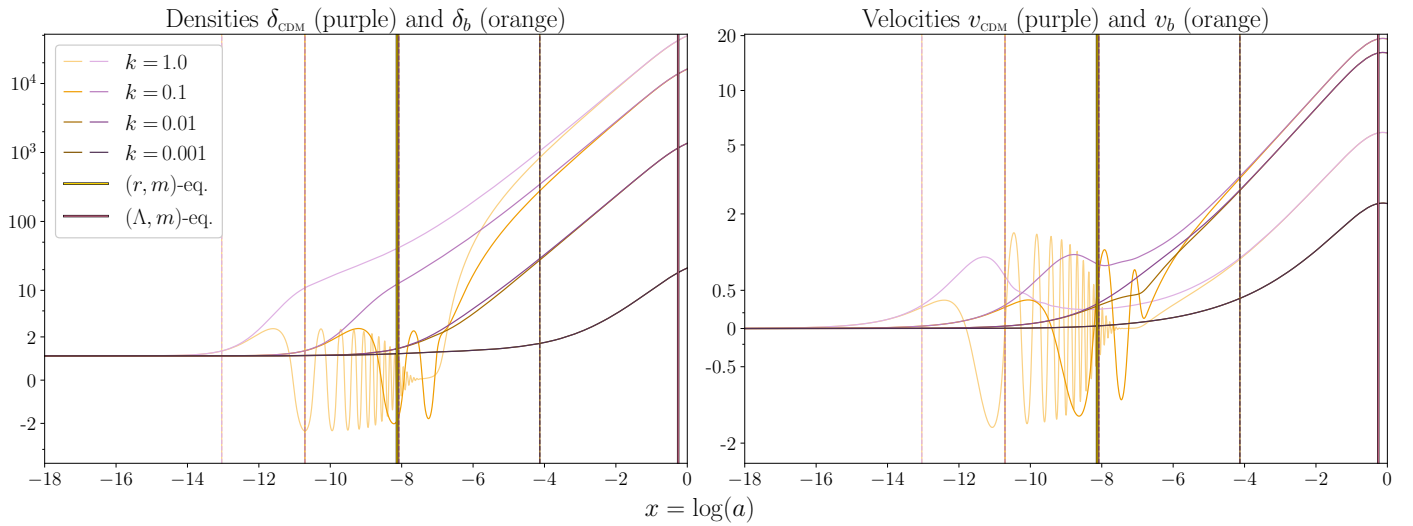
Fig. 4.1. Evolution of the CDM (purple shades) and baryon (orange shades) density (left) and velocity (right) perturbations. Darker lines correspond to larger scales (smaller k, given in units of Mpc^{-1}). An asinh-scaling is used to highlight variations across several orders of magnitude and sign changes. Dashed lines indicate approximate horizon entry times for different modes, while the yellow and red vertical lines mark radiation-matter and matter-dark energy equality, respectively. should I explain the asinh scaling?

tational wells and weakens the gravitational pull that would otherwise enhance CDM growth. Since dark matter does not couple directly to photons, this suppression is slightly delayed compared to baryons. CDM overdensities continue to grow briefly after horizon entry, with velocity perturbations peaking slightly later (e.g., around $x \sim -11.5$ for $k = 1.0\,\mathrm{Mpc}^{-1}$), before growth eventually stalls.

For baryons, the behavior is markedly different prior to recombination. In addition to being affected by the decaying gravitational wells, they experience acoustic oscillations driven by photon pressure due to their tight coupling through Thomson scattering. This is visible in the velocity plot as rapid oscillations for the highest k-mode following horizon entry. The radiation pressure prevents effective baryon clustering, leading to oscillations in δ_b and preventing the growth observed in δ_{CDM}. The onset of oscillations is slightly delayed by the gravitational pull from growing CDM overdensities, which initially drive the baryons into the same potential wells. However, the direct interaction with photons soon dominates, causing the velocity divergence to reverse and oscillate.

The intermediate mode ($k = 0.01\,\mathrm{Mpc}^{-1}$), which enters the horizon around the time of radiation-matter equality, displays a hybrid behavior. Initially, its growth is mildly suppressed by residual radiation pressure, causing the baryon overdensity to lag slightly behind that of dark matter. After recombination, however, the diminishing influence of photon scattering allows baryons to fall freely into CDM potential wells. This leads to the observed convergence of the baryon and CDM perturbations, with any residual oscillations in the baryon velocity field decaying rapidly as pressure support fades. The largest mode ($k = 0.001\,\mathrm{Mpc}^{-1}$) enters the horizon well after matter-radiation equality, and evolves in a regime where gravitational potentials are nearly constant. Consequently, both CDM and baryon overdensities grow roughly in proportion to the scale factor, with steadily increasing and closely aligned velocity perturbations, unaffected by oscillatory behavior.

At late times, after matter-dark energy equality (marked by the red line), the accelerated expansion caused by dark energy suppresses the growth of all matter perturbations. This is re-

flected in the flattening of the density contrast curves and the gradual decrease of velocity perturbations for all modes, and is the result of decaying of gravitational potentials. This leads to a freeze-out in structure formation, and is closely related to the ISW effect mentioned in section 4.1.2.

4.3.2. Photons and neutrinos

Figure 4.2 displays the evolution of the photon density perturbations $\delta_\gamma = 4\Theta_0$ (left panel) and velocity perturbations $v_\gamma = -3\Theta_1$ (right panel), for the same range of k-values as previously. Before horizon entry, all modes evolve slowly and remain nearly constant due to the absence of causal interactions. If a mode enters the horizon before or around the time of recombination, it begins to oscillate due to acoustic waves in the tightly coupled photon-baryon plasma, mimicking the behavior seen for baryons in figure 4.1. These oscillations are governed by the interplay between gravitational compression and the restoring pressure of the photons, effectively behaving like a driven harmonic oscillator.

For the modes that enter the horizon during radiation domination (e.g., $k = 0.1$ and $1.0\,\mathrm{Mpc}^{-1}$), oscillations begin early and with high frequency. However, their amplitude gradually decays over time due to diffusion damping (Silk damping), where photons scatter and diffuse out of overdense regions, erasing anisotropies on small scales. This leads to the observed rapid suppression of oscillations in both δ_γ and v_γ for these high-k modes after radiation-matter equality. In contrast, large-scale modes ($k = 0.001$ and $0.01\,\mathrm{Mpc}^{-1}$) enter the horizon later, during or after matter domination. As a result, they begin oscillating later and at lower frequencies, and their amplitudes are less affected by damping.

The velocity perturbations v_γ track the same oscillation frequency as δ_γ, but are phase-shifted by $\pi/2$, consistent with harmonic oscillator dynamics. Their amplitudes evolve similarly, decreasing with time due to the same damping mechanisms, with small-scale modes decaying more rapidly than large-scale ones. Their sign reflects the direction of bulk photon motion associated with compressions and rarefactions in the fluid.
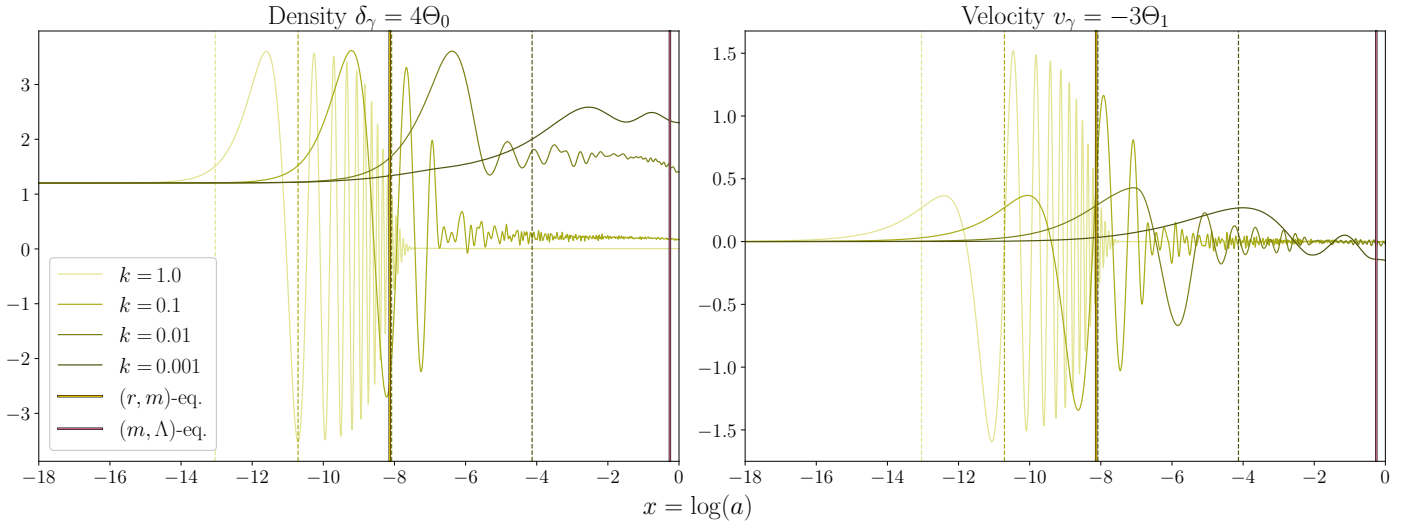
Fig. 4.2. Evolution of photon density $\delta_\gamma = 4\Theta_0$ (left) and velocity $v_\gamma = -3\Theta_1$ (right) perturbations. The photon perturbations grow and oscillate after horizon entry, with oscillations damping over time, especially for small-scale modes after matter-radiation equality.
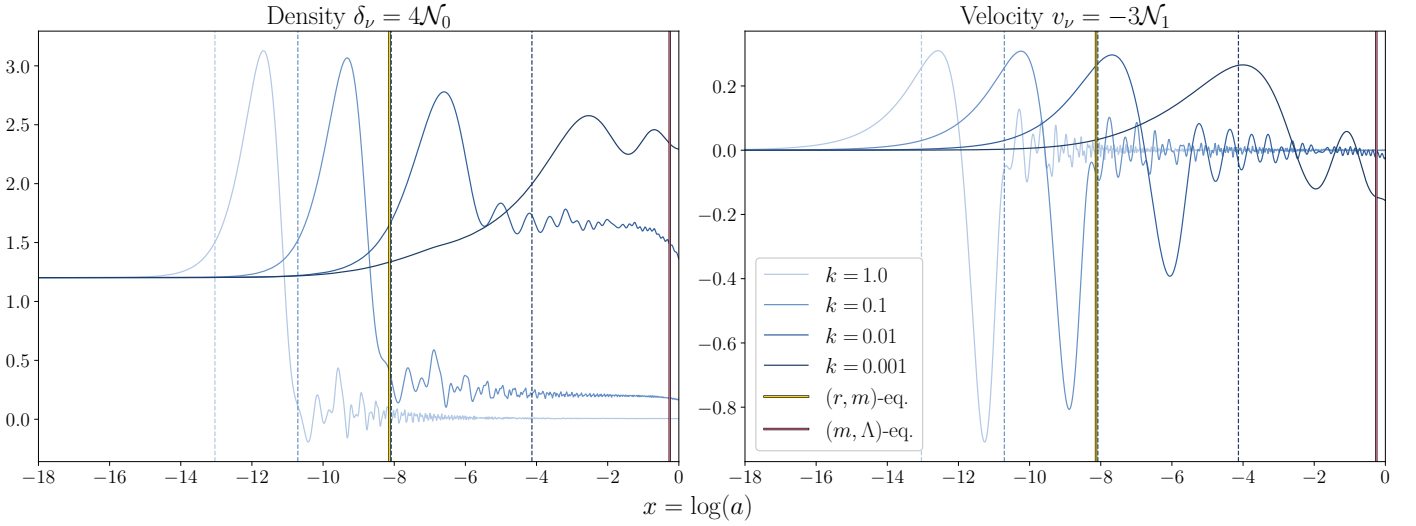
Fig. 4.3. Evolution of neutrino density $\delta_\nu = 4\mathcal{N}_0$ (left) and velocity $v_\nu = -3\mathcal{N}_1$ (right) perturbations. Neutrino perturbations behave similarly to photons at early times but evolve differently due to free-streaming, with scale-dependent residuals emerging after horizon entry.

Figure 4.3 shows the evolution of the neutrino density contrast $\delta_\nu = 4\mathcal{N}_0$ (left) and velocity perturbation $v_\nu = -3\mathcal{N}_1$ (right) for the same range of wavenumbers. Before horizon entry, all perturbations evolve slowly and remain nearly constant, consistent with the causal limitations imposed on superhorizon modes.

Unlike photons, neutrinos decoupled at temperatures around $1\,\mathrm{MeV}$ and have been free-streaming ever since. As a result, their perturbations evolve collisionlessly, and begin to oscillate immediately after horizon crossing. However, because neutrinos do not participate in the tight-coupling dynamics of the photon-baryon fluid, they are not subject to the same restoring forces, and their perturbations are not sustained by acoustic oscillations. Consequently, we see that the velocity and density contrasts in neutrinos decay more rapidly than their photon counterparts. This damping is particularly strong for small-scale modes, where the free-streaming is most effective at erasing inhomogeneities.

At late times, the accelerated expansion driven by dark energy suppresses the growth of all perturbations. For relativistic species like photons and neutrinos, whose energy densities dilute more rapidly with expansion ($\rho_r \propto a^{-4}$), this results in a gradual decline in their density contrasts. This behavior is evident in the intermediate-scale modes shown in figures 4.2 and 4.3, where the perturbations—following an extended period of near-constant oscillations—begin to decay as we approach matter-dark energy equality.

4.3.3. Quadrupole moments

Figure 4.4 shows the evolution of the photon (left) and neutrino (right) quadrupoles. In the left panel, the x-axis is cropped to exclude most of the tight-coupling era, during which Θ_2 is heavily suppressed due to rapid Thomson scattering. After tight-coupling breaks down near recombination, a non-zero photon quadrupole rapidly develops, though its evolution varies strongly with scale. For the largest k-mode, Θ_2 begins oscillating shortly after horizon entry and is quickly damped by residual scattering and diffusion. In contrast, the second largest mode exhibits more pronounced and irregular oscillations that persist further into the matter-dominated era before gradually decaying—highlighting
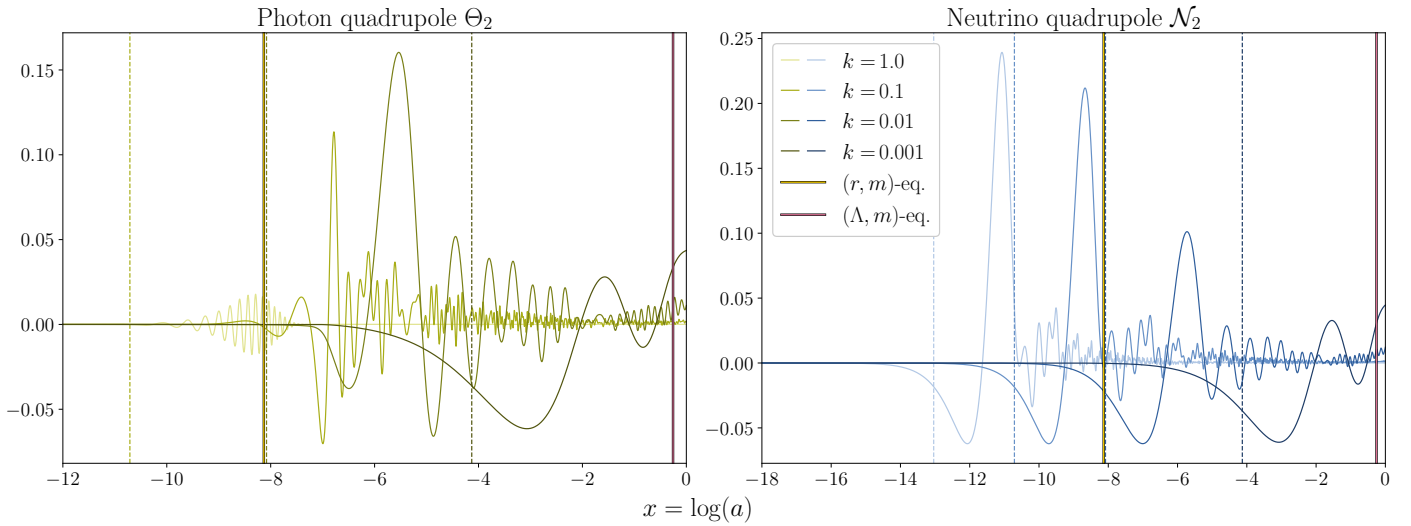
Fig. 4.4. Evolution of the photon quadrupole Θ_2 (left) and the neutrino quadrupole $\mathcal{N}_2$ (right). The photon quadrupole remains suppressed until tight-coupling breaks down, while the neutrino quadrupole freely grows after horizon crossing.

the continued interplay between acoustic driving and damping processes described earlier.

The second smallest k-mode exhibits the most pronounced and sustained oscillations. Although the amplitude gradually decays following recombination, a significant growth is observable around $x \sim -2$, coinciding with the onset of reionization. This timing might suggest that renewed Thomson scattering off free electrons reintroduced during reionization may allow for temporary amplification of the quadrupole through new anisotropic photon scattering. is this reasonable?

Turning to $\mathcal{N}_2$, we observe a visibly different pattern, especially on small scales. Due to the very early neutrino decoupling, their quadrupole begins growing immediately after horizon entry for each mode, unimpeded by scattering. The smaller-scale modes peak at higher amplitudes due to more efficient free-streaming and earlier entry into the horizon, while the large-scale modes enter later and thus remain nearly flat until matter domination. In the radiation-dominated era, neutrinos contribute significantly to the anisotropic stress. Since they can develop a quadrupole immediately upon horizon entry, they also play an important role in the decay of the gravitational potential Φ on subhorizon scales.

A noteworthy late-time feature is the gentle upward trend in both Θ_2 and $\mathcal{N}_2$ for the large- and intermediate-scale modes after matter-dark energy equality. This can be attributed to the decay of gravitational potentials in the dark energy-dominated era, which acts as a source for anisotropies via the ISW effect. The fact that this trend appears in both the photon and neutrino quadrupoles suggests it is unlikely to be a consequence of reionization, as neutrinos are unaffected by scattering processes.

QUESTION: Could the increase towards $x = 0$ be a numerical artifact caused by including too many multipoles? Or does it actually have a physical significance? It disappears if I reduce to 8 multipoles of each type. I'm honestly guessing a little here, because I think it's kinda difficult to interpret.

4.3.4. Polarization multipoles

Figure 4.5 shows the evolution of the photon polarization monopole Θ_0^P (top panel), dipole Θ_1^P (middle panel), and quadrupole Θ_2^P (bottom panel). In contrast to photon temperature

perturbations, all the polarization multipoles are sourced by the anisotropic Thomson scattering that becomes effective only after photon decoupling. Consequently, they are vanishingly small in the early Universe, and the x-axis is cropped in the plot to highlight their relevant evolution.

The smallest-scale mode, which enters the horizon deep in the radiation era, naturally begins oscillating first. Its polarization multipoles closely track the oscillatory pattern of Θ_2 from figure 4.4, consistent with the fact that all polarization multipoles are algebraically related to the temperature quadrupole in the tight-coupling regime. Their oscillations also persist with decreasing amplitude after radiation-matter equality, echoing the damping seen for Θ_2.

The intermediate-scale modes show more irregular oscillatory behavior, with noticeable shifts and non-monotonic amplitudes. This may be partially influenced by reionization at $x \gtrsim -2$, which reintroduces Thomson scattering and allows the quadrupole to again source polarization. Interestingly, Θ_0^P and Θ_2^P for these modes appear to be consistently shifted slightly below zero, suggesting a net anisotropic distortion in one direction due to residual quadrupole contributions or asymmetric reionization effects. or possibly a numerical artifact?

Finally, the largest-scale mode exhibits almost no oscillation in any of the polarization multipoles, despite the quadrupole Θ_2 for this mode showing clear growth after horizon entry. This mismatch is a consequence of the limited causal interaction at such large scales: the polarization generation is inefficient due to the lack of significant Thomson scattering at late times and therefore insufficient anisotropy build-up.

4.3.5. Gravitational potentials

Figure 4.6 shows the evolution of the gravitational potential Φ (left) and the anisotropic stress $\Phi + \Psi$ (right). During radiation domination, Φ remains nearly constant for superhorizon modes, consistent with the conservation of the comoving curvature perturbation $\mathcal{R}$. In contrast, for the smallest-scale modes that enter the horizon during this epoch, Φ decays rapidly. This occurs because the dominating radiation pressure prevents the sustain of stable gravitational potential wells and inhibits efficient matter clustering. As illustrated in figures 4.1 and 4.2, this decay con-
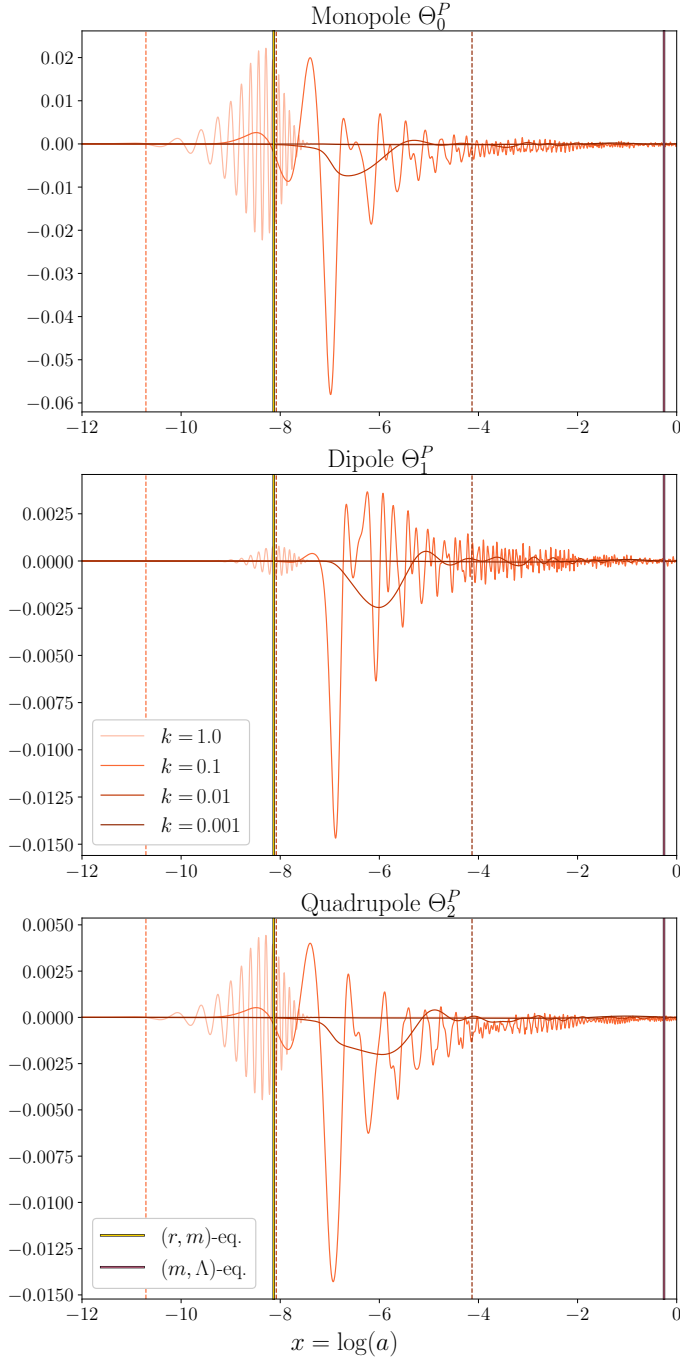
Fig. 4.5. Evolution of the polarization monopole Θ_0^P (top), dipole Θ_1^P (middle), and quadrupole Θ_2^P (bottom). Polarization arises from the temperature quadrupole anisotropy, becoming significant only after tight-coupling ends.

tributes both to the onset of acoustic oscillations in the photon-baryon fluid and to the suppressed growth of CDM overdensities via the Meszaros effect.

The intermediate mode $k = 0.01 \, \mathrm{Mpc}^{-1}$ enters the horizon around the time of radiation-matter equality, and its behavior reflects the transition between these two regimes. Its gravitational potential exhibits a modest decay while radiation still contributes significantly to the total energy density, but soon flattens as CDM begins to dominate and support stable potential wells. This pattern aligns with the sustained growth of matter perturbations seen for this mode and helps explain its prolonged oscilla-

tory behavior in the photon and neutrino quadrupole plots (figure 4.4).

For the largest scale, which enters well after matter domination, Φ remains nearly constant after horizon entry. Here, CDM clustering is fully efficient, and the lack of significant radiation pressure means potential wells remain effectively static. This reflects the standard Meszaros transition, where structure formation proceeds unimpeded by relativistic species. At late times, however, all modes exhibit a decline in Φ as dark energy becomes dominant. As mentioned briefly in the previous sections, this decay of potentials contributes to the late-time ISW effect, which sources large-scale temperature anisotropies in the CMB.

The right panel of figure 4.6 illustrates how the anisotropic stress $\Phi + \Psi$ evolves across different scales and epochs. For high-k modes entering the horizon during radiation domination, we observe a rapid decline from the initial positive value, followed by oscillations around zero with a decaying amplitude. This pattern reflects the onset of anisotropic stress caused by free-streaming neutrinos. As seen in figure 4.4, the neutrino quadrupole $\mathcal{N}_2$ grows rapidly once a mode enters the horizon, generating anisotropic stress that alters the Einstein equations by suppressing Ψ relative to Φ (see eq. (4.43)). This in turn causes $\Phi + \Psi$ to deviate from its initial value and oscillate.

These oscillations also affect the evolution of Φ, as both Ψ and the neutrino quadrupole $\mathcal{N}_2$ enter its differential equation (eq. (4.42)). On small scales, this coupling drives the rapid decay of the gravitational potentials. As the Universe transitions to matter domination, the impact of free-streaming relativistic species weakens, leading to a gradual decline in anisotropic stress. For the intermediate mode ($k = 0.01 \, \mathrm{Mpc}^{-1}$), this change appears as a brief dip in $\Phi + \Psi$ just after horizon entry, followed by a steady return toward zero, reflecting the residual but diminishing influence of radiation. In contrast, the largest-scale mode exhibits only a modest positive bump before smoothly flattening out. In both cases, $\Phi + \Psi$ approaches zero at late times, consistent with a pressureless fluid in which anisotropic stress vanishes and $\Phi = -\Psi$.

QUESTION: Is it okay to have this subsection at the end? I placed it here because I wanted to refer to the quadrupole plots when discussing the anisotropic stress, but I don't know if these things should be presented earlier.

5. Milestone IV: Power Spectra

Having explored the background evolution of the Universe, its thermal history, and the growth of perturbations, we now reach the final step: computing the primary statistical observables in cosmology—the CMB power spectrum and the matter power spectrum. These spectra encode the evolution of perturbations from their initial conditions to their imprint on the cosmic microwave background and the large-scale distribution of matter. Their precise computation allows us to compare theoretical predictions with observations from missions such as Planck, placing stringent constraints on cosmological parameters.

The CMB power spectrum quantifies temperature and polarization anisotropies in the CMB sky, which arise from acoustic oscillations in the early Universe, gravitational redshifting, and scattering effects. To compute this spectrum, we must perform line-of-sight integration, tracing how photons have propagated from recombination to today, incorporating contributions from Sachs-Wolfe effects, Doppler shifts, and polarization terms. The matter power spectrum, on the other hand, describes how density fluctuations in the Universe are distributed across different scales today. It is derived from the total matter perturbations, including
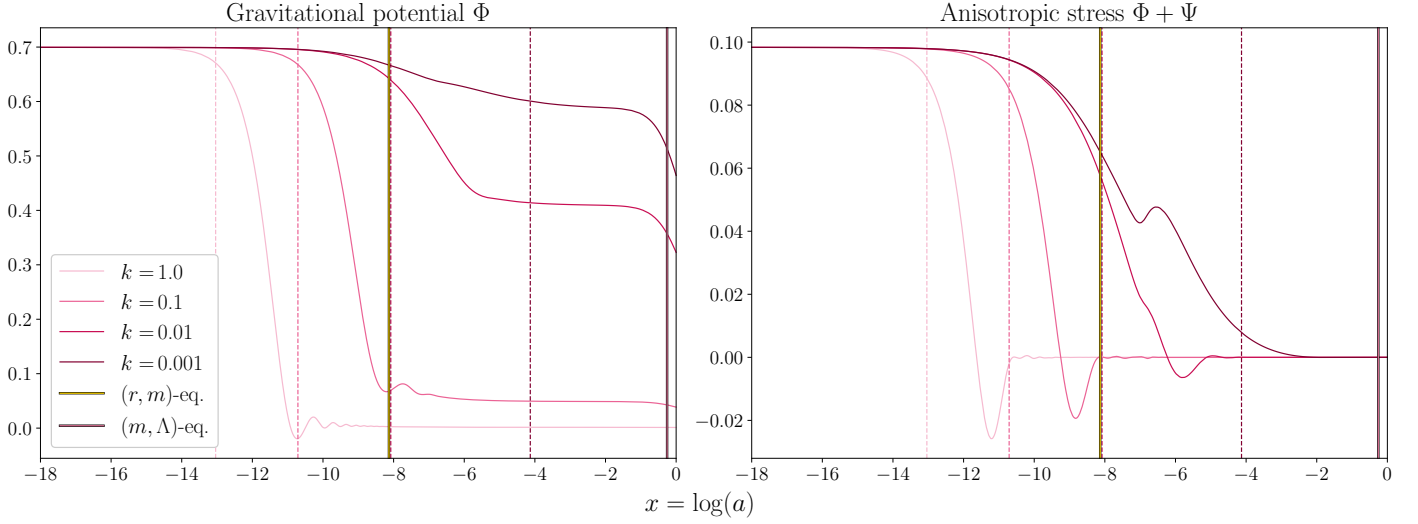
Fig. 4.6. Evolution of the gravitational potential Φ (left) and the anisotropic stress $\Phi + \Psi$ (right). Small-scale modes that enter the horizon during radiation domination exhibit decaying Φ and oscillatory $\Phi + \Psi$, while large-scale modes preserve nearly constant potentials until dark energy domination.

contributions from dark matter and baryons, and plays a crucial role in understanding the formation of large-scale structure.

By synthesizing the physics from all previous milestones, this milestone brings us to the final stage of our Einstein-Boltzmann solver. The results will allow direct comparison with observational data, testing the validity of our theoretical model and its numerical implementation.

<mark>TODO: shorten/word different to fit the rest</mark>

5.1. Theoretical framework

5.1.1. Temperature fluctuations as spherical harmonics

<mark>TODO: find better name</mark>

To begin understanding the CMB power spectrum, we must connect our theoretical results to the actual observable: the temperature fluctuations of the CMB across the sky. These are quantified by the temperature field $\Theta(t, \boldsymbol{x}, \hat{p})$ introduced in the previous milestone, which we already know how to solve for in Fourier space. Since the sky is a two-dimensional sphere, it is natural to expand this temperature field in terms of spherical harmonics:

$$\Theta(t, \boldsymbol{x}, \hat{p}) = \sum_{\ell=1}^{\infty} \sum_{m=-\ell}^{\ell} a_{\ell m}(t, \boldsymbol{x}) Y_{\ell m}(\hat{p}). \tag{5.1}$$

Here, $Y_{\ell m}$ are the spherical harmonic functions that form a complete basis on the sphere, and the coefficients $a_{\ell m}$ describe the amplitude of fluctuations at angular scale ℓ and azimuthal mode m. By expressing Θ in terms of its Fourier components we can compute these coefficients as

$$a_{\ell m}(t, \boldsymbol{x}) = \int \frac{d^3 k}{2\pi^3} e^{i\boldsymbol{k}\cdot\boldsymbol{x}} \int Y_{\ell m}^*(\hat{p}) \Theta(t, \boldsymbol{k}, \hat{p}) \, d\Omega_{\hat{p}}. \tag{5.2}$$

<mark>TODO: remove? rewrite to fit 4.17 and 4.18?</mark>

The multipole index ℓ is inversely related to the angular scale: low ℓ values correspond to large angular scales (broad patterns on the sky), while high ℓ values probe finer angular features. The m index corresponds to different orientations of the pattern at a fixed angular scale. However, since the Universe is

assumed to be statistically isotropic, the ensemble average of the temperature field must be invariant under rotations. This implies that there should be no preferred direction on the sky, and hence no statistical dependence on m. Consequently, we define the angular power spectrum as the variance of $a_{\ell m}$ over m:

$$C_\ell \equiv \langle |a_{\ell m}|^2 \rangle = \frac{1}{2\ell + 1} \sum_{m=-\ell}^{\ell} |a_{\ell m}|^2. \tag{5.3}$$

Thus, the CMB power spectrum C_ℓ provides the average amplitude of temperature fluctuations as a function of angular scale ℓ, and is the primary quantity we compare to observations.

A crucial point to emphasize is that we only observe one realization of the Universe. Theoretically, the average $\langle \cdot \rangle$ is meant to be an ensemble average over many universes with the same statistical properties. In practice, we must replace this ensemble average with an average over the $2\ell + 1$ available m-modes at each ℓ, assuming ergodicity. <mark>TODO: maybe fix redundancy</mark> This leads to a fundamental statistical limitation called cosmic variance. Since there are fewer m-modes at low ℓ, our estimate of C_ℓ becomes increasingly uncertain on large angular scales. The cosmic variance is quantified by

$$\frac{\text{Var}(C_\ell)}{C_\ell^2} = \frac{2}{2\ell + 1}, \tag{5.4}$$

which shows that the relative uncertainty is larger for small ℓ. Importantly, this is not a limitation of our instruments or data analysis, but a fundamental property of observing only one sky. As $\ell \to 0$, the number of independent modes becomes too small to robustly determine C_ℓ, leading to large uncertainties in the low-ℓ regime of the power spectrum.

5.1.2. Line-of-sight integration

To calculate the CMB angular power spectrum C_ℓ, we need the temperature multipoles $\Theta_\ell(k)$ at present time. A naive approach would be to evolve the full Boltzmann hierarchy for each ℓ up to some large $\ell_{\max} \sim 1000$, which would involve solving thousands of coupled differential equations for every mode k. While this

is theoretically feasible, it is extremely computationally expensive. Fortunately, a clever method known as line-of-sight (LOS) integration (see add citation!) offers an elegant and much more efficient alternative. Rather than evolving the entire Boltzmann hierarchy, this method instead solves for the monopole at all times and positions and then integrates over the photon path to determine the final anisotropies observed today. This drastically reduces the computational cost, requiring us to compute only a handful of lower multipoles, as mentioned in the previous milestone. TODO: word different?

At the heart of the LOS approach lies the source function $\tilde{S}(k, x)$, which captures all physical effects that contribute to the temperature anisotropies observed in the CMB. It is derived by formally integrating the photon temperature perturbation equation from the last milestone, and isolating the directional dependence through integration by parts and multipole expansion. The final expression for the temperature multipole at present time $x = 0$ is

$$\Theta_\ell(k, x = 0) = \int_{-\infty}^{0} \tilde{S}(k, x) j_\ell[k(\eta_0 - \eta)] \, dx \qquad (5.5)$$

where j_ℓ are the spherical Bessel functions. Their appearance in the integral arises from the projection of three-dimensional spatial perturbations (characterized by wavevector magnitude k) onto the two-dimensional sky (characterized by angular multipole moment ℓ). These functions emerge naturally when decomposing the plane wave $e^{i\boldsymbol{k}\cdot\boldsymbol{x}}$ into spherical harmonics and radial functions, and encode how fluctuations in a Fourier mode k contribute to angular anisotropies at a given scale ℓ.

One can show that the source function itself is given by:

$$\tilde{S}(k, x) = \tilde{g}\left[\Theta_0 + \Psi + \frac{1}{4}\Pi\right] + e^{-\tau}(\Psi' - \Phi') - \frac{1}{ck}\frac{d}{dx}(\mathcal{H}\tilde{g}v_b)$$
$$+ \frac{3}{4c^2k^2}\frac{d}{dx}\left[\mathcal{H}\frac{d}{dx}(\mathcal{H}\tilde{g}\Pi)\right], \qquad (5.6)$$

Each term here has a specific physical interpretation: the first represents the monopole contribution (weighted by visibility), corrected by the gravitational redshift (Sachs-Wolfe effect) and polarization part of the SW effect? . Furthermore, $e^{-\tau}(\Psi' - \Phi')$ is simply the integrated Sachs-Wolfe (ISW) term, while the Doppler effect enters through the third term. The final term, involving Π, is a quadrupolar correction to the scattering due to anisotropic Thomson scattering, and includes polarization effects. In total, these terms encapsulate the full physics of how inhomogeneities in the early Universe source temperature anisotropies observed today.

5.1.3. Computing the temperature power spectrum

rename section?

Having computed the photon temperature multipoles $\Theta_\ell(k)$ through the line-of-sight integration method, we are in a position to extract one of the most important observables in modern cosmology: the angular CMB temperature power spectrum. This is computed by first squaring the photon temperature multipoles obtained via the LOS method (eq. (5.5)). We then multiply this with the primordial power spectrum mentioned in section 4.1.9 and integrate over all wave numbers k, which gives us:

$$C_\ell = \frac{2}{\pi} \int k^2 P_{\text{primordial}}(k) |\Theta_\ell(k)|^2 \, dk. \qquad (5.7)$$

Fortunately, most of the simplest single field inflation models predict a so-called Harrison-Zel'dovich spectrum:

$$P_{\text{primordial}}(k) = \frac{2\pi^2}{k^3}\mathcal{P}_{\mathcal{R}}(k) = \frac{2\pi^2}{k^3}A_s\left(\frac{k}{k_{\text{pivot}}}\right)^{n_s-1}, \qquad (5.8)$$

where A_s is the primordial amplitude, $n_s \sim 1$ is the spectral index, and k_{pivot} is a chosen reference scale. explain origin? Thus, using that the temperature multipoles $\Theta_\ell(k)$ must be real since they represent physical observables correct? , we may rewrite eq. (5.7) as

$$C_\ell = 4\pi \int A_s\left(\frac{k}{k_{\text{pivot}}}\right)^{n_s-1} \Theta_\ell^2(k)\frac{dk}{k}, \qquad (5.9)$$

Given the full theoretical C_ℓ spectrum, we can generate a synthetic realization of the CMB sky. This is interesting for comparing theory to actual observations, for visualizing the random nature of the CMB, and for generating mock data sets. However, to do this we must compute the coefficients $a_{\ell m}$ defined in eq. (5.2). A simple method for doing this is to sample them as complex Gaussian random variables with variance C_ℓ, i.e.,

$$a_{\ell m} = \sqrt{-\log(A)C_\ell}\,e^{2\pi i\theta}, \qquad (5.10)$$

where A and θ are random numbers drawn from a uniform distribution over $[0, 1)$. To ensure that $T(\hat{n})$ is real-valued, we enforce:

$$a_{\ell,-m} = (-1)^m a_{\ell m}^*. \qquad (5.11)$$

Once the $a_{\ell m}$'s are generated, the temperature map can be constructed using the HEALPIX library add citation! , which perform the spherical harmonic synthesis efficiently.

move/rewrite/specify in implementation?

5.1.4. Features in the CMB

rename section? combine with previous?

The prominent peaks and troughs observed in the power spectrum arise from acoustic oscillations in the tightly coupled photon-baryon fluid before recombination. These oscillations are the result of competition between gravitational collapse and photon pressure in the early Universe. Overdense regions begin to collapse under gravity, but the intense radiation pressure from photons resists compression, resulting in oscillatory behavior analogous to sound waves.

From figure 3.3 presented in milestone II we know that the visibility function $\tilde{g}$ is sharply peaked around recombination. A rough approximation is thus $\tilde{g} \approx \delta(x - x_{\text{rec}})$, which according to eq. (5.5) leads to

$$\Theta_\ell^{\text{today}}(k) \approx \left[\Theta_0 + \Psi + \frac{\Pi}{4}\right]_{\text{rec}} j_\ell[k(\eta_0 - \eta_{\text{rec}})] \approx [\Theta_0 + \Psi]_{\text{rec}}\, j_\ell(k\eta_0).$$
$$(5.12)$$

The second approximation follows from the fact that the anisotropy term is very small at recombination, and that $\eta_{\text{rec}} \ll \eta_0$. word different? Thus, we know that the dominant contribution to the observed anisotropies must come from the effective temperature perturbation at the time of recombination ($[\Theta_0 + \Psi]_{\text{rec}}$).

To understand how this perturbation evolves, we may consider the coupled evolution equations for the monopole and dipole in terms of the conformal time:

$$\frac{\partial \Theta_0}{\partial \eta} = -k\Theta_1 - \frac{\partial \Phi}{\partial \eta}, \tag{5.13}$$

$$\frac{\partial \Theta_1}{\partial \eta} = \frac{k}{3}(\Theta_0 - 2\Theta_2 + \Psi) + \frac{\partial \tau}{\partial \eta}\left(\Theta_1 + \frac{v_b}{3}\right), \tag{5.14}$$

Combining these equations (by differentiating the first and substituting into the second), we obtain a second-order differential equation of the form:

$$\frac{\partial^2(\Theta_0 + \Psi)}{\partial \eta^2} + \frac{k^2}{3}(\Theta_0 + \Psi) = F, \tag{5.15}$$

where the right-hand side acts as a driving force that includes contributions from higher-order multipoles and gravitational evolution:

$$F = \frac{2}{3}k^2\Theta_2 - k\frac{d\tau}{d\eta}\left(\Theta_1 + \frac{v_b}{3}\right) + \frac{d^2(\Psi - \Phi)}{d\eta^2}. \tag{5.16}$$

TODO: continue, mention most/all of the following:

1. Baryon loading
2. Radiation driving
3. Diffusion damping
4. Sachs-Wolfe plateau
5. Widths and relative heights of the first three peaks
6. The damping tail
7. Effects of reionization

TODO: maybe not focus on derivations?

5.1.5. Polarization spectra

TODO: write to fit milestone III

5.1.6. Effects of gravitational lensing

Gravitational lensing refers to the bending of light caused by the gravitational potential of massive structures between the source and the observer. As CMB photons from the last scattering surface travel through inhomogeneities in the large-scale structure on their way towards us, their paths are slightly deflected. This phenomenon introduces subtle distortions to the observed temperature and polarization anisotropies of the CMB. While the deflections are small, their cumulative effect leads to a measurable smoothing of the acoustic peaks in the observed angular power spectra by effectively redistributing power across multipoles. word different?

In order to compute the effect of gravitational lensing, we first need the CMB lensing potential C_ℓ^Ψ. This is found using LOS integration in the same way as the temperature multipoles (eq. (5.5)), with the source function being

$$\tilde{S}_\Psi = -\frac{2c\Psi}{\mathcal{H}(\eta_0 - \eta)}W(\chi, \chi_s). \tag{5.17}$$

where χ_s corresponds to the comoving distance to the last scattering surface. Here, the window function is

$$W(\chi, \chi_s) = \frac{S_k(\chi - \chi_s)}{S_k(\chi_s)}, \quad \text{for } \chi \geq \chi_s, \tag{5.18}$$

and zero otherwise, with the function $S_k(\chi)$ depending on spatial curvature k (see section 2.1.1):

$$S_k(\chi) = \begin{cases} \sin\chi, & k = 1, \\ \chi, & k = 0, \\ \sinh\chi, & k = -1. \end{cases} \tag{5.19}$$

rewrite to fit rest of text?

To quantify angular correlations in the CMB temperature anisotropies, we make use of the angular correlation function $C(\theta)$. This measures how the temperature fluctuations at two different directions $\hat{n}_1$ and $\hat{n}_2$ on the sky, separated by an angle θ, are statistically related. The theoretical prediction for this quantity is given by the Legendre series expansion:

$$C(\theta) = \frac{1}{4\pi}\sum_\ell (2\ell + 1)C_\ell P_\ell(\cos\theta). \tag{5.20}$$

However, the presence of massive structures alters this expression, leading to a lensed correlation function. This is approximately given by:

$$C^{\text{lensed}}(\theta) \approx \frac{1}{4\pi}\sum_\ell (2\ell + 1)C_\ell \exp\left[-\frac{\ell(\ell+1)}{2}\sigma^2(\theta)\right]$$
$$\times \left[P_\ell(\cos\theta) + \frac{\ell(\ell+1)}{2}C_{\text{gl},2}(\theta)d_{1,-1}^\ell(\theta)\right], \tag{5.21}$$

where the variance

$$\sigma^2(\theta) = C_{\text{gl}}(0) - C_{\text{gl}}(\theta) \tag{5.22}$$

encodes the lensing-induced smoothing, and

$$C_{\text{gl}}(\theta) = \sum_\ell \frac{2\ell+1}{4\pi}\ell(\ell+1)C_\ell^\Psi d_{1,1}^\ell(\theta), \tag{5.23}$$

$$C_{\text{gl},2}(\theta) = \sum_\ell \frac{2\ell+1}{4\pi}\ell(\ell+1)C_\ell^\Psi d_{-1,1}^\ell(\theta). \tag{5.24}$$

In these expressions, d_{mn}^ℓ are the reduced Wigner functions:

$$d_{mn}^\ell(\theta) = \sum_i (-1)^i \frac{\sqrt{(\ell+m)!(\ell-m)!(\ell+n)!(\ell-n)!}}{(\ell+m-i)!(\ell-n-i)!i!(i+n-m)!}$$
$$\times \cos^{2\ell+m-n-2i}\left(\frac{\theta}{2}\right)\sin^{2i+n-m}\left(\frac{\theta}{2}\right), \tag{5.25}$$

with the sum running over all integers i such that the factorials are non-negative. By integrating the lensed correlation function over all angles, we thus obtain the lensed power spectrum:

$$C_\ell^{\text{lensed}} = 2\pi \int_{-1}^1 C^{\text{lensed}}(\theta)P_\ell(\cos\theta)\,d\cos\theta. \tag{5.26}$$

rewrite to better the flow

mention what is useful about these quantities?

5.1.7. The neutrino power spectrum

In addition to photons, neutrinos also decouple early in the Universe's history and subsequently free-stream, carrying imprints of primordial perturbations. While we currently lack the observational capability to directly measure the anisotropies in the cosmic neutrino background, it is nevertheless possible to compute a theoretical neutrino power spectrum. This can be useful

both for understanding their effect on the photon spectrum and as a consistency check within the Einstein-Boltzmann framework.

Neglecting higher-order multipoles such as the quadrupole, the source function for neutrinos can be written as:

$$\tilde{S}_\nu = (\mathcal{N}_0 + \Psi)\delta(\eta) + \frac{d\Psi}{dx} - \frac{d\Phi}{dx}, \tag{5.27}$$

The structure of this equation clearly shows that the neutrino spectrum receives contributions from both the SW term and the ISW term. The absence of the exponential optical depth factor $e^{-\tau}$, present in the photon source function, reflects the fact that neutrinos are unaffected by reionization or scattering processes.

`merge into earlier sections?`

5.1.8. The matter power spectrum

The matter power spectrum is a statistical tool that captures the distribution of matter density fluctuations across scales. It tells us how matter is clumped in the Universe at different spatial wavelengths, or equivalently, how different Fourier modes k contribute to the overall structure. The shape of this spectrum is determined by the primordial power spectrum generated during inflation, as well as the growth (or suppression) of structure depending on whether a mode is inside or outside the horizon. The latter also depends onwhether the Universe is radiation or matter dominated, as we will see. `word different?`

The general form of the matter power spectrum is given by

$$P(k, x) = |\Delta_M(k, x)|^2 P_{\text{primordial}}(k), \tag{5.28}$$

where

$$\Delta_m(k, x) = \frac{2}{3} \frac{c^2 k^2 \Phi(k, x)}{\Omega_{m0} H_0^2} e^x, \tag{5.29}$$

is the transfer function representing the growth of matter perturbations over time. `derive this?`

`TODO: maybe explain Meszaros effect`

As with the CMB, it is most interesting to study the matter power spectrum today, since this is what we observe. It is then common to show k in units of h/Mpc and $P(k)$ in units of $(\text{Mpc}/h)^3$ `because of degeneracies?`. It is also helpful to mark the scale of matter-radiation equality,

$$k_{\text{eq}} = \frac{a_{\text{eq}} H(a_{\text{eq}})}{c}, \tag{5.30}$$

since this sets the transition between modes that entered the horizon during radiation domination versus those that entered later during matter domination.

`TODO: change notation to fit milestone I`

`TODO: rewrite section to fit milestone III results`

5.1.9. The correlation function

While the matter power spectrum is crucial for understanding structure evolution, it is sometimes more intuitive to consider its Fourier transform, the correlation function $\xi(r)$ in real space. This gives the excess probability (relative to a random distribution) of finding a pair of matter overdensities separated by a distance r, and is derived by using spherical symmetry to reduce the 3D Fourier transform to a 1D Hankel transform:

$$\xi(r) = \int_0^\infty \frac{\sin(kr)}{kr} \frac{k^3 P(k)}{2\pi^2} \frac{dk}{k}. \tag{5.31}$$

Alternatively, eq. (5.31) can be rewritten as a regular 1D Fourier transform by defining

$$f(k) = \frac{kP(k)}{4\pi^2} \tag{5.32}$$

and then using the identity

$$r\xi(r) = \int_{-\infty}^\infty f(k)e^{ikr} dk, \tag{5.33}$$

where we assume $f(k) = f^*(-k) = -f(-k)$ to ensure reality and symmetry. This form is numerically convenient for fast computations using, for instance, FFTLog. `add citation?`

A particularly significant feature in the correlation function is a bump at the sound-horizon scale r_{drag}. This is known as the BAO peak, and is a direct imprint of acoustic waves in the photon-baryon fluid before recombination. As we know from milestone II, baryons were dragged along with photons during the drag epoch due to their strong coupling, forming a pressure-supported sound wave that propagated outward from initial overdensities. When decoupling occurred, this sound wave "froze in", leaving behind a characteristic excess of matter at a fixed comoving separation r_{drag}. In real space, this corresponds to a spherical shell of enhanced density, and in Fourier space, to oscillations in the matter power spectrum. `don't make redundant`

`TODO: rewrite clumsy sentences`

5.2. Implementation details

5.2.1. Main program structure

`TODO: maybe explain source funcs here`

5.2.2. Initial conditions

`TODO: short section, maybe merge into next`

5.2.3. Integration limits and points

`TODO: mention sampling criteria`

5.2.4. Tolerances

`TODO: explain polarization and lensing`

5.2.5. Testing the code

`TODO`

5.3. Results and discussions

5.3.1. The transfer function

Figure 5.1 presents the transfer function $\Theta_\ell(k)$ (left panel) and the integrand of the CMB angular power spectrum integral $|\Theta_\ell(k)|^2/k$ (right panel), evaluated for a range of multipoles ℓ. For clarity and better comparison across ℓ, the left panel is scaled by $\sqrt{\ell(\ell+1)}$ and the right panel by $\ell(\ell+1)$, making the relative contributions more visually apparent.

In both subplots, the curves reveal where in k-space the dominant contributions to the temperature anisotropies arise. We see that as ℓ increases, the peak of the integrand shifts to higher k,
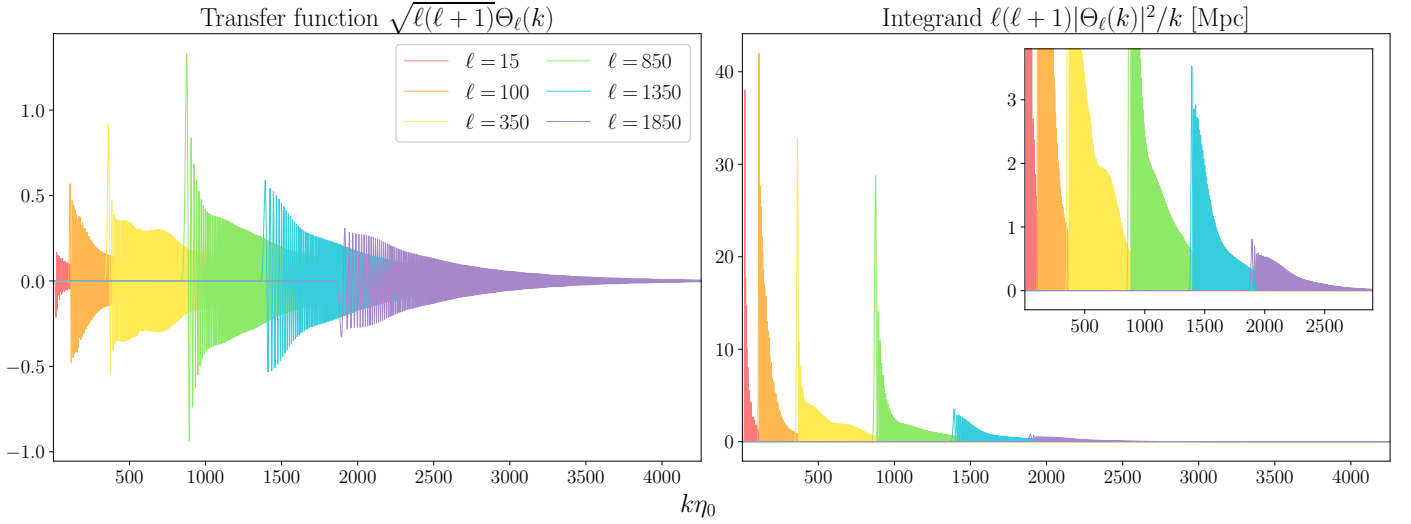
Fig. 5.1. The transfer function $\Theta_\ell(k)$ (left) and the integrand $|\Theta_\ell(k)|^2/k$ (right) for selected multipoles ℓ. The transfer function describes the projection of primordial perturbations onto angular scales today, while the integrand determines the contribution of each mode k to the angular power spectrum C_ℓ. TODO: maybe change

confirming that small-scale modes predominantly source high-ℓ power. This is consistent with the approximate projection relation $k \sim \ell/\eta_0$, and illustrates the relationship between spatial and angular scales in cosmological perturbation theory. It also highlights key features that shape the observed spectrum C_ℓ, such as the oscillatory structure and damping at small scales. TODO: maybe change

5.3.2. The CMB temperature power spectrum

Figure 5.2 presents the final CMB temperature power spectrum C_ℓ^{TT} computed using the line-of-sight formalism discussed in section 5.1.2, plotted with conventional normalization in units of μK^2. Superimposed are the observational data from the Planck satellite, with orange error bars representing low-ℓ data and purple bars corresponding to high-ℓ measurements. The inset in the top-left corner shows a magnified view of the high-ℓ region.

The spectrum exhibits the well-known acoustic peak structure, arising from oscillations in the tightly coupled photon-baryon plasma prior to recombination (see section 5.1.4). The first peak at $\ell \sim 220$ corresponds to modes that underwent a full compression phase, while subsequent peaks correspond to higher harmonics. As expected, the odd-numbered peaks are amplified due to baryon loading, and the relative suppression of even-numbered peaks encodes the baryon-to-photon ratio. These features are direct consequences of the physics described by the harmonic oscillator formulation of the photon monopole perturbation in the presence of gravity and baryons.

TODO: we treat neutrinos as massless?

TODO: truncating the hierarchy too early?

5.3.3. TE and EE polarization power spectra

5.3.4. The neutrino power spectrum

5.3.5. The matter power spectrum

Figure 5.6 shows the matter power spectrum $P(k)$ today, plotted in units of $(\mathrm{Mpc}/h)^3$ as a function of the wavenumber k in h/Mpc. The black curve represents the theoretically computed

spectrum, while blue and green error bars show observational data from CMB measurements by the Wilkinson Microwave Anisotropy Probe (WMAP) and the Acatama Cosmology Telescope (ACT), and the Sloan Digital Sky Survey (SDSS) DR7 Luminous Red Galaxies (LRGs), respectively. TODO: rephrase

As detailed in section 5.1.8, the shape of the matter power spectrum reflects both the primordial spectrum seeded during inflation and the subsequent growth of perturbations across spatial scales. In particular, the turnover near the scale k_{eq} (marked on the plot) corresponds to the mode that entered the horizon at matter-radiation equality. Modes with $k \ll k_{\mathrm{eq}}$ entered the horizon during matter domination and grew efficiently due to gravitational instability. Conversely, modes with $k \gg k_{\mathrm{eq}}$ entered during radiation domination, when the rapid expansion and pressure support from relativistic species suppressed growth, resulting in the $\propto k^{-3}$ decline of $P(k)$ at large k.

TODO: discuss how the primordial spectrum is visible

The plot also marks the baryon acoustic oscillation (BAO) scale $2\pi/r_{\mathrm{drag}}$, which arises from sound waves in the early Universe's photon-baryon fluid and appears as a characteristic scale in both the matter and CMB power spectra. Although the BAO wiggles are less pronounced in the matter power spectrum due to the smoothing effect of nonlinear evolution, they are still visible. TODO: change/remove this

The agreement between the computed spectrum and observational data is generally good across a wide range of scales. On large scales ($k \lesssim 0.1\,h/\mathrm{Mpc}$), the model accurately matches both the CMB and galaxy data, confirming the consistency of the perturbation evolutions with initial inflationary conditions. TODO: word different On smaller scales ($k \gtrsim 0.1\,h/\mathrm{Mpc}$), the slight deviations likely stem from nonlinear clustering effects not captured in our linear treatment. Additionally, galaxy bias and redshift-space distortions introduce observational systematics in the SDSS measurements, which may also contribute to discrepancies. TODO: add source
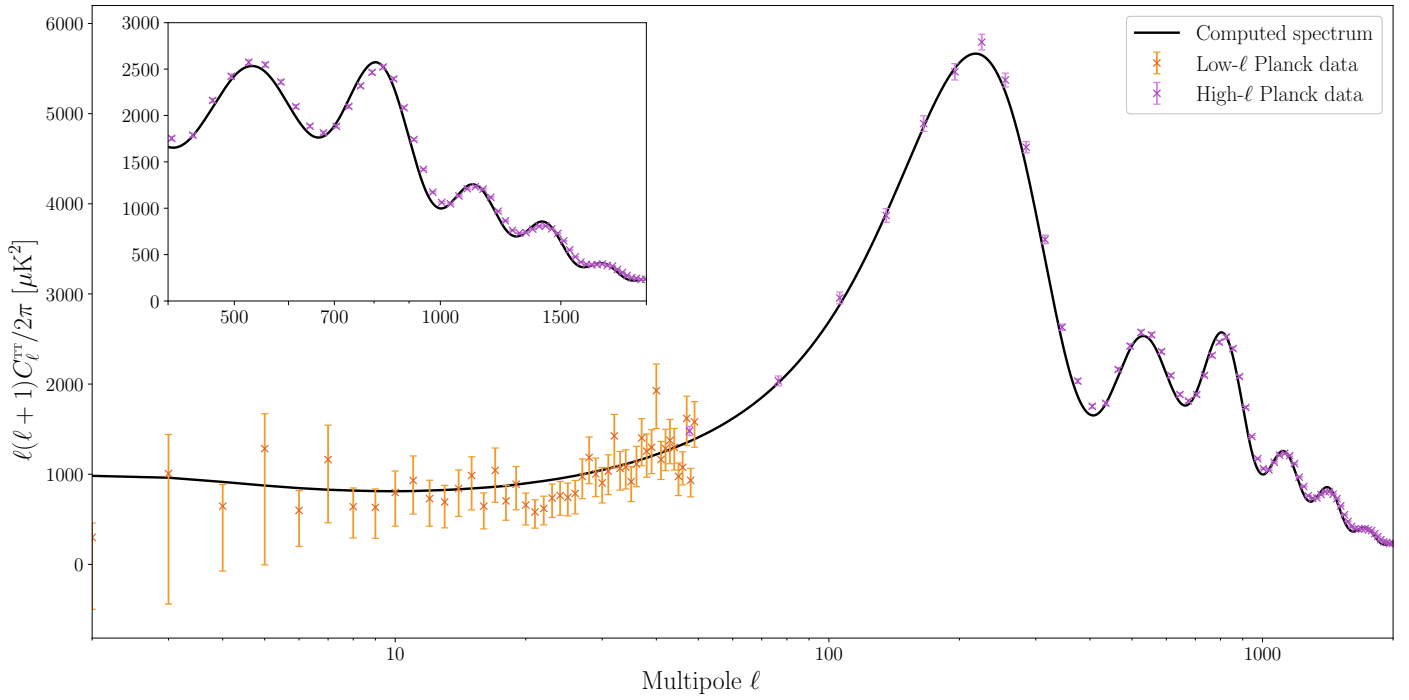
Fig. 5.2. The CMB temperature power spectrum C_ℓ^{TT} (black) compared with Planck low-ℓ (orange) and high-ℓ (purple) data points. The inset highlights a zoom on the high-ℓ region. The first three peaks are clearly visible, and the agreement with data is overall good, though the computed peaks are slightly higher, likely due to the absence of gravitational lensing smoothing. TODO: maybe change
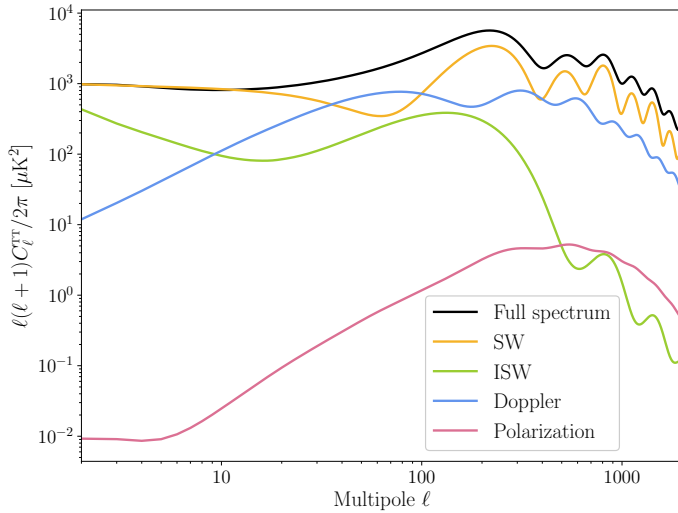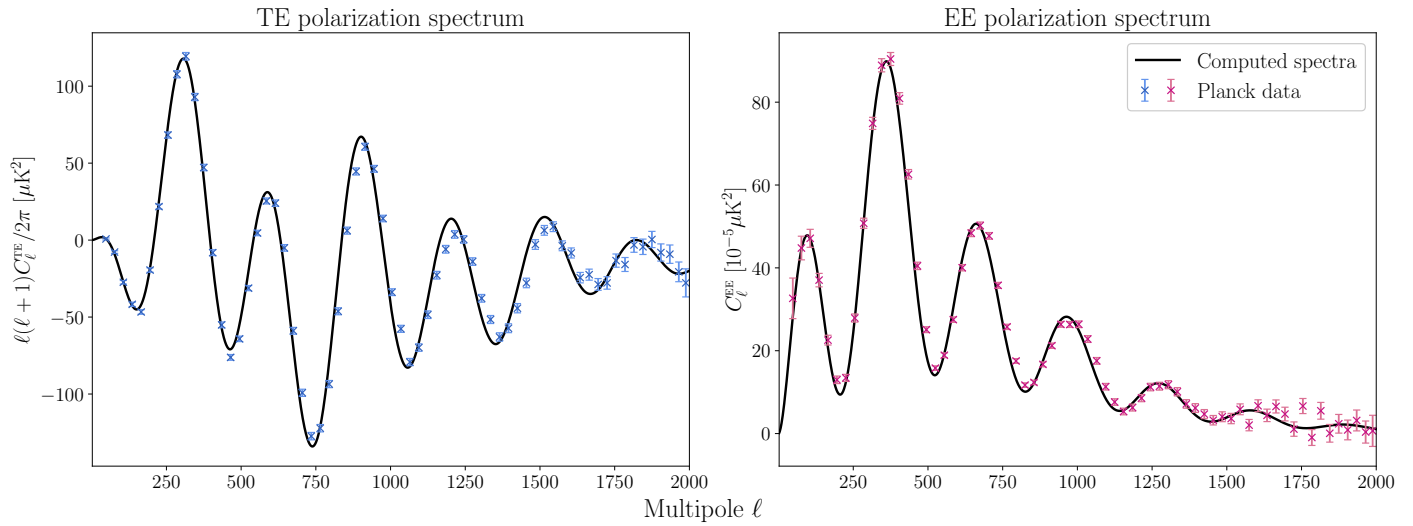

Fig. 5.3. Breakdown of the individual contributions to the CMB temperature power spectrum. The Sachs-Wolfe term (orange) dominates on large scales, the Doppler term (blue) modulates intermediate scales, and the ISW term (green) adds power at low ℓ. The polarization contribution (red) is subdominant. The full spectrum (black) reflects the coherent sum of all these effects. TODO: maybe change

6. Conclusions

References

Basu, A., Garaldi, E., & Ciardi, B. 2024, Monthly Notices of the Royal Astronomical Society, 532, 841

Cortês, M. & Liddle, A. R. 2024, Monthly Notices of the Royal Astronomical Society, 531, L52

Lewis, A., Challinor, A., & Lasenby, A. 2000, The Astrophysical Journal, 538, 473

Nelson, D., Sharma, P., Pillepich, A., & et. al. 2020, Monthly Notices of the Royal Astronomical Society, 498, 2391

Planck Collaboration, Aghanim, N., Akrami, Y., & et al. 2020, Astronomy & Astrophysics, 641

Reid, R. Accessed: February 2025, Chi-squared distribution table with sigma values, https://www.reid.ai/2012/09/chi-squared-distribution-table-with.html

Reiss, A. G., Scolnic, D., Anand, G. S., & et al. 2024, The Astrophysical Journal, 977, 120

Tumlinson, J., Peeples, M. S., & Werk, J. K. 2017, Annual Review of Astronomy and Astrophysics, 55, 389

Winther, H. A., Eriksen, H. K., Øystein Elgarøy, Mota, D. F., & Ihle, H. Accessed: June 2025, Cosmology II - A course on the formation of the cosmic microwave background and structures in the Universe, https://cmb.wintherscoming.no/index.php

Fig. 5.4. The CMB TE (left) and EE (right) polarization spectra compared with high-ℓ data. The computed spectra reproduce the oscillatory features seen in the data, though the amplitude is somewhat larger and the TE peaks slightly shifted in ℓ, likely due to the neglect of gravitational lensing. TODO: maybe change
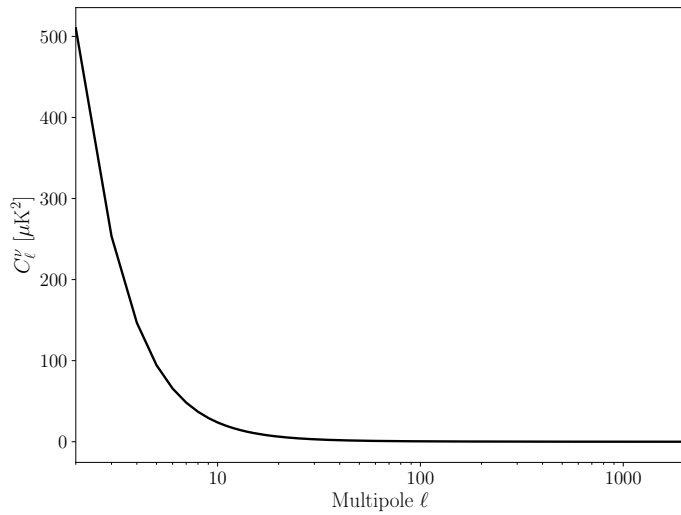
Fig. 5.5. The neutrino angular power spectrum C_ℓ^ν, computed using the same conventions as the CMB temperature spectrum. Although unobservable, the spectrum illustrates the effects of free-streaming relativistic particles and includes only Sachs-Wolfe and ISW contributions. TODO: spectrum looks wrong
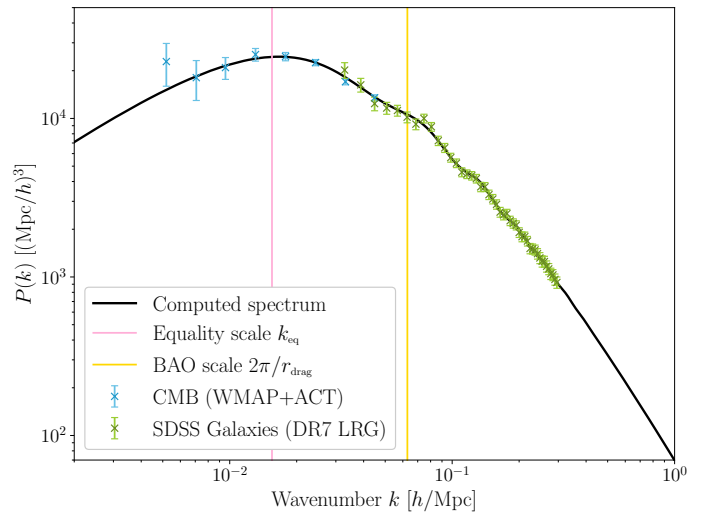
Fig. 5.6. Matter power spectrum $P(k)$ in units of $(\text{Mpc}/h)^3$. Theoretical prediction is compared to WMAP+ACT (blue) and SDSS DR7 LRG (green) data. The model reproduces the overall shape and amplitude well, especially around the BAO feature at $k \sim 0.1\,h/\text{Mpc}$. TODO: maybe change

Appendix A: Toy cosmology figures
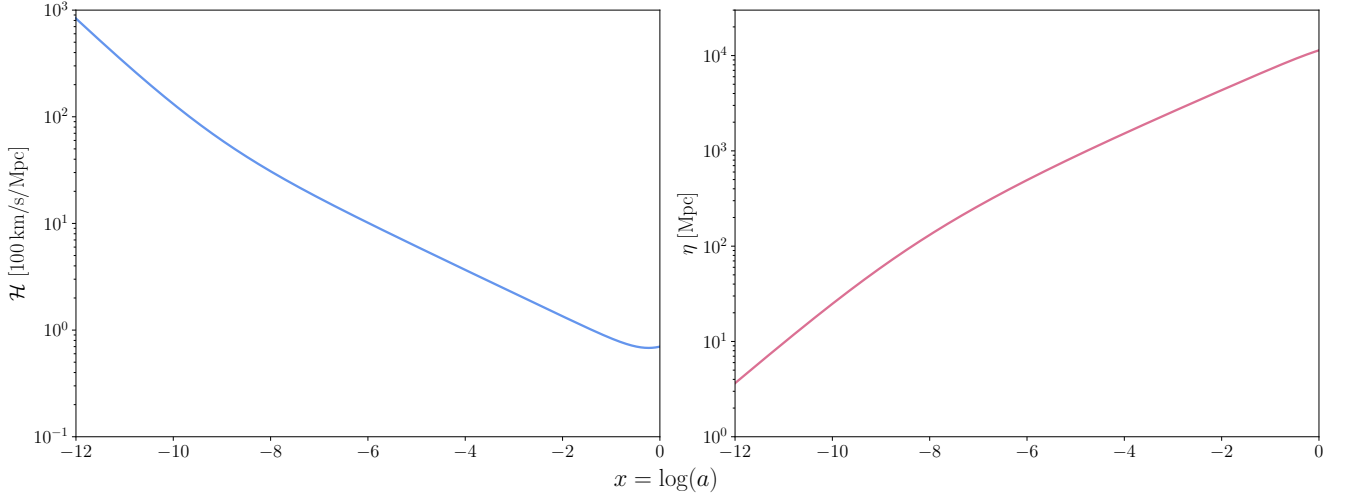
Fig. A.1. Evolution of the conformal Hubble parameter $\mathcal{H}$ (left) and the conformal time η (right) in Winther's toy cosmological model. The parameters used are $h = 0.7$, $\Omega_{CDM0} = 0.45$, $\Omega_{b0} = 0.05$ and $N_{eff} = 0$. Ω_{k0} and T_{CMB0} are the same as for the fiducial cosmology.
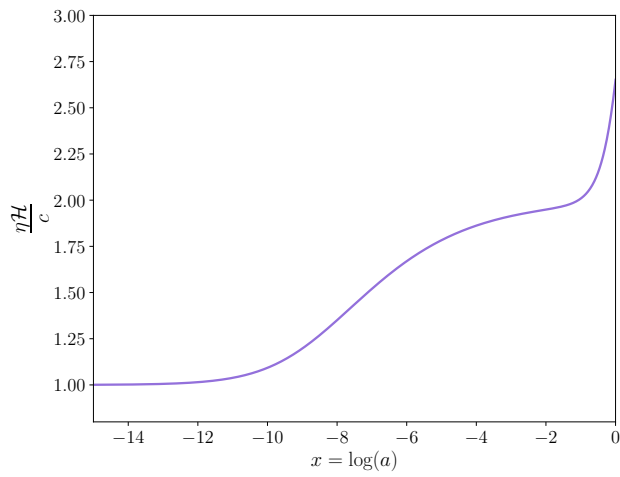
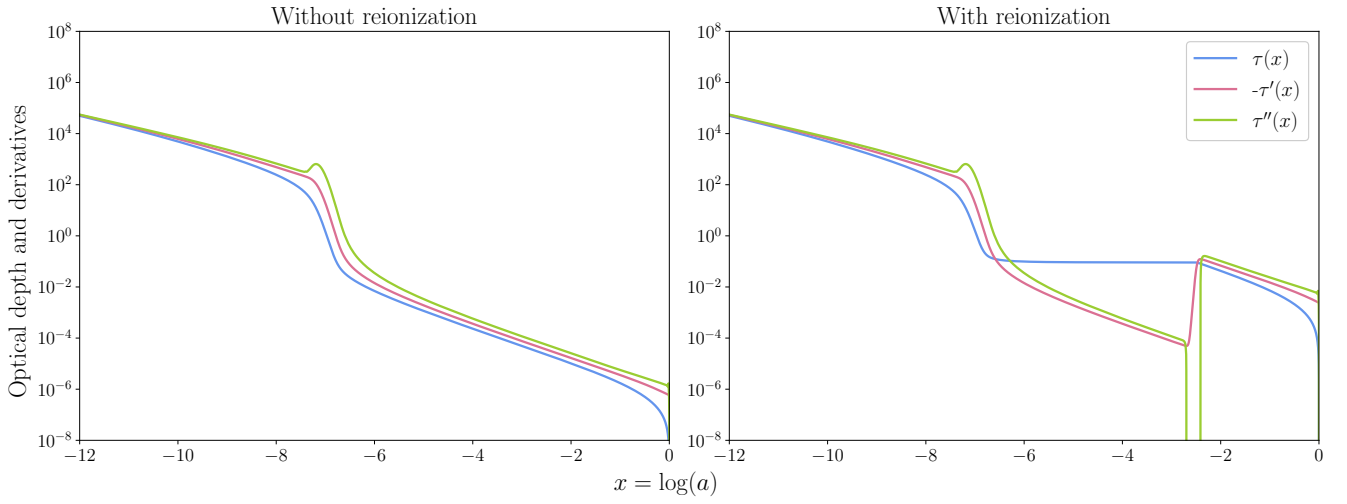**Fig. A.2.** Evolution of the ratio $\eta\mathcal{H}/c$ in Winther's toy cosmological model ($h = 0.7$, $\Omega_{CDM0} = 0.45$, $\Omega_{b0} = 0.05$ and $N_{eff} = 0$).
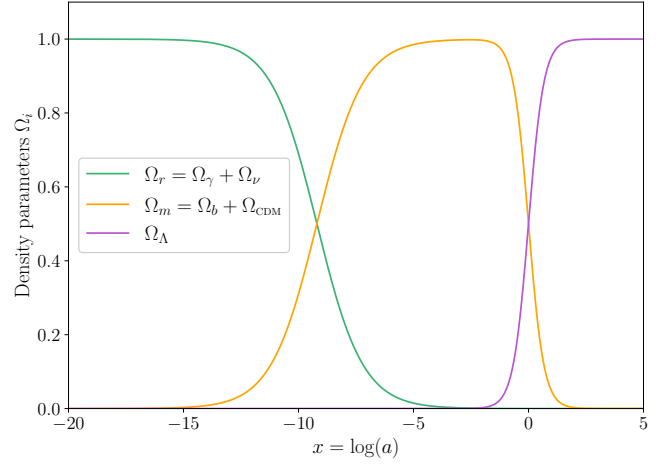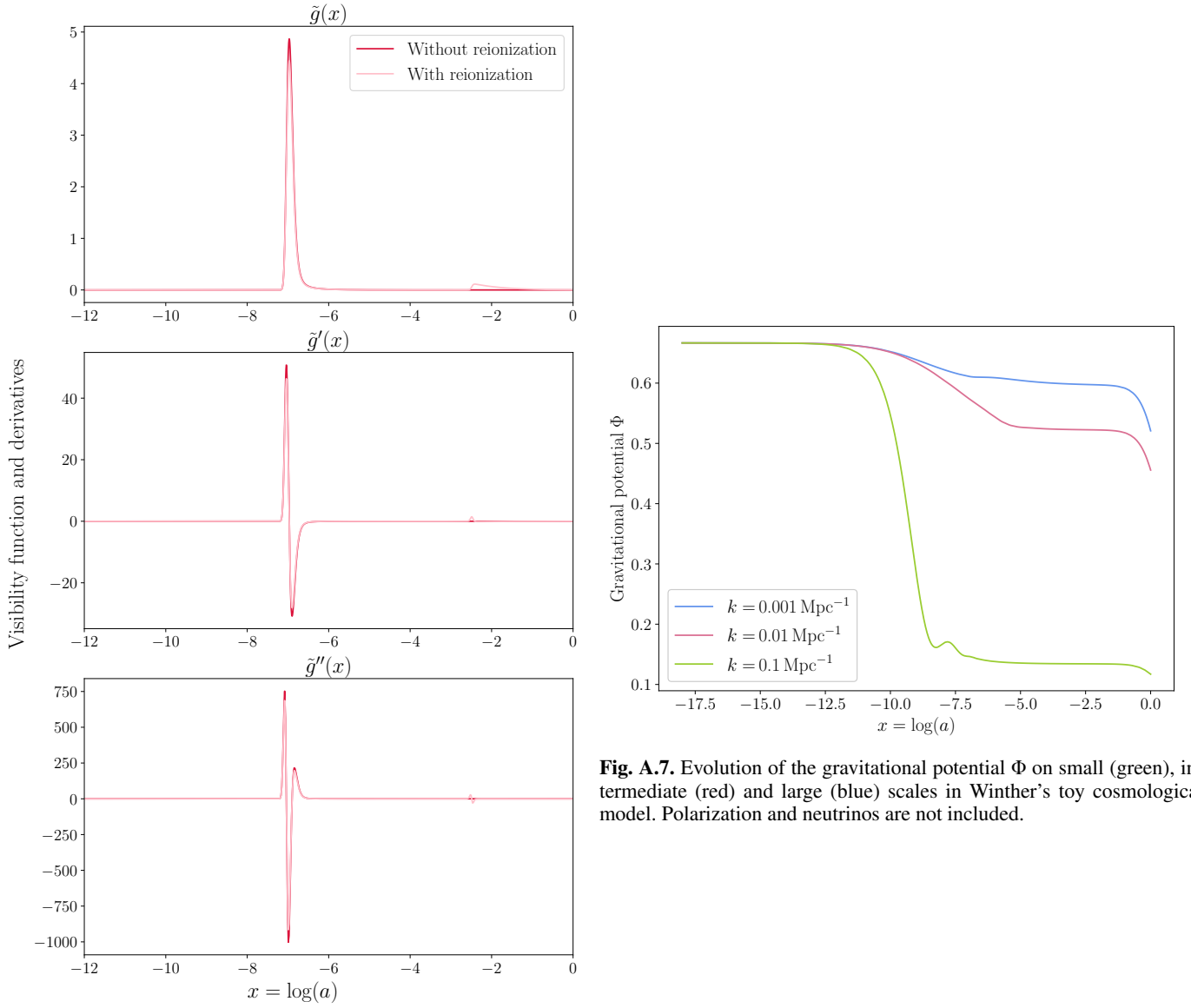
Fig. A.3. Evolution of the density parameters Ω_r (green), Ω_m (orange) and Ω_Λ (purple) in Winther's toy cosmological model ($h = 0.7$, $\Omega_{CDM0} = 0.45$, $\Omega_{b0} = 0.05$ and $N_{eff} = 0$).
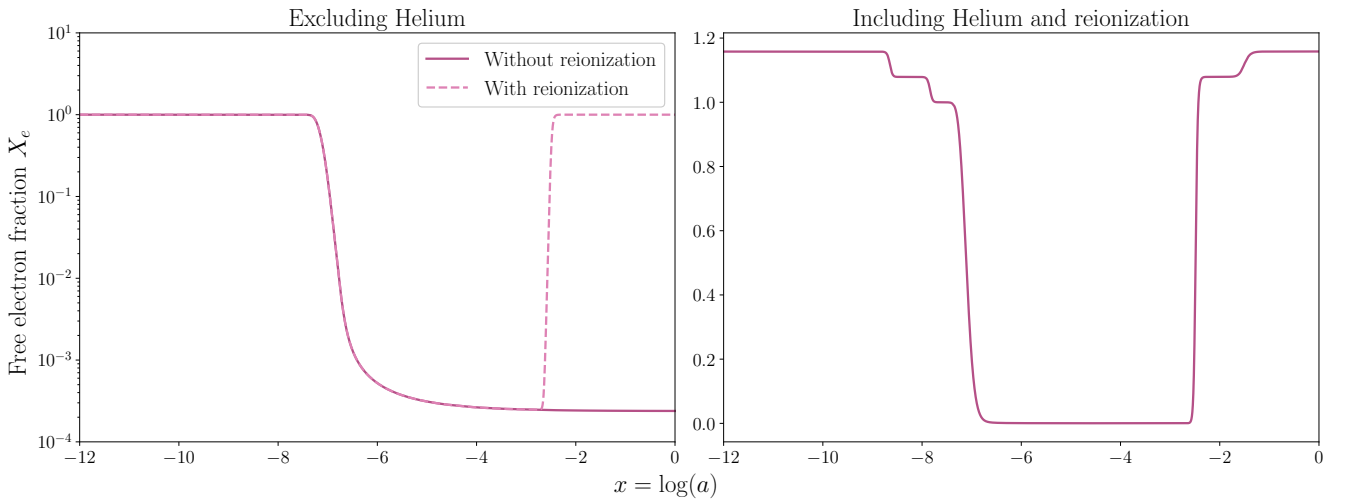
Fig. A.4. Evolution of the free electron fraction with (right) and without (left) Helium in Winther's toy cosmological model. The Hydrogen reionization parameters used are $z_{reion} = 11.0$ and $\Delta z_{reion} = 0.5$. When including Helium, $Y_p = 0.24$ is used as the primordial abundance, and $z_{He,reion} = 3.5$ and $\Delta z_{He,reion} = 0.5$ as Helium reionization parameters.

Fig. A.5. Evolution of the optical depth τ and derivatives $-\tau'$ and τ'' with (right) and without (left) reionization included in Winther's toy cosmological model. Helium is not included, and the reionization parameters used are $z_{\mathrm{reion}} = 11.0$ and $\Delta z_{\mathrm{reion}} = 0.5$.

Fig. A.7. Evolution of the gravitational potential Φ on small (green), intermediate (red) and large (blue) scales in Winther's toy cosmological model. Polarization and neutrinos are not included.

Fig. A.6. The visibility function $\tilde{g}$ (top) and its first (middle) and second (bottom) derivatives $\tilde{g}'$ and $\tilde{g}''$ in Winther's toy cosmological model, plotted with (pink) and without (red) reionization. Helium is not included, and the reionization parameters are $z_{\mathrm{reion}} = 11.0$ and $\Delta z_{\mathrm{reion}} = 0.5$.
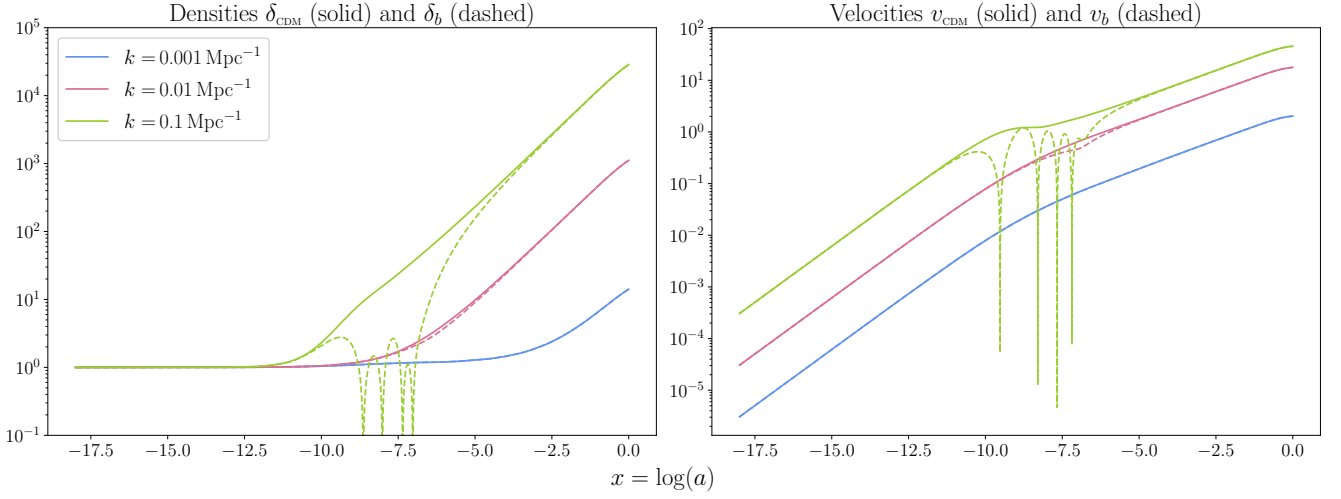
Fig. A.8. Evolution of the CDM and baryon density (left) and velocity (right) perturbations on small (green), intermediate (red) and large (blue) scales in Winther's toy cosmological model. Dashed lines are used for baryons. The absolute values are plotted, since they can be negative and a logarithmic y-axis is used. Polarization and neutrinos are not included.
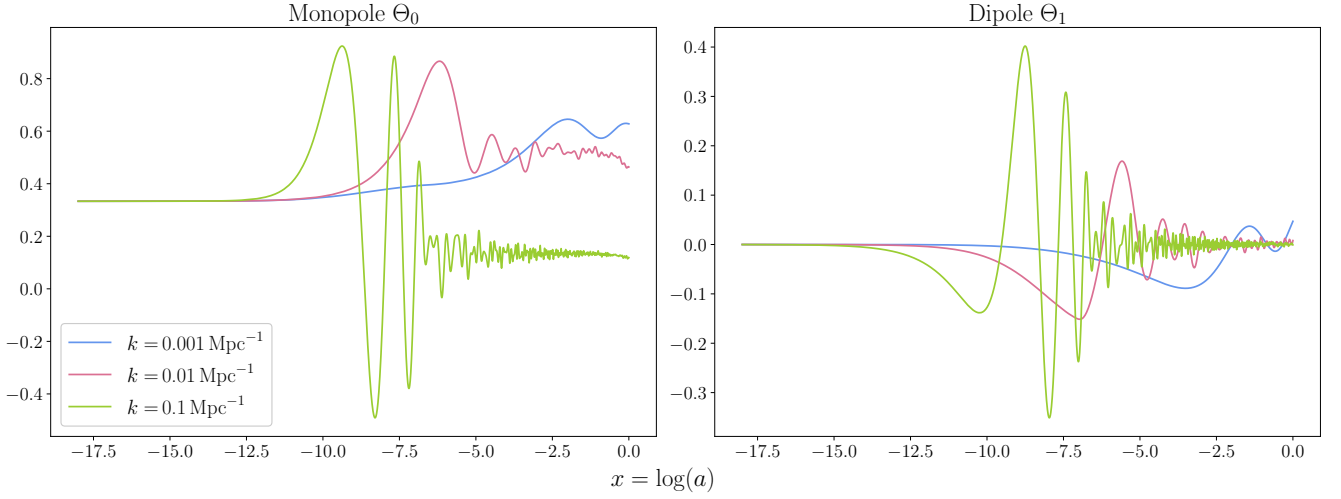
Fig. A.9. Evolution of the photon monopole Θ_0 (left) and dipole Θ_1 (right) on small (green), intermediate (red) and large (blue) scales in Winther's toy cosmological model. Polarization and neutrinos are not included.
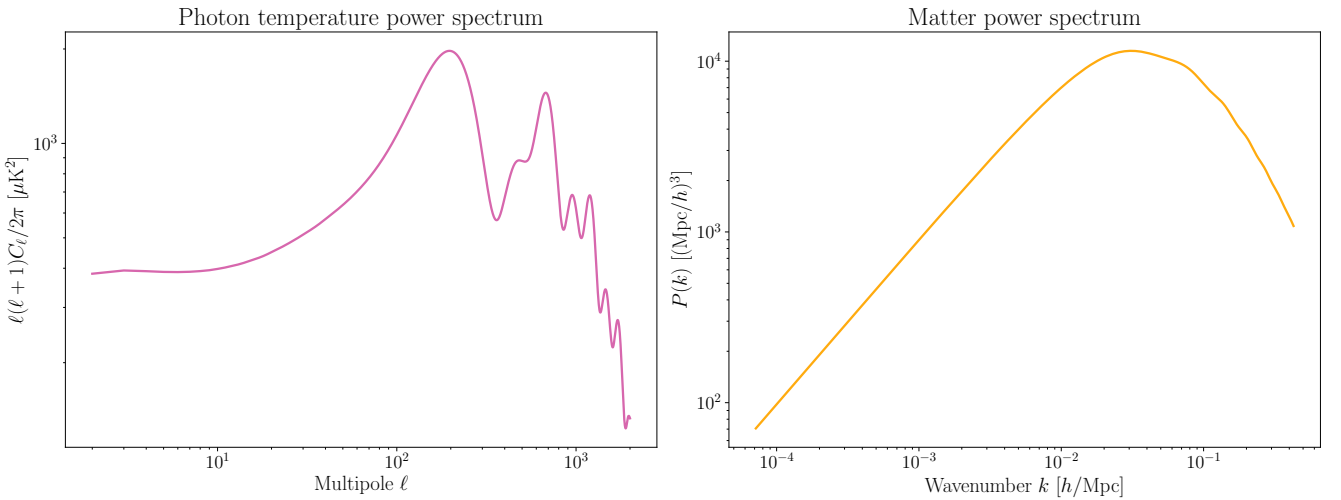
Fig. A.10. The CMB power spectrum $\ell(\ell + 1)C_\ell/2\pi$ (left) and matter power spectrum $P(k)$ (right) in Winther's toy cosmological model. Helium, reionization, polarization and neutrinos are not included. The parameters used for the primordial power spectrum are $A_s = 10^{-9}$, $n_s = 0.965$ and $k_{\mathrm{pivot}} = 0.05\,\mathrm{Mpc}^{-1}$.